
Development and Application of Efficient Methods for the Dynamic Simulation of Charge Transport in Organic Semiconductors

Zur Erlangung des akademischen Grades eines
DOKTORS DER NATURWISSENSCHAFTEN
(Dr. rer. nat.)

von der KIT-Fakultät für Chemie und Biowissenschaften
des Karlsruher Instituts für Technologie (KIT)

genehmigte

DISSERTATION

von

Dipl.-Chem. Alexander Heck

aus

Malsch bei Karlsruhe

KIT-Dekan: Prof. Dr. Willem Klopper

Referent: Prof. Dr. Marcus Elstner

Korreferent: Apl.-Prof. Dr. Wolfgang Wenzel

Tag der mündlichen Prüfung: 12. Februar 2016

Zusammenfassung

Diese Arbeit befasst sich mit der Weiterentwicklung, Anwendung und Evaluierung computergestützter Methoden zur Beschreibung der Dynamik von Ladungsträgern in organischen Halbleitern.

Für eine unvoreingenommene Beschreibung der Ladungsträgerdynamik wird eine vorherige Festlegung des Ladungstransportregimes vermieden. Anstatt von einer delokalisierten Bandstruktur oder von lokalisiertem "Hopping" auszugehen, wird in unserem Modell die Ladung mit der zeitabhängigen Schrödinger-Gleichung propagiert. Diese Multi-Skalen-Methode – ursprünglich entwickelt für die Beschreibung des Ladungstransfers in DNA – musste für die Anwendung auf organische Halbleiter angepasst und erweitert werden. Eine neuer selbstwechselwirkungsfreier Ausdruck für die Gesamtenergie wurde formuliert und neue Bewegungsgleichungen für den Ladungsträger und die Kerne wurden daraus abgeleitet, was sich als notwendig für die korrekte Ladungsträgerdynamik erweist. Darüber hinaus wurde die Methodik um zusätzliche Fragmentorbitale auf jedem Molekül erweitert und lokale als auch nicht-lokale Elektron-Phonon-Kopplungen wurden in einer konsistenten Weise berücksichtigt.

Mit dieser verbesserten Methodik konnten die Ladungsträgermobilität für verschiedene organische Materialien in guter Übereinstimmung mit dem Experiment simuliert werden. Von besondere Relevanz ist die Temperaturabhängigkeit der Mobilität, da sie darauf hinweist in welchem Regime der Ladungstransport stattfindet – "Hopping" oder bandartig. Aus diesem Grund wurde die Temperaturabhängigkeit der Mobilität unterschiedlicher Systeme untersucht, wobei ein Steigen als auch Sinken der Mobilität mit der Temperatur in amorphen bzw. kristallinen Systemen reproduzierbar ist.

Das Herzstück der Methodik ist ein Fragmentorbital Hamiltonian, der darüber hinaus in "Hopping"-Modellen eingesetzt werden kann oder um auf effiziente Weise Informationen über die elektronische Struktur eines molekularen Systems zu erhalten. Ein eleganterer Ansatz zur Berechnung seiner Matrixelemente unter Verwendung der semi-empirischen Methode DFTB wurde entwickelt. Das Benchmarken dieses Vorgehens an einem großen Satz organischer Moleküle bestätigte, dass diese Methode ausgezeichnet zur effizienten Berechnung elektronischer Kopplungen geeignet ist. Darüber hinaus wurde der Einfluss des Selbstwechselwirkungsfehlers von DFT auf die Berechnung der Matrixelemente diskutiert und Korrekturen vorgeschlagen.

Abstract

This work focuses on the development, application, and evaluation of computational methods for the description of the dynamics of excess charge carriers in organic semiconducting materials.

For an unbiased bottom-up description of the charge dynamics, we aim to avoid pre-determination of the charge transport regime. Instead of assuming in our model delocalized bands or localized hopping we perform a direct propagation of the excess charge with the time-dependent Schrödinger equation. This multi-scale method – initially derived for the description of charge transfer in DNA – had to be adapted and further developed for the application to organic semiconductors. A new self-interaction-free total energy expression is formulated and new equations of motion for the excess charge and the nuclei are derived, which turns out to be essential for the correct evolution of the charge carrier. Furthermore, the methodology was enhanced by increasing the active space to an arbitrary number of fragment orbitals per molecule, and local- as well as non-local electron-phonon coupling was included in a consistent way.

With the advanced method, hole mobilities for several organic materials were simulated in good agreement with the experiment. Of particular interest is the temperature dependence of the mobility, because it indicates the regime in which the charge transport takes place – hopping or band-like. Therefore, the temperature dependence of the mobility was investigated in several systems with the finding that our method is able to reproduce both the increase and decrease of the mobility with temperature for amorphous and crystalline systems, respectively.

The core of this method is the fragment orbital Hamiltonian, which can also be applied e.g. in hopping models or to obtain the electronic structure of a molecular system in a linear scaling fashion. A more sophisticated method for the calculation of its matrix elements in the framework of the semi-empirical method DFTB was developed. Benchmarking this approach on a large set of organic molecules confirmed the excellent performance of this method for the efficient calculation of electronic couplings. Furthermore, influence of the self interaction error of DFT on the matrix elements are discussed and corrections proposed.

Acknowledgment

At this point I would like to thank everyone who contributed to the successful completion of this work.

First of all, I would like to express my gratitude to Prof. Marcus Elstner for giving me the opportunity to work on this interesting topic and for his continuous support over the last years. He always took his time for constructive discussions, while giving me the freedom to conduct my research according to my own interest.

I would also like to thank all my colleagues at Karlsruhe Institute of Technology for the enjoyable atmosphere. A special word of thank goes to Tomáš Kubař, who supported me with his words of advice and his vast scientific expertise. Furthermore, I would like to thank Julian Kranz for his qualified feed-back and for assisting me with various calculations on anthracene and P3HT.

Special thanks goes also to Velimir Meded, who was always available for enthusiastic discussions. I am also very grateful for the force field parameters and starting structures of α -NPD and P3HT that were provided by Denis Danilov from the group of Wolfgang Wenzel and by Carl Poelking from the group of Denis Andrienko, respectively.

Furthermore, I want to thank all collaborators, who supported me during my work. Especially the benchmark results are the product of the combined effort of experts with knowledge of different computational methods, and I want to thank explicitly Adam Kubas for organizing our endeavor. Special thank goes also to Asif Bashir and Prof. Christof Wöll for the pleasant cooperation and for providing experimental results of HBC SAMs.

I also like to thank the Karlsruhe House of Young Scientists (KHYS) for providing me with a scholarship (Landesgraduiertenförderung) over the course of two years.

The IT-staff at the Steinbuch Centre for Computing (SCC) and the University Ulm are also thanked for the stable operation of the computer clusters IC2 and Justus and for the provided computer time.

Last but not least, I would like to thank all of my friends and my family for their support and patience during the course of my PhD studies.

Contents

1. Introduction	1
1.1. Advantages and Disadvantages of Organic Semiconductors	1
1.2. Potentials of Organic Semiconductors	3
1.3. Open Challenges	4
1.4. Thesis Outline	7
2. Theoretical Background	9
2.1. Computational Chemistry	9
2.1.1. Density Functional Theory	10
2.1.2. Density Functional Tight Binding	13
2.1.3. Self-Interaction Error of DFT	17
2.1.4. Molecular Mechanics	19
2.2. Electronic States and Couplings	22
2.2.1. Generalized Mulliken-Hush	24
2.2.2. Constrained Density Functional Theory	25
2.2.3. Fragment Orbital Density Functional Theory	26
2.3. Charge Transport Models	29
2.3.1. Miller-Abrahams Rates and Gaussian Disorder Model	30
2.3.2. Marcus Rates	31
2.3.3. Coarse Grained Electron Ion Dynamics	33
2.4. Measurement of Charge Carrier Mobility	36
2.4.1. Time of Flight	37
2.4.2. Pulse-Radiolysis Time-Resolved Microwave Conductivity	37
2.4.3. Thin Film Transistors	39
3. Fragment Orbital Hamiltonian	41
3.1. Conventional DFTB FO Hamiltonian	42
3.2. Improved Block DFTB Hamiltonian	43
3.2.1. Inclusion of External Electric Fields	44

3.3. Benchmarking	44
3.3.1. Database	45
3.3.2. Computational Details	47
3.3.3. Hole Transfer Couplings	50
3.3.4. Electron Transfer Couplings	54
3.3.5. Compensation for Missing Non-Local Exchange	57
3.3.6. Transferability of the Correction	57
3.3.7. Influence of Electron Number in FO Calculations	61
3.4. Discussion and Conclusion	63
4. Bridge-mediated Couplings	69
4.1. Studied Systems	70
4.2. Computational Details	71
4.2.1. Geometry Optimization	71
4.2.2. DFTB Calculations	72
4.2.3. CDFT Calculations	72
4.3. Results	72
4.4. Discussion and Conclusion	76
5. Advancements in Coupled Electron Ion Dynamics	79
5.1. Influence of Self-Interaction on the Charge Evolution	80
5.2. Self-Interaction-Free Total Energy Expression of the Charged System	84
5.2.1. Fragmentation of the System	85
5.2.2. Approximations in the Quantum Calculations	87
5.3. Propagation of Electronic Degrees of Freedom	88
5.4. Propagation of Nuclear Degrees of Freedom	90
5.5. Outlook: Electronic Polarization	93
5.6. Discussion	94
6. Evaluation of Coupled Electron Ion Dynamics on Anthracene and HBC	97
6.1. Simulation Setup	98
6.2. Evaluation of Site Energies	99
6.3. Evaluation of Electronic Couplings	100
6.4. Influence of the Environment	101
6.5. Electron-Phonon Coupling	101
6.6. Picture of the Charge Transport	102
6.7. Charge Carrier Mobilities	104

6.8. Charge Transport Mechanism	107
6.9. Relevance of Lower-lying Orbitals	109
6.10. Discussion	112
7. Temperature Dependence of Mobilities	115
7.1. General Simulation Setup	116
7.2. Study of an Ordered Material: Anthracene	117
7.2.1. Results and Discussion	117
7.3. Study of a Disordered Material: α -NPD	118
7.3.1. Simulation Setup	119
7.3.2. Results and Discussion	120
7.4. Study of a Semi-Ordered Material: P3HT	121
7.4.1. Simulation Setup	122
7.4.2. Results and Discussion	123
7.5. Enforcing Order: HBC	124
7.5.1. Simulation Setup	125
7.5.2. Results and Discussion	126
7.6. Conclusion	128
8. Summary and Future Work	131
A. Appendix	133
A.1. Electronic Couplings with Degenerated States	133
A.2. Test of Basis Sets and FODFTB Methods	134
Bibliography	137

List of Figures

1.1. Global electricity production	4
2.1. Total energy for a (fractional) number of electrons.	18
2.2. Energy profile along the reaction coordinate between initial and final diabatic state	24
2.3. Free energy profile for a donor acceptor system according to Marcus theory	32
2.4. Setup for a time of flight measurement.	37
2.5. Setup for a PR-TRMC measurement.	38
2.6. Setup for a TFT measurement.	39
3.1. Schematic representation of the alignment of a dimer.	47
3.2. Correlation between calculated CDFT/0, CDFT/50, FODFT, FODFTB H_{ab} values and reference data.	58
3.3. Thiophenes in additional orientations.	59
3.4. Variation of electronic coupling along rotations.	60
3.5. CPU time for H_{ab} calculations and corresponding relative errors in the ET rate due to the error in H ab.	67
4.1. Hetero-cyclopentadiene systems for studying various factors that affect T_{DA} : (1) influence of the energetic separation between B and D/A. (2) influence of D-A distance. (3) influence of the number of bridging molecule	71
4.2. T_{DA} for increasing D-A distance	75
4.3. Dependence of T_{DA} on the length of the bridge	75
4.4. T_{DA} for different bridging molecules	77
5.1. Time evolution of the occupation in a two-site system with and without artificial stabilization.	82
5.2. Highest occupied molecular orbitals during a molecular dynamic simulation.	86
6.1. Morphology of anthracene and HBC-LC	98

6.2.	Comparison of HOMO energies obtained with and without self-consistency to the ionization potential.	100
6.3.	Power spectrum of site energies with and without the electrostatic potential of the environment.	101
6.4.	Relaxation of site energies upon charging.	102
6.5.	QM zone of anthracene	103
6.6.	QM zone of HBC	103
6.7.	Time evolution of the hole in anthracene and HBC	105
6.8.	Density of states and the number of molecules over which these states are delocalized. Shown values are averages over each simulation of the anthracene b-direction.	108
6.9.	Percentage of adiabatic states that are occupied, averaged over 100 simulations.	109
6.10.	Dependence of the electronic couplings on the relative rotation of two HBC molecules around the columnar axis.	110
6.11.	Energies of molecular orbitals for an HBC stack of different size.	111
7.1.	Molecular building blocks of the systems studied in this chapter. a) anthracene b) α -NPD c) P3HT d) HBC-LC e) HBC-SAM.	117
7.2.	Temperature dependent mobilities in anthracene	118
7.3.	QM zone of α -NPD	120
7.4.	Temperature dependent mobility in α -NPD	121
7.5.	QM zone of P3HT	122
7.6.	Temperature dependent mobility in P3HT	124
7.7.	QM zone of HBC-SAM	126
7.8.	Temperature dependent mobility in HBC	127
7.9.	Summary of the temperature dependent mobilities of all system studied in this chapter.	129
A.1.	Comparison of FODFTB methods and confinement radii	135

List of Tables

3.1. Database of organic molecules for the calculation of electronic coupling matrix elements for hole and electron transfer.	46
3.2. Absolute values of the electronic coupling H_{ab} between cationic dimers at various distances and its exponential decay constant β	51
3.3. Absolute values of the electronic coupling H_{ab} between anionic dimers at various distances and its exponential decay constant β	55
3.4. Errors of H_{ab} after applying a method-specific scaling factor	59
3.5. Statistical evaluation of the error of H_{ab} calculated for 15 randomly rotated cationic thiophene dimers.	61
3.6. Electronic coupling matrix elements calculated for six randomly oriented anionic anthracene dimers.	62
3.7. Comparison of electronic coupling matrix elements calculated with and without explicit charge in the system.	64
4.1. Total electronic coupling T_{DA} (in eV) for systems shown in figure 4.1 . . .	73
4.2. Tunneling barriers for the systems shown in figure 4.1 calculated as difference between vertical IPs of B and D/A	76
6.1. Electronic coupling between nearest neighbors for the anthracene crystal structure obtained with FODFTB and with FODFT at the B3LYP/TZ2P level	100
6.2. Hole mobilities for anthracene along crystallographic axes as well as for liquid crystalline HBC along the columnar stacking direction.	106
7.1. Comparison of the simulated hole mobilities of anthracene with experimental values obtained from TOF measurements	119

Acronyms

AO atomic orbital

CASSCF complete active space self-consistent field

CDFT constrained density functional theory

CEID coupled electron ion dynamics

CT charge transfer

DC direct current

DFT density functional theory

DFTB density functional tight-binding

FET field-effect transistor

FO fragment orbital

FODFT fragment orbital density functional theory

GGA generalized gradient approximation

GMH generalized Mulliken-Hush

HBC-LC hexa(3,7-dimethyloctanyl)hexa-peri-hexabenzocoronene

HBC-SAM 2,5-bis[4-(S-acetylthiomethyl)phenylethynyl]-8,11,14,17-tetrakis(3,7-dimethyloctanyl)hexa-peri-hexabenzocoronene

HF Hartree-Fock

ISC inorganic semiconductor

LDA local density approximation

MD molecular dynamics

MM molecular mechanics

MRCI+Q multi-reference configuration interaction singles and doubles with Davidson correction

NEVPT2 N-electron valence state perturbation theory

OFET organic field-effect transistor

OLED organic light-emitting diode

OSC organic semiconductor

P3HT poly(3-hexylthiophen)

PCBM phenyl-C61-butyric acid methyl ester

PME particle mesh Ewald

PR-TRMC pulse-radiolysis time-resolved microwave conductivity

QM quantum mechanics

SAM self-assembling monolayer

SCS-CC2 spin-component scaled second-order approximate coupled cluster method

SI self-interaction

STM scanning tunneling microscope

TFT thin film transistor

TOF time of flight

vdW van der Waals

Introduction

High electrical conductivity of organic compounds was already observed in 1972 in a bimolecular charge-transfer salt of tetrathiafulvalene (TTF) as electron donor, and tetracyanoquinodimethane (TCNQ) as electron acceptor.¹ In 1976 electrical conductivity was also found in polymers after oxidation of polyacetylene with halogens by Heeger, MacDiarmid, and Shirakawa,^{2,3} who were rewarded with the Nobel prize in chemistry for this work in the year 2000. Today, there exists a large variety of organic semiconducting materials, consisting of small molecules or polymers. What they all have in common is that their molecular building blocks are only weakly interacting via van der Waals (vdW) forces, in contrast to the covalent network that is formed by conventional inorganic semiconductors (ISCs). This fundamental difference at the atomic scale gives rise to largely different mechanical and electronic properties and therefore allows distinct fields of application. The most important advantages and disadvantages of OSCs over ISCs are summarized in the following.

1.1. Advantages and Disadvantages of Organic Semiconductors

- **Low-cost Production:** A significant share of the total production cost of electronic components is attributed to the complex fabrication process and not to the material price.⁴ One of the most interesting properties of OSCs is the possibility to reduce these costs significantly. Due to their weak intermolecular interaction, soluble OSC molecules can be synthesized, which gives access to one of the most inexpensive industrial patterning process: printing. Using the technologies that are applied to conventional printed products (newspapers, posters, packaging etc.),

large circuits consisting of thin-film transistors and other components can be easily patterned onto a broad range of substrates like plastic, glass, or metal foils. These printing technologies can be divided into sheet-based and roll-to-roll-based approaches. Sheet-based inkjet printing is the best solution for low-volume production with frequently changing requirements. Applying offset, gravure or flexographic printing in roll-to-roll processing allows high-volume production of roughly $10.000 \text{ m}^2/\text{h}$.⁵ Roll-to-roll processing of organic electronics is still in a development phase. If the industrial application of this technology succeeds, however, many OSC devices could be produced at a fraction of conventional ISCs.

- **Flexibility:** Weak intermolecular interaction and self-assembling properties of the semiconducting molecules give rise to bendable electronic devices, when a flexible substrate like a polymer film is used. Circuits may remain functional even when they are bent with a radius of just $100 \text{ }\mu\text{m}$.⁶
- **Large-area Processing:** Inorganic semiconductor devices are quite limited in size, due to their difficult production process that cannot be up-scaled easily in most cases. For example, crystalline inorganic solar-cells are assembled from small wafers that have to be cut from a single crystal. Printing of organic semiconductors, on the other hand, is a possibility to produce large scale devices in a single step. Even more pronounced is the difference in the field of lighting. There is a growing interest in producing large-area organic light-emitting diodes (OLEDs) as novel lighting solutions.
- **Easy Modifications:** The molecular structure of organic semiconductors, provides easy routes to modify the solubility or electronic properties of a compound. Solubility, for example can be controlled by modifications in the side chains⁷ and the carrier mobility and band gap of polymers can be modified by their molecular weight.^{8,9}
- **Bad Performance:** The weak intermolecular interaction in OSCs makes these materials vulnerable to environmental influences like oxygen and moisture. Although carrier mobilities in organic materials have already improved since the early studies, they still lack behind the mobilities that can be observed in crystalline inorganic materials. The low carrier mobility of OSCs manifests in low efficiencies of organic solar cells and slow switching speeds of organic field effect transistors.¹⁰

1.2. Potentials of Organic Semiconductors

The advantages of OSCs, presented above, give rise to an astonishing potential. OSCs are applied in a wide range of electronic components like OLEDs,^{11–13} organic field-effect transistors (OFETs)^{10,14,15} and organic solar cells.^{16–18} Commercial application of OSCs takes place mainly in form of OLEDs as pixel in thin and/or flexible displays. These are nice gadgets but OSCs have a potential impact on a much larger scale, that we will outline briefly in the following. The realization of these visions is, however, dependent on the ability to produce devices with sufficient performance at a significantly lower cost than conventional devices, based on ISCs.

Sustainable Energy Supply

One major challenge of the current century is the continuously growing demand for energy, which is increasing at an alarming rate (see figure 1.1a). In a world with finite resources it is obvious that such a non-sustainable growth, mainly fueled by fossil resources, has to come to an end. Regenerative energy sources are the only viable solution in the long run. A virtually infinite source of energy that powers nearly all life on earth is the sun. From the $\sim 10^9$ TWh of solar energy that reach the ground per year only $\sim 0.5 \cdot 10^6 - 15 \cdot 10^6$ TWh are estimated to be technical usable,¹⁹ which is, however, still considerably larger than the global energy consumption of $\sim 2.5 \cdot 10^4$ TWh.²⁰ The importance of solar energy is growing with an astonishing rate (see figure 1.1 b) and with so much open potential there is no physical limit in the near future. Already today, more electricity is worldwide produced from solar energy than from geothermal sources. Between 2005 and 2010 the amount of solar electricity increased by a factor of 10. If this trend continues, solar electricity might be the dominant share of the global renewable electricity production in 10 years from now.

However, photovoltaic is currently still among the most expensive sources of electricity. Furthermore, the high amount of energy that is required in the production of inorganic photovoltaic cells takes more than a year of device operation until it is paid back.²¹ The energy-saving production of organic photovoltaic has the potential of fast energy pay-back times and the large-scale roll-to-roll printing may reduce the production cost of photovoltaic cells dramatically.⁴ However, organic solar cells lack behind their inorganic counterparts regarding efficiency, and for the design of better materials a more comprehensive understanding of the processes in organic OSCs is required.²²

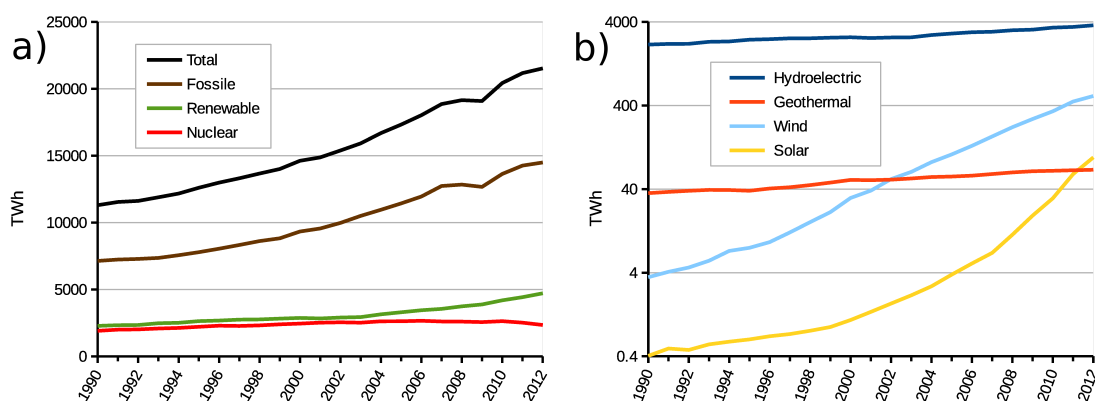


Figure 1.1.: a) Global electricity production over the last 20 years broken down to different sources. b) Contribution of different technologies to the global renewable electricity production. Source: U.S. Energy Information Administration (Oct 2015)

Ubiquitous Computing and Internet of Things

The idea behind ubiquitous computing is providing access to the digital world at any time and everywhere. The desktop computer as main gate to the digital world will be replaced by "smart objects", which can come in any shape and support the user seamlessly in his everyday live. First steps in this direction are devices like laptop, smart phone and augmented reality glasses. In a further step, also objects of everyday live will obtain processing power and network connectivity. This could be realized with RFID-tags, which are small, printable and enable wireless identification of objects. The collection and exchange of data from these smart objects is also referred to as "internet of things" and is seen as the next informational revolution.²³ Again, low cost production of electronic components with sufficient device performance is essential for this technology to take off.

1.3. Open Challenges

Efficient charge transport in OSCs is essential for their success. One design goal is therefore the improvement of charge carrier mobilities by structural modification of existing compounds as well as syntheses of completely new organic materials. However, the overwhelming amount of possible compounds makes fast progress on a trial and error basis unlikely. A detailed understanding of the charge dynamic in OSCs would greatly help to

guide further efforts in improving device performance, but a comprehensive description of charge transport in high-mobility OSCs is still missing.

The difficulty in the description of these materials arises from their complex molecular morphology that is not as perfectly ordered as inorganic crystalline systems but also not completely disordered like amorphous systems. One important property that influence charge transfer (CT) is the packing motive of the molecules, since their relative orientation has a pronounced impact on the electronic coupling elements.²⁴ At finite temperatures, also the distortion of the equilibrium geometry due to local and non-local electron-phonon couplings gets important.²⁵ Former introduce fluctuations of the site energies, whereas latter mainly influence the electronic coupling between molecules, which in turn has a significant influence on the charge carrier dynamics.^{26–28} Another factor that can have a significant impact on the efficiency of OSCs is the presence of impurities or structural defects in the material. They can trap charge carriers, which will reduce the mobility tremendously and gives rise to activated transport.^{15,29} In summary, this shows the pronounced importance of the atomistic structure and its dynamics for the charge transport in organic semiconductors.

There are two main challenges for which atomistic simulations are valuable tools:

- 1) Description of the variety of morphologies that are accessible under experimental conditions.
- 2) Unraveling the mechanism of the charge transport.

In this work we will focus on the second problem and will consequently study already well characterized structures. In the recent decade, different methodologies were successfully applied for the description of charge transport in OSCs. On the one hand, there are several variants of hopping models.³⁰ In these models the charge is restricted to a single molecule and thermal activation can enable transitions to neighboring sites. Due to the localized description of the charge carrier, density functional theory (DFT) calculations of large molecular systems with inclusion of environmental effects are affordable. These methods are usually applied to disordered systems like amorphous AlQ₃³¹ or α -NPD³² but also to more ordered systems like liquid crystals,^{33–35} polymers^{36,37} or partially disordered organic crystals.^{38–40} On the other hand, model Hamiltonian approaches, parametrized from ab initio or DFT calculations, have been further developed and successfully applied to ordered crystal structure, see e.g. ref. 25 and 41 for a recent review.

The limits of these models have been intensely discussed, i.e. lack of solutions for the full-bandwidth case in combination with non-local electron-phonon couplings.⁴¹ The importance of the non-local electron-phonon couplings has been emphasized several times, therefore the restriction of theory to go beyond the small polaron model seems to be severe.⁴² Due to the 'non-existence' of small polarons in high-mobility OSCs, the charge carrier is no longer localized, and a hopping description becomes inadequate.^{29,43,44} Therefore, new methods have been proposed based on numerical propagation of the charge carrier.

Applying a time-dependent Hamiltonian, the charge carrier can be propagated using stochastic, mean-field (MF: Ehrenfest) or surface hopping (SH) approaches.^{42,45,46} MF and SH are semi-classical approaches, where the electronic wavefunction is propagated with the time-dependent Schrödinger equation and the nuclear degrees of freedom follow classical trajectories. In principle, the nature of the charge carrier and the transfer mechanism is not predetermined in these approaches. Therefore, they allow a localized as well as delocalized character of the charge carrier. However, since they are approximation to the full quantum propagation, they exhibit various drawbacks, as discussed for the application to OSCs in detail recently.^{45,46} Valuable insights can already be obtained with model Hamiltonians, where the atomic resolution is discarded and the nuclear vibration is reduced to few relevant modes.^{26,28,47} While model Hamiltonians can give insight into basic principles, detailed information about structure, dynamics and their impact on the charge transport parameters has to be included for a quantitative simulation of real materials. For instance, the electronic structure and electron-phonon interaction has to be resolved at an atomistic level. Such MF simulations have already been performed at various levels of quantum treatment, e.g. using a Su–Schrieffer–Heeger model Hamiltonian to describe fast transport through ordered systems like pentacene,⁴⁸ using a DFT based scheme for liquid crystals⁴⁹ or the intrachain transport in polymers applying an approximate DFT method DFTB.⁵⁰ Full atomic orbital DFT or DFTB approaches, however, exhibit a high computational demand, therefore these simulations have to be restricted to small systems that are arguably representative of the bulk material. Application of linear scaling fragment orbital (FO) methods, however, allows to tackle significantly larger systems.

1.4. Thesis Outline

After introducing the most important theoretical background in chapter 2, we will first develop a new procedure for the calculation of fragment orbital Hamiltonians in the framework of DFTB in chapter 3. The electronic couplings derived from this Hamiltonian will be benchmarked in the remainder of this chapter. Its application to bridge-mediated charge transfer will be subsequently evaluated in chapter 4. Next, we will advance a method for the coupled propagation of electrons and nuclei in chapter 5, where this Hamiltonian will play a central role. In chapter 6 we will evaluate the new method and look at details of the charge transport mechanism before we study the temperature dependence of the mobility of various OSCs in chapter 7.

Theoretical Background

In this chapter, a foundation for the study of charge transport in OSCs will be given. The fundamentals of the computational methods that are used throughout this work are shown in section 2.1, and in section 2.2 we will see how these methods are applied in the calculation of CT parameters. In section 2.3 we will then discuss several theoretical models for the simulation of charge transport, and in section 2.4 we will briefly summarize how experimental methods get insight into the charge carrier dynamics.

2.1. Computational Chemistry

The central aim of computational chemistry is the calculation of the total energy of a system. In the Born-Oppenheimer approximation⁵¹ the motion of nuclei and electrons are separated and the (non-relativistic) electronic energy can be calculated by the time-independent Schrödinger equation

$$\hat{H}\Psi_i(r_1 \dots r_N) = E\Psi_i(r_1 \dots r_N) \quad (2.1)$$

where $\Psi_i(r_1 \dots r_N)$ is the N -electron wave function (Slater-Determinant) of the ground ($i = 0$) and i -th excited adiabatic state. The Hamiltonian \hat{H} can be further divided

$$\hat{H} = \hat{T}_e + \hat{V}_{en} + \hat{V}_{ee} \quad (2.2)$$

$$\hat{T}_e = \sum_{i=1}^N -\frac{\nabla^2}{2}, \quad \hat{V}_{en} = \sum_{i=1}^N \sum_{\alpha=1}^n \frac{-Z_\alpha}{|R_\alpha - r_i|}, \quad \hat{V}_{ee} = \sum_{i=1}^N \sum_{j=1}^N \frac{1}{|r_i - r_j|}$$

here \hat{T}_e is the operator of the kinetic energy of the electrons, \hat{V}_{en} describes the electron-nuclei attraction and \hat{V}_{ee} the electron-electron repulsion. Due to the last term the elec-

trons are correlated, which is difficult to describe. One efficient approach to tackle this problem is the density functional theory.

2.1.1. Density Functional Theory

The foundation of the DFT is the Hohenberg-Kohn theorem, which shows that there is a one-to-one relation between the external potential, the electron density $\rho(r)$ and the electronic wavefunction Ψ , which means that the electronic wavefunction can be expressed as functional of the electronic density⁵²

$$\Psi(r) = \Psi[\rho(r)] \quad (2.3)$$

Consequently, the expectation value of every observable is also a functional of the density

$$\langle \Psi | \hat{A} | \Psi \rangle = A[\rho(r)] \quad (2.4)$$

Therefore, the knowledge of the density should be sufficient in order to calculate e.g. the total electronic energy

$$E[\rho] = T[\rho] + E_{en}[\rho] + E_{ee}[\rho] \quad (2.5)$$

where $T[\rho]$ is the kinetic energy functional of the electrons, $E_{en}[\rho]$ describes the electron-nuclei attraction and $E_{ee}[\rho]$ is the electron-electron repulsion.

This is an enormous facilitation compared to eq. 2.1, since now we need only the 3 spatial coordinates of the density in contrast to the $3N$ spatial coordinates of the N -electron wavefunction.

However, the exact functional that yields the electronic energy from the electron density is still unknown. Only for the electron-nuclei attraction the functional form is known to be

$$E_{en}[\rho] = - \sum_{\alpha} \int \frac{Z_{\alpha} \rho(r)}{|R_{\alpha} - r|} dr \quad (2.6)$$

where Z_{α} is the nuclear charge of atom α at position R_{α} .

For the remaining terms in eq. 2.5 Kohn and Sham introduced a fictitious system of non-interacting electrons.⁵³ If we separate the non-interacting system from the electronic energy expression, eq. 2.5 becomes

$$E[\rho] = T_S[\{\phi_i[\rho]\}] + E_{en}[\rho] + J[\rho] + E_{xc}[\rho] \quad (2.7)$$

where the subscript in $T_S[\{\phi_i[\rho]\}]$ indicates that this is the kinetic energy of non-interacting electrons (Slater-determinant), for which

$$T_S[\{\phi_i[\rho]\}] = \sum_i^{occ} \langle \phi_i | -\frac{1}{2}\nabla^2 | \phi_i \rangle \quad (2.8)$$

$J[\rho]$ is the classical coulomb energy of a charge density, given as

$$J[\rho] = \frac{1}{2} \int \frac{\rho(r)\rho(r')}{|r-r'|} dr dr' \quad (2.9)$$

and the difference between the non-interacting and interacting system is captured by the last term of eq. 2.7, which defines the exchange-correlation functional as

$$E_{xc}[\rho] = (T[\rho] - T_S[\rho]) + (E_{ee}[\rho] - J[\rho]) \quad (2.10)$$

This way the major part of the electronic energy can be calculated with the known expressions for the non-interacting electrons and approximations have only be made in the functional form of $E_{xc}[\rho]$.

For the homogeneous electron gas, an expression for the exchange is exactly known, whereas the exact correlation is only known in the high- and low-density limit. For intermediate densities quantum Monte-Carlo simulations of the energy can yield the correlation energy.⁵⁴ There exist a variety of approximations to the exact exchange-correlation functional. In the local density approximation (LDA) the exchange correlation energy depends only on the value of the electronic density at each point in space. Derivatives of the density are additionally included in the generalized gradient approximation (GGA) in the functional $E_{xc}[\rho]$. Since exchange is exactly described within Hartree-Fock (HF) theory, a successful strategy for the design of accurate exchange-correlation functionals is to include a certain percentage of exact HF-exchange in the so called hybrid-functionals.

Kohn and Sham showed that the density that minimizes the interacting many-body system (as described by a many-body Hamiltonian like in eq. 2.2) is the same as the density that minimizes a non-interacting (single-body) system in an effective potential $v_{eff}(r)$.⁵³ This gives rise to the famous Kohn-Sham equations

$$\left[-\frac{1}{2}\nabla^2 + v_{eff}(r) \right] \phi_i(r) = \epsilon_i \phi_i(r) \quad (2.11)$$

where ϵ_i are the single-particle energies and the effective potential is

$$v_{eff}(r) = v_{en}(r) + v_H(r) + v_{xc}(r) \quad (2.12)$$

with the three contributions

$$v_{en}(r) = \frac{\delta E_{en}[\rho]}{\delta \rho(r)} = - \sum_{\alpha} \frac{Z_{\alpha}}{|R_{\alpha} - r|} \quad (2.13)$$

$$v_H(r) = \frac{\delta J[\rho]}{\delta \rho(r)} = \int \frac{\rho(r')}{|r - r'|} dr' \quad (2.14)$$

$$v_{xc}(r) = \frac{\delta E_{xc}[\rho]}{\delta \rho(r)} \quad (2.15)$$

By expanding the Kohn-Sham orbitals in atomic basis functions $\eta_{\mu}(r)$

$$\phi_i(r) = \sum_{\mu} c_{\mu}^i \eta_{\mu}(r) \quad (2.16)$$

we can write the Kohn-Sham equation from eq. 2.11 as

$$\sum_{\mu} c_{\mu}^i \hat{H}[\rho] |\eta_{\mu}\rangle = \epsilon_i \sum_{\mu} c_{\mu}^i |\eta_{\mu}\rangle \quad (2.17)$$

with $\hat{H}[\rho] = \hat{T} + v_{eff}(r)$. After multiplication from left with $\langle \eta_{\nu} |$ we obtain

$$\sum_{\mu} c_{\mu}^i \langle \eta_{\nu} | \hat{H}[\rho] |\eta_{\mu}\rangle = \epsilon_i \sum_{\mu} c_{\mu}^i \langle \eta_{\nu} | \eta_{\mu}\rangle \quad (2.18)$$

which can be expressed in matrix notation as

$$\mathbf{HC} = \mathbf{SC}\epsilon \quad (2.19)$$

Solution of this matrix equation yields the orbital energies ϵ_i and the orbital coefficients c_{μ}^i . The density is then obtained from the occupied Kohn-Sham orbitals

$$\rho(r) = \sum_i^{occ} \langle \phi_i | \phi_i \rangle \quad (2.20)$$

Since both $v_H(r)$ and $v_{xc}(r)$ depend on the solution $\phi_i(r)$ of the Kohn-Sham equations via $\rho(r)$, they have to be solved iteratively. Once the solution is converged, one can calculate

the electronic energy from eq. 2.7 or, equivalently and more conveniently, from

$$E[\rho] = \sum_i^{\text{occ}} \epsilon_i - \frac{1}{2} \iint' \frac{\rho(r)\rho(r')}{|r-r'|} dr dr' - \int v_{xc}(r)\rho(r)dr + E_{xc}[\rho] \quad (2.21)$$

2.1.2. Density Functional Tight Binding

Many chemical problems can be solved with DFT with sufficient accuracy. More efficient methods are required, however, for large systems with more than 1000 atoms or if a myriad of calculations are necessary, like in the screening of large molecular data sets or if calculations are performed at every step along a molecular dynamics (MD) trajectory. Density functional tight-binding (DFTB) introduces well-controlled approximations to DFT, which reduce the computational cost by about three orders of magnitude. In the following we will only outline the basics of the DFTB methods DFTB1 and DFTB2, whereas a detailed review can be found in ref. 55 and 56.

The computational cost of DFT calculations increases with N^3 , where N is the number of basis functions. For the efficiency of a method it is therefore desirable to get along with a minimal basis, where each atomic orbital (AO) is represented only by a single basis function $\eta(r)$. The orbitals of a free atom are quite diffuse and not very well suited for the description of bonded chemical systems like solids, molecules, or clusters. The presence of neighboring atoms in these systems confines the AOs compared to the free AOs in vacuo. In DFTB one uses therefore an optimized minimal basis which is constructed by solving Kohn-Sham equations of the single atoms within an additional confining potential

$$\left(-\frac{1}{2}\nabla^2 + v_{\text{eff}}(\rho_{\text{atom}}) + \left(\frac{r}{r_0}\right)^2 \right) \eta_\mu(r) = \epsilon_\mu \eta_\mu(r) \quad (2.22)$$

where the empirical parameter r_0 is roughly twice the covalent radius of the atom.

Another difference to DFT calculations is the way how the density-dependent Kohn-Sham matrix elements in eq. 2.18 are constructed. The trick of DFTB1 is to use a known reference density, namely the sum of neutral atomic densities.

$$\rho_0(r) = \sum_\alpha \rho_\alpha(r) \quad (2.23)$$

Additionally, a two-center approximation is introduced, which means that only the density of the atoms α and β on which the AOs η_μ and η_ν are located is considered in the

Hamilton matrix elements

$$H_{\mu\nu} = \langle \eta_\nu | \hat{H}[\rho_0] | \eta_\mu \rangle = \langle \eta_\nu | \hat{H}[\rho_\alpha + \rho_\beta] | \eta_\mu \rangle \quad (2.24)$$

Since in this approximation the integrals $H_{\mu\nu}$ and $S_{\mu\nu}$ depend only on two atoms, they can be tabulated for various atom-pairs up to a distance where they vanish due to the exponential decay of the AOs. During an actual DFTB calculation, the tabulated integrals can just be read and do not have to be calculated explicitly like in DFT calculations. Depending on the relative orientation of the atoms the integrals have to be transformed according to the Slater-Koster rules.⁵⁷

By comparing with the DFT total energy for this reference system

$$E[\rho_0] = \sum_i^{occ} \epsilon_i - \frac{1}{2} \iint \frac{\rho_0(r)\rho_0(r')}{|r-r'|} dr dr' - \int v_{xc}(r)\rho_0(r)dr + E_{xc}[\rho_0] + E_{nn} \quad (2.25)$$

which is the electronic energy shown in equation 2.21 plus the nuclear-nuclear repulsion energy $E_{nn} = \frac{1}{2} \sum_{\alpha\beta} \frac{Z_\alpha Z_\beta}{R_{\alpha\beta}}$, we realize that we still need an expression for the last three terms, which are usually collected in a single repulsive energy term

$$E_{rep}[\rho_0] = \frac{1}{2} \sum_{\alpha\beta} V_{\alpha\beta}(R_{\alpha\beta}) \quad (2.26)$$

A simple approach for fitting the repulsive potential $V_{\alpha\beta}$ between two atoms α and β would be performing DFT and DFTB calculations at different interatomic distances $R_{\alpha\beta}$ and fit the potential such that

$$V_{\alpha\beta}(R_{\alpha\beta}) = E_{tot}^{DFT}(R_{\alpha\beta}) - \sum_i \epsilon_i^{DFTB} \quad (2.27)$$

In practice, however, a single system is insufficient to provide a transferable repulsive potential. Consequently, the repulsive potential has to be fitted on a whole set of molecular structures, which is the most difficult task of parameterizing DFTB. The total energy at the DFTB1 level is thus

$$E[\rho_0] = \sum_i \epsilon_i + E_{rep}[\rho_0] \quad (2.28)$$

Self-Consistent Charges

The reference density, composed of neutral atomic densities, is reasonable as long as little charge gets transferred between the atoms. In cases where significant charge transfer between the atoms occurs, one has to explicitly consider these density fluctuations. In DFTB2 the total energy of the system is expressed as second-order Taylor expansion of the DFT energy with respect to density fluctuations $\delta\rho$ around the reference density ρ_0 .

$$E[\rho] = \sum_i^{occ} \langle \phi_i | \hat{H}[\rho_0] | \phi_i \rangle - \frac{1}{2} \iint' \frac{\rho_0(r)\rho_0(r')}{|r-r'|} - \int v_{xc}(r)\rho_0(r) + E_{xc}[\rho_0] + E_{nn} \\ + \frac{1}{2} \iint' \left(\frac{1}{|r-r'|} + \frac{\delta^2 E_{xc}}{\delta\rho\delta\rho'} \Big|_{\rho=\rho_0} \right) \delta\rho\delta\rho' \quad (2.29)$$

where \int' is short for $\int dr'$. The first term can be expanded as

$$\langle \phi_i | \hat{H}[\rho_0] | \phi_i \rangle = \sum_{\mu\nu} c_\mu^i c_\nu^i H_{\mu\nu}^0 \quad (2.30)$$

where $H_{\mu\nu}^0$ are again the DFTB1 matrix elements. The rest of the first line of eq. 2.29 is just the repulsive potential, which was introduced in eq. 2.26. The only new terms at the DFTB2 level are in the last line of eq. 2.29, .

Like the reference density $\rho_0(r)$ in eq. 2.23, also the density variation $\delta\rho$ is divided into atomic contributions

$$\delta\rho = \sum_\alpha \delta\rho_\alpha \quad (2.31)$$

Moreover, a charge monopole approximation is used to represent the atomic density fluctuations ρ_α

$$\delta\rho_\alpha \approx \Delta q_\alpha F_{00}^\alpha Y_{00} \quad (2.32)$$

where F_{00}^α denotes the normalized radial distribution function of the density and Y_{00} is the angular distribution, which is spheric. Within this approximation the second-order term can be expressed as

$$E_{2nd} \approx \frac{1}{2} \sum_{\alpha\beta} \Delta q_\alpha \Delta q_\beta \iint' \left(\frac{1}{|r-r'|} + \frac{\delta^2 E_{xc}}{\delta\rho\delta\rho'} \Big|_{\rho=\rho_0} \right) F_{00}^\alpha F_{00}^\beta Y_{00}^2 \quad (2.33)$$

Even though this expression looks quite complicated, we can still identify two limiting

cases. First, for large distances between the atoms α and β the exchange-correlation term vanishes* and the summands in eq. 2.33 become

$$\gamma_{\alpha\beta}(R_{\alpha\beta} \rightarrow \infty) = \frac{\Delta q_{\alpha} \Delta q_{\beta}}{R_{\alpha\beta}} \quad (2.34)$$

which describes the regular Coulomb interaction between two partial atomic charges Δq_{α} and Δq_{β} which decays with $1/R_{\alpha\beta}$. Second, for vanishing interatomic distance, i.e. if $\alpha = \beta$, the terms in eq. 2.33 describe the electron-electron interaction on a single atom

$$\gamma_{\alpha\alpha}(R_{\alpha\alpha} = 0) = U_{\alpha} = \frac{\partial^2 E_{\alpha}}{\partial^2 q_{\alpha}} \quad (2.35)$$

where U_{α} is the Hubbard parameter or chemical hardness of atom α . An approximation that interpolates between these extreme cases was proposed by Klopman and Ohno^{58,59}

$$\gamma_{\alpha\beta}(R_{\alpha\beta}) = \frac{1}{\sqrt{R_{\alpha\beta} + \frac{1}{4} \left(\frac{1}{\gamma_{\alpha\alpha}} + \frac{1}{\gamma_{\beta\beta}} \right)^2}} \quad (2.36)$$

With the approximations for the second-order terms the DFTB2 total energy can be written as

$$E[\rho] = E_0[\rho_0] + E_{2nd}[\delta\rho] \quad (2.37)$$

$$= \sum_i \sum_{\mu\nu}^{occ} c_{\mu}^i c_{\nu}^i H_{\mu\nu}^0 + E_{rep}[\rho_0] + \frac{1}{2} \sum_{\alpha\beta} \Delta q_{\alpha} \Delta q_{\beta} \gamma_{\alpha\beta}(R_{\alpha\beta}) \quad (2.38)$$

For the calculation of Δq_{α} Mulliken charges are used in DFTB, where

$$q_{\alpha} = \frac{1}{2} \sum_i \sum_{\mu \in \alpha, \nu}^{occ} (c_{\mu}^{i*} c_{\nu}^i + c.c.) S_{\mu\nu} \quad (2.39)$$

are the number of electrons on atom α . Hence $\Delta q_{\alpha} = q_{\alpha} - q_{\alpha}^0$, where q_{α}^0 is the number of valence electron on atom α .

The variation of eq. 2.38 with respect to the coefficients c_{μ}^i under the constraint that the norm is conserved gives rise to the equivalent to the Kohn-Sham equations in DFTB,

*This is at least the case if one assumes semi-local exchange-correlation like it is the case for GGA functionals. Exact exchange decays also with $1/r$

where the matrix elements $H_{\mu\nu}$ are obtained as

$$H_{\mu\nu} = H_{\mu\nu}^0 + \frac{1}{2}S_{\mu\nu} \sum_{\xi} \Delta q_{\xi} (\gamma_{\alpha\xi} + \gamma_{\beta\xi}) \quad (2.40)$$

where AO μ is located on atom α and AO ν on atom β . The elements of the DFTB2 Hamilton matrix depend on the charges Δq , similar to the elements of the Kohn-Sham Hamiltonian, which depend on the density. Therefore, also DFTB2 calculations have to be performed self-consistently.

QM/MM-Coupling

In simulations of large molecular complexes it is often sufficient to treat only the important part of the system with quantum mechanics (QM), whereas the remainder of the system can be modeled with classical molecular mechanics (MM). In such QM/MM simulations the quantum region is polarized by the classical point charges of the MM region. By considering also the external MM point charges Q_A in the DFTB2 Hamiltonian we can write⁶⁰

$$H_{\mu\nu} = H_{\mu\nu}^0 + \frac{1}{2}S_{\mu\nu} \left(\sum_{\xi} \Delta q_{\xi} (\gamma_{\alpha\xi} + \gamma_{\beta\xi}) + \sum_A Q_A \left(\frac{1}{r_{\alpha A}} + \frac{1}{r_{\beta A}} \right) \right) \quad (2.41)$$

2.1.3. Self-Interaction Error of DFT

Perdrew et al. studied the total energy of a system with fractional charge, which can be described as ensemble of states with integral number of electrons. They showed that the total energy has to follow a straight line between the states with integer electrons (see figure 2.1).⁶¹ The slope of the line that connects the energy of the systems with integer charges can be identified as the ionization potential

$$E(N) - E(N - 1) = -I \quad (2.42)$$

and the electron affinity

$$E(N + 1) - E(N) = -A \quad (2.43)$$

of the N electron system.

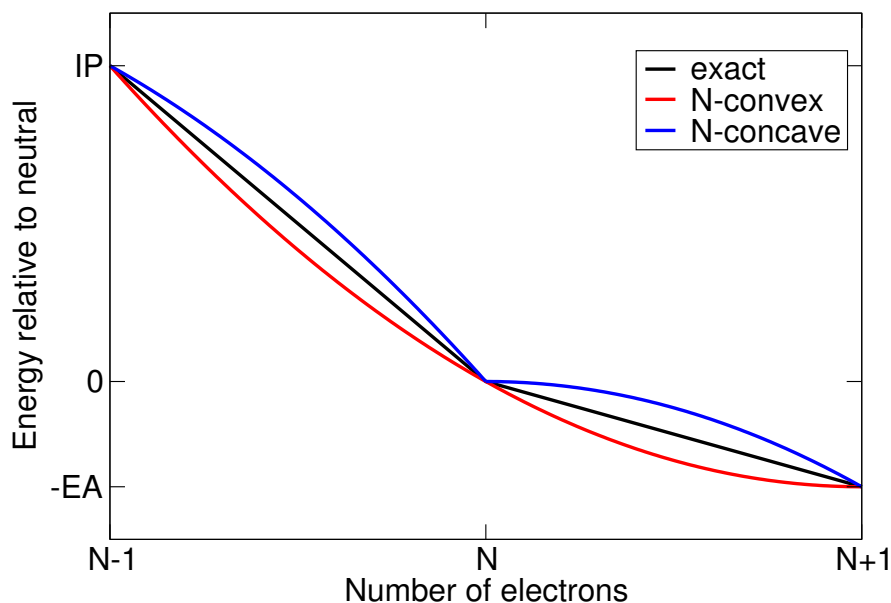


Figure 2.1.: Total energy for a (fractional) number of electrons.

Furthermore, it can be shown that a variation of electron number N has to result only in a variation of the occupation of frontier orbitals n ⁶²

$$\frac{\partial E(N)}{\partial N} = \begin{cases} \frac{\partial E}{\partial n_{LUMO}} & \text{for } \delta N > 0 \\ \frac{\partial E}{\partial n_{HOMO}} & \text{for } \delta N < 0 \end{cases} \quad (2.44)$$

In combination with Janak's theorem,⁶³ which states that the variation of the total energy with respect to an orbital occupation is equal to the eigenvalue of that orbital, we can identify the slopes also with the orbital energies of HOMO and LUMO

$$\frac{\partial E(N)}{\partial N} = \begin{cases} \epsilon_{LUMO} & \text{for } \delta N > 0 \\ \epsilon_{HOMO} & \text{for } \delta N < 0 \end{cases} \quad (2.45)$$

Approximate methods, however, deviate from the exact straight line. For example DFT using GGAs shows a convex behavior, whereas Hartree-Fock calculations show a concave behavior.⁶⁴ The deviation in DFT is due to the approximate exchange-correlation and often termed self-interaction (SI). Some of the effects of SI are that dissociation curve of symmetric ionic radicals are incorrect,⁶⁵ charge-transfer complexes are often not well described,⁶⁶ and delocalized states are artificially stabilized.⁶⁷

The reason for this self-interaction can be seen on a single-electron system. Even with

only one electron we get a contribution from the coulomb integral in eq. 2.7

$$J[\rho] = \frac{1}{2} \int \frac{\rho(r)\rho(r')}{|r-r'|} dr dr' \quad (2.46)$$

This electron should, however, only see the density of (N-1) electrons instead of the total density, i.e. zero electrons in this case. In principle the exchange-correlation functional should correct this problem because it is part of its definition (see 2.10), but since we only know approximations to the real $E_{xc}[\rho]$, a spurious interaction of the electron with itself remains. In the case of local functionals, which depends only on the electron density at r , the exchange-correlation potential $v_{xc}[\rho](r)$ decays exponentially like the density, whereas the exact $v_{xc}[\rho](r)$ has to decay with $1/r$ in order to cancel the Hartree potential $v_H[\rho](r)$.

Note that like for DFT, also the DFTB2 total energy shows a convex behavior, which is in this case originating from the second-order terms.

$$E^{DFTB2} = \sum_i^{occ} \langle \phi_i | H_0 | \phi_i \rangle + \frac{1}{2} \sum_{AB} \gamma_{AB} \Delta q_A \Delta q_B \quad (2.47)$$

These terms appear by expanding the total energy around a reference density. Also the orbital energies depend on the fractional charge via the charge-dependent Hamiltonian

$$H_{\mu\nu} = H_{\mu\nu}^0 + \frac{1}{2} S_{\mu\nu} \sum_{\xi} \Delta q_{\xi} (\gamma_{\alpha\xi} + \gamma_{\beta\xi}) \quad (2.48)$$

Therefore, by using the DFTB2 formalism for partially charged systems an artificial stabilization emerges as was discussed in detail in ref. 68.

2.1.4. Molecular Mechanics

With quantum chemical methods a lot of informations about a system are accessible, like e.g. excitation energies, polarizabilities, or ionization potentials. For large systems, quantum mechanical calculations become prohibitive slow, since they usually scale with N^3 , where N is the number of atoms in the system. In many cases, however, only molecular geometries with the corresponding energy are needed, whereas informations about the electronic structure are dispensable. This goal can be achieved with molecular mechanics (MM) at a fraction of cost by treating molecules classically. In this method atoms are approximated as spheres carrying partial charges and their interactions are

described by parameterized potentials. Since the properties of an atom are dependent on its chemical environment, atoms are not only classified by their element, but instead they are described as so-called 'atom-types'. One distinguishes for example sp^1 - sp^2 - und sp^3 -hybridized carbon atoms or metal atoms in different oxidation states. The potential energy is usually divided in bonded and non-bonded interactions between the atoms.

$$V_{MM}^{tot} = V_{bonded} + V_{non-bonded} \quad (2.49)$$

The functional form and parameter set that describes the interactions is termed 'force field'. In the following we will discuss the force-fields of the AMBER family, like GAFF⁶⁹ and OPLS,^{70,71} which are applied in this work.

Bonded Interactions

The bonded interactions describe the energy with respect to all bond lengths, angles and dihedral angles of a molecule.

$$V_{bonded} = \sum_{bonds} V_b(R) + \sum_{angles} V_a(\theta) + \sum_{dihedral} V_d(\phi) + \sum_{improper} V_{id}(\xi) \quad (2.50)$$

The chemical bonds between atom i and j are approximated as harmonic potential around an equilibrium length R_{ij}^0 with force constant k_{ij}^b

$$V_b(R_{ij}) = \frac{1}{2} k_{ij}^b (R_{ij} - R_{ij}^0)^2 \quad (2.51)$$

Also the deformation of the angles θ between bond ij and jk are approximated harmonically.

$$V_a(\theta_{ijk}) = \frac{1}{2} k_{ijk}^a (\theta_{ijk} - \theta_{ijk}^0)^2 \quad (2.52)$$

The periodic potential for the torsion around a single bond jk is expanded in a Fourier series

$$V_d(\phi_{ijkl}) = \sum_n k_{ijkl}^n (1 + \cos(n\phi_{ijkl} - \phi_{ijkl}^0)) \quad (2.53)$$

where $n = \{1, 2, 3\}$ describes a periodicity of 360° , 180° and 120° , respectively, ϕ_{ijkl} is the angle between the planes of atom ijk and jkl , and ϕ_{ijkl}^0 is the phase shift. This term is also called proper dihedral potential. The planarity of e.g. π -conjugated molecules, on

the other hand, is enforced by a harmonic improper dihedral potential

$$V_{id}(\xi_{ijkl}) = \frac{1}{2}k_{ijkl}(\xi_{ijkl} - \xi_{ijkl}^0)^2 \quad (2.54)$$

where k_{ijkl} is a relatively high force constant.

Non-Bonded Interactions

The non-bonded terms in the potential energy consist of a Coulomb potential for electrostatic interactions and the Lennard-Jones potential, which describes Pauli-Repulsion and vdW interactions.

$$V_{non-bonded} = V_{LJ}(R) + V_{el}(R) \quad (2.55)$$

Contributions from atoms, which are separated by less than four bonds are not considered because their electrostatic and Lennard-Jones interactions are already contained in the parameterization of the bonded interactions.

The Lennard-Jones potential between two atoms i and j is given as

$$V_{LJ}(R_{ij}) = 4\epsilon_{ij} \left(\left(\frac{\sigma_{ij}}{R_{ij}} \right)^{12} - \left(\frac{\sigma_{ij}}{R_{ij}} \right)^6 \right) \quad (2.56)$$

where ϵ_{ij} is the depth of the potential minimum, which is located at an interatomic distance of $R_{ij} = \sqrt[6]{2}\sigma_{ij}$. These parameters are obtained from atom-specific parameters of atom i and j following force-field-dependent combinations rules like the geometric mean in case of the OPLS force field.

$$\epsilon_{ij} = \sqrt{\epsilon_{ii}\epsilon_{jj}} \quad (2.57)$$

$$\sigma_{ij} = \sqrt{\sigma_{ii}\sigma_{jj}} \quad (2.58)$$

$$(2.59)$$

The electrostatic interaction between two atomic point charges q_i and q_j at distance R_{ij} is given by

$$V_{el}(R_{ij}) = \frac{1}{4\pi\epsilon_0\epsilon_R} \frac{q_i q_j}{R_{ij}} \quad (2.60)$$

where ϵ_0 and ϵ_R are the vacuum and relative permittivity, respectively. These interactions decay only with $1/R$ and thus converge slowly. The summation can be cut-off at a certain distance or in periodic systems the particle mesh Ewald (PME) method can be used for

full-range electrostatics by using a Fourier transformation for the calculation of long-range interactions.

Molecular Dynamics Simulation

Quantum chemical calculations are often performed on the equilibrium structure. At finite temperature, however, the optimized conformation loses relevance and thermodynamic ensemble-averages become important. Accurate prediction of macroscopically observable quantities therefore requires sufficient sampling of the phase-space. For ergodic systems, i.e. when the average over time and the average over the statistical ensemble are the same, we can obtain such an ensemble of structures by propagating the nuclear degrees of freedom using MD simulations. The initial state of a given system is defined by the starting positions R_i and velocities v_i of all atoms i . New positions and velocities at time t are obtained iteratively via the leap-frog algorithm⁷²

$$v(t + \frac{1}{2}\Delta t) = v(t - \frac{1}{2}\Delta t) + \frac{\Delta t}{m}F(t) \quad (2.61)$$

$$R(t + \Delta t) = R(t) + \Delta t v(t + \frac{1}{2}\Delta t) \quad (2.62)$$

where Δt is the time step between each iteration, and the force on atom i is the negative derivative of the total potential energy (eq. 2.49) with respect to the coordinates R_i

$$F_i = -\frac{\partial V_{MM}^{tot}}{\partial R_i} \quad (2.63)$$

Propagation with these equations of motions yields a microcanonical ensemble. For the simulation of different thermodynamic ensembles it is necessary to keep e.g. the temperature and/or pressure constant. For this task there exists a variety of thermostats and barostats, which achieve this goal by scaling the velocities and system size, respectively.⁷³⁻⁷⁷

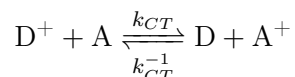
2.2. Electronic States and Couplings

Application of the Born-Oppenheimer approximation and diagonalization of the electronic Hamiltonian yields the electronic eigenstates, which are by construction electronically decoupled (adiabatic). By considering also the nuclear Hamiltonian one can show that these adiabatic states are coupled via nuclear derivative couplings $\langle \Psi_i(r; R) | \nabla_R | \Psi_j(r; R) \rangle_r$,

where $\langle \rangle_r$ denotes integration over all electronic degrees of freedom. This means that by going beyond the Born-Oppenheimer approximation, any nuclear motion is coupled to electronic transitions between adiabatic states.

Diabatic states, on the other hand, are historically defined as states with vanishing derivative couplings ($\langle \Psi_a(r; R) | \nabla_R | \Psi_b(r; R) \rangle_r = 0$). Exactly diabatic states, however, do not exist in general⁷⁸ and therefore several alternative definitions of diabatic states can be found in the literature.^{79–84} Within the context of charge transfer, the diabatic states are usually defined as the orthogonalized states before and after the transfer process, where the excess charge is localized either at the donor D or acceptor A .

In the case where only two diabatic states are considered, the charge transfer can be described by a second order rate equation.



For simplicity we will assume in the following sections that D and A are neutral molecules with the same number of electrons N , i.e., in the initial state D has $N - 1$ electrons and A has N electrons, and vice versa for the final state.

The corresponding energy profile along the reaction coordinate is shown in fig. 2.2. The rate constant k_{CT} for this charge transfer reaction can be derived from Fermi's golden rule (or its approximations like Marcus theory shown in section 2.3.2)

$$k_{CT} = \frac{2\pi}{\hbar} |H_{ab}|^2 FC \quad (2.64)$$

where FC is the Franck-Condon factor describing the overlap of the nuclear wavefunctions of initial and final state and

$$H_{ab} = \langle \Psi_a | \hat{H} | \Psi_b \rangle \quad (2.65)$$

is the coupling between initial $|\Psi_a\rangle$ and final $|\Psi_b\rangle$ diabatic electronic states and \hat{H} is shown in eq. 2.2.

Adiabatic states, in contrast to diabatic states, diagonalize the electronic Hamiltonian and are therefore well defined and can be obtained with standard electronic structure methods. The energies of the diabatic states (E_a, E_b) are related to the potential energies

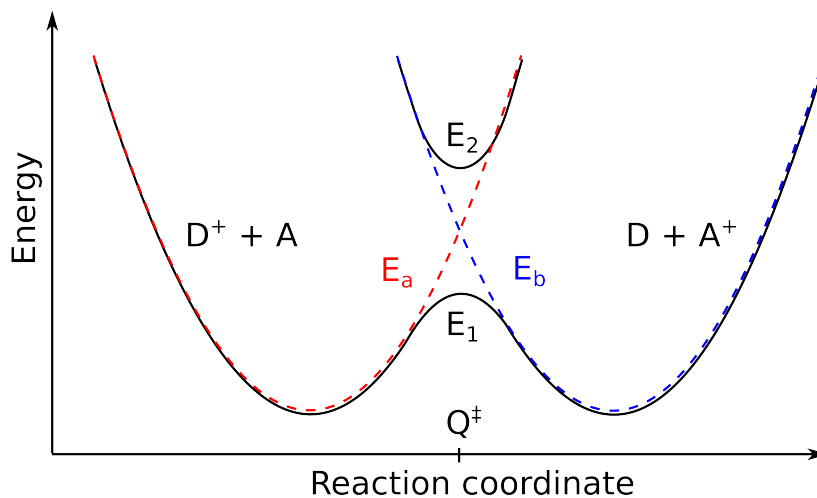


Figure 2.2.: Energy profile along the reaction coordinate between an initial diabatic state (dashed red), where the charge is localized on D , and a final state (dashed blue), where the charge is localized on A . Adiabatic ground and first excited state are shown as solid lines.

of the electronic ground state (E_1) and first excited state (E_2)⁸⁵

$$E_{1,2} = \frac{1}{2} \left(E_a + E_b \pm \sqrt{(E_a - E_b)^2 + 4|H_{ab}|^2} \right) \quad (2.66)$$

Hence for $E_a = E_b$, which is the case at point Q^\ddagger in fig. 2.2, we can obtain H_{ab} from the first excitation energy $\Delta E_{12} = E_2 - E_1$

$$\Delta E_{12} = 2|H_{ab}| \quad (2.67)$$

2.2.1. Generalized Mulliken-Hush

An extension to asymmetric cases where $E_a \neq E_b$ can be made with the generalized Mulliken-Hush (GMH) method.^{86,87} The diabatic states are obtained from the adiabatic states via a unitary transformation. Due to the localized character of diabatic states, it is assumed that the off-diagonal element of the dipole moment matrix vanishes in the diabatic basis. The same transformation that diagonalizes the dipole-moment matrix, expressed in the adiabatic basis, can thus be used to transform the adiabatic into diabatic states. After transforming the (diagonal) adiabatic Hamiltonian into the diabatic basis,

we obtain for the off-diagonal elements (electronic couplings)

$$|H_{ab}| = \frac{|\mu_{12}|\Delta E_{12}}{\sqrt{(\mu_{11} - \mu_{22})^2 + 4(\mu_{12})^2}} \quad (2.68)$$

where μ_{11} and μ_{22} denote the dipole moments of the ground and first excited states and μ_{12} is the transition dipole moment between these states. The GMH approach can be used in combination with any ab initio method but requires the costly calculation of excited states. Furthermore, for larger systems with more than two charge-localized centers in a non-collinear geometry, the localization of charge with the GMH method works less well.^{88,89} It is therefore obvious that computationally less expensive electronic structure methods have to be used if one would like to study large molecular systems, like a bulk of organic semiconducting molecules, especially if coupling calculations are carried out for a very large number of times (e.g. along an MD simulation).

2.2.2. Constrained Density Functional Theory

In constrained density functional theory (CDFT) the charge localized (diabatic) states are directly obtained by minimizing the total energy under a charge constraint N_C that is imposed on the density $\rho(r)$ by a spatial weight function $\omega(r)$.⁹⁰

$$N_C = \int \omega(r)\rho(r)dr \quad (2.69)$$

The weight function selects the region subjected to the charge constraint and its functional form is dependent on the charge definition that is used to fulfill the constraint. If we want to constrain for example the difference of Hirshfeld charges⁹¹ between donor and acceptor, $\omega(r)$ takes the form

$$\omega(r) = \frac{\sum_{i \in D} \rho_i(r - R_i) - \sum_{i \in A} \rho_i(r - R_i)}{\sum_{i=1}^n \rho(r - R_i)} \quad (2.70)$$

where the sums in the numerator run over all atoms of fragment D and A , respectively, whereas the sum in the denominator runs over all n atoms of the complex and $\rho_i(r - R_i)$ is the unperturbed (or pro-molecular) electron density of atom i .

By setting the constraint of the charge difference between donor and acceptor to $N_C = 1$ or $N_C = -1$ one obtains the initial and final diabatic state as a single determinant of

$2N - 1$ spin-orbitals

$$\begin{aligned}\Psi'_a &= \frac{1}{\sqrt{(2N-1)!}} \det(\phi_a^1 \dots \phi_a^{2N-1}) \\ \Psi'_b &= \frac{1}{\sqrt{(2N-1)!}} \det(\phi_b^1 \dots \phi_b^{2N-1})\end{aligned}\tag{2.71}$$

where the charge is entirely localized on donor or acceptor. The two states are in general non-orthogonal, which is why we distinguish them from the orthogonal states in eq. 2.65 by a prime.

With these states we can define the Hamilton matrix

$$\mathbf{H} = \begin{pmatrix} H_{AA} & H_{AB} \\ H_{BA} & H_{BB} \end{pmatrix}\tag{2.72}$$

with diagonal elements $H_{AA} = \langle \Psi'_A | \hat{H}[\rho_A] | \Psi'_A \rangle$ and $H_{BB} = \langle \Psi'_B | \hat{H}[\rho_B] | \Psi'_B \rangle$ and off-diagonal elements $H_{AB} = \langle \Psi'_A | \hat{H}[\rho_B] | \Psi'_B \rangle$ and $H_{BA} = \langle \Psi'_B | \hat{H}[\rho_A] | \Psi'_A \rangle$, where

$$\rho_A = \langle \Psi'_A | \Psi'_A \rangle\tag{2.73}$$

$$\rho_B = \langle \Psi'_B | \Psi'_B \rangle\tag{2.74}$$

Note that in eq. 2.72 the off-diagonal elements are only approximations to the exact electronic coupling in 2.65. On the one hand Ψ'_A and Ψ'_B are non-orthogonal, whereas Ψ_a and Ψ_b in eq. 2.65 are orthogonal by definition. Therefore, the matrix \mathbf{H} has to be transformed into an orthogonal basis first.⁹² On the other hand the exact Hamiltonian is approximated with the Kohn-Sham Hamiltonian, which is dependent on the charge. Therefore, for asymmetric systems $H_{AB} \neq H_{BA}$ in general, although the deviation from hermiticity is usually small. In such cases the coupling matrix element is taken as the average of the two off-diagonal elements.⁹³

2.2.3. Fragment Orbital Density Functional Theory

In CDFT calculations we first construct charge-localized states Ψ'_a and Ψ'_b , which are subsequently orthogonalized to obtain the final basis of diabatic states. In fragment orbital density functional theory (FODFT) calculations, on the other hand, the diabatic states are directly constructed by defining different occupations of an orthogonalized set of orbitals that are localized on donor or acceptor.

First, two sets of orbitals $\{\phi_A^i\}$ and $\{\phi_D^i\}$ are obtained from independent DFT calculations of the isolated donor and acceptor, performed in the respective geometries of the fragments in the DA complex. The orbitals within a single set are orthogonal by construction, whereas there is a small overlap between orbitals from different sets in general. The combined set of donor and acceptor orbitals $\{\phi_A^i; \phi_D^i\}$ is orthogonalized, e.g. with the method of Löwdin,⁹⁴ to yield an orthogonal (unprimed) set of orbitals $\{\phi_A^i; \phi_D^i\}$. The (orthogonal) diabatic states are then constructed as single Slater-determinant of $2N - 1$ spin orbitals by occupying the lowest orbitals of D and A such that the charge of the complex is either localized at donor or acceptor.

$$\Psi_a = \frac{1}{\sqrt{(2N - 1)!}} \det(\phi_D^1 \dots \phi_D^{N-1}, \phi_A^1 \dots \phi_A^N) \quad (2.75)$$

$$\Psi_b = \frac{1}{\sqrt{(2N - 1)!}} \det(\phi_D^1 \dots \phi_D^N, \phi_A^1 \dots \phi_A^{N-1}) \quad (2.76)$$

If the exact Hamiltonian \hat{H} can be expressed by independent-particle operators $\hat{H} = \sum_i \hat{h}(r_i)$, like in Kohn-Sham DFT[†], then⁹⁵

$$\langle \Psi_a | \hat{H}[\rho] | \Psi_b \rangle = \langle \phi_D^N | \hat{h}[\rho](r_{2N-1}) | \phi_A^N \rangle \quad (2.77)$$

This way we need to calculate only the integral between the HOMOs of D and A instead of the integral between two Slater-determinants like in CDFT.

FODFT with correct electron number

There exists a variety of FODFT methods, which differ e.g. in the number of electrons that enter the Kohn-Sham Hamiltonian in eq. 2.77 via the density ρ or in the orthogonalization procedure that is applied to the orbitals. In one realization,^{44,92,96} which is conceptual similar to the CDFT method, the correct number of electrons is used in the Kohn-Sham Hamiltonian during the calculation of the electronic couplings (eq. 2.77). Furthermore, one sets the electron number in the monomer calculations such that all orbitals in eq. 2.76 originate from occupied orbitals of the monomer calculations. This means each monomer is calculated with N electrons in the case of hole transfer and with $N + 1$ electrons in the case of electron transfer.

[†]Note that the equality is only true for the exact functional. For any approximate exchange-correlation functional eq. 2.77 is only approximately true.

Since the KS-Hamiltonian is state dependent, we can again construct two Hamiltonians, $\hat{H}[\rho_\alpha] = \sum_i \hat{h}[\rho_\alpha](r_i)$ and $\hat{H}[\rho_\beta] = \sum_i \hat{h}[\rho_\beta](r_i)$ where

$$\rho_A = \sum_i^N \langle \phi_D^i | \phi_D^i \rangle + \sum_i^{N-1} \langle \phi_A^i | \phi_A^i \rangle \quad (2.78)$$

$$\rho_B = \sum_i^{N-1} \langle \phi_D^i | \phi_D^i \rangle + \sum_i^N \langle \phi_A^i | \phi_A^i \rangle \quad (2.79)$$

A matrix, which is similar to the CDFT matrix in eq. 2.72, can then be constructed

$$\mathbf{H} = \begin{pmatrix} h_{AA} & h_{AB} \\ h_{BA} & h_{BB} \end{pmatrix} \quad (2.80)$$

with diagonal elements $h_{AA} = \langle \phi_A | h_{KS}[\rho_A] | \phi_A \rangle$ and $h_{BB} = \langle \phi_B | h_{KS}[\rho_B] | \phi_B \rangle$ and off-diagonal elements $h_{AB} = \langle \phi_A | h_{KS}[\rho_B] | \phi_B \rangle$ and $h_{BA} = \langle \phi_B | h_{KS}[\rho_A] | \phi_A \rangle$. Note that this way, the correct number of electrons is considered in the Hamiltonian, which is $2N - 1$ electrons for hole transfer and $2N + 1$ electrons for electron transfer. However, this Hamilton matrix is again not guaranteed to be hermitian, as we have already discussed for CDFT, and averaging of the off-diagonal elements may become necessary.

FODFT of the neutral system

In another common realization^{97,98} of the FODFT method, the calculations for both hole and electron transfer (with formally $2N - 1$ and $2N + 1$ electrons in system, respectively) are performed on the neutral system with $2N$ electrons. Consequently, one difference arises in the generation of the MOs in the case of electron transfer. Now an unoccupied MO (LUMO) is used in the construction of the Slater-determinant (eq. 2.76) instead of the HOMO of a anionic monomer with $N + 1$ electrons. The second difference arises in the Hamilton matrix of eq. 2.80, in which the density of the neutral system is entering

$$\rho = \sum_i^N \langle \phi_D^i | \phi_D^i \rangle + \sum_i^N \langle \phi_A^i | \phi_A^i \rangle \quad (2.81)$$

instead of the state-dependent densities ρ_A and ρ_B .

2.3. Charge Transport Models

OSCs are flexible materials consisting of weakly interacting molecules. The important physics can therefore be formulated in terms of molecular sites and their nuclear vibrations. A general Hamiltonian for the description of charge transport can then be given as⁹⁹

$$H = H_{el}^0 + H_{ph}^0 + V_{el} + V_{el-ph}^{local} + V_{el-ph}^{nonlocal} + V_{impurities} \quad (2.82)$$

$$H_{el}^0 + V_{el} = \sum_j \epsilon_j a_j^\dagger a_j + \sum_{ij} \tau_{ij} a_i^\dagger a_j \quad (2.83)$$

$$H_{ph}^0 = \sum_{\mathbf{ql}} \hbar \omega_{\mathbf{ql}} \left(b_{\mathbf{ql}}^\dagger + b_{\mathbf{ql}} + \frac{1}{2} \right) \quad (2.84)$$

$$V_{el-ph}^{local} = \sum_{\mathbf{ql}} \sum_j g_{jj,\mathbf{ql}} \hbar \omega_{\mathbf{ql}} \left(b_{\mathbf{ql}}^\dagger + b_{\mathbf{ql}} \right) a_j^\dagger a_j \quad (2.85)$$

$$V_{el-ph}^{nonlocal} = \sum_{\mathbf{ql}} \sum_{i \neq j} g_{ij,\mathbf{ql}} \hbar \omega_{\mathbf{ql}} \left(b_{\mathbf{ql}}^\dagger + b_{\mathbf{ql}} \right) a_i^\dagger a_j \quad (2.86)$$

Here, H_{el}^0 is the electronic Hamiltonian of the noninteracting molecules with site energy ϵ , V_{el} describes the electronic inter-site coupling τ_{ij} , and, a_j^\dagger and a_j are the creation and annihilation operators of a charge carrier on site j , respectively. H_{ph}^0 is the nuclear Hamiltonian of the unperturbed vibrations with frequency $\omega_{\mathbf{ql}}$ and $b_{\mathbf{ql}}^\dagger$ and $b_{\mathbf{ql}}$ are the creation and annihilation operators for a phonon with wavevector \mathbf{q} in mode l . V_{el-ph}^{local} is the local (Holstein) electron-phonon coupling and describes how the occupation of site j leads to a relaxation of its nuclear structure. $V_{el-ph}^{nonlocal}$ is the non-local (Peierls) coupling which describes the dependence of the electronic coupling on the nuclear modes.

Depending on the importance of the individual terms for different systems, one can apply reasonable approximations, which gives rise to a variety of CT models. For a detailed review see Ref. 29 and 99. Here, we focus only on few models, which will be addressed later in this work.

In the presence of static disorder and weak electronic coupling between the molecules the electronic states become localized. The charge transport then takes place in the hopping regime, where the charge carrier gets occasionally transferred between neighboring molecules. For these disordered system there exist two different models for the derivation of hopping rates, which will be briefly summarized in section 2.3.1 and 2.3.2. The Miller-Abrahams equation is valid at low temperatures and for weak electron-phonon coupling,

whereas the Marcus equation is valid at high temperatures and for large electron-phonon coupling.²⁵ In cases where all terms of eq. 2.82 are equally important and the temperature is sufficiently high, we can apply a semi-classical approximation. Within this approximation we can propagate the nuclei classically and need the time-dependent Schrödinger equation only for the excess charge carrier (see section 2.3.3).

2.3.1. Miller-Abrahams Rates and Gaussian Disorder Model

In 1960 Miller and Abrahams derived rate equations for phonon-induced electron hopping between impurities in inorganic semiconductors, i.e. trap states.¹⁰⁰ In the context of CT in organic semiconductors the rate is usually written as¹⁰¹

$$k_{ij} = \nu_0 \exp(-2\gamma R_{ij}) \begin{cases} \exp\left(-\frac{(\epsilon_j - \epsilon_i)}{k_B T}\right) & \text{for } \epsilon_j > \epsilon_i \\ 1 & \text{for } \epsilon_j \leq \epsilon_i \end{cases} \quad (2.87)$$

where ν_0 is the phonon vibration frequency, which can be understood as the jump-attempt rate or simply taken as a normalization factor, γ is a decay parameter describing the decreasing coupling between two sites with distance R_{ij} , and ϵ_i is the energy of the charge carrier on site i .

In his pioneering studies of hopping transport in disordered polymers Bässler used these rates in Kinetic Monte Carlo simulations in order to calculate charge carrier mobilities and their temperature dependence.¹⁰¹ In his so called Gaussian disorder model the site energies ϵ_i in eq. 2.87 are assigned according to a Gaussian distribution

$$\rho(\epsilon) = \frac{1}{\sqrt{2\pi\sigma^2}} \exp\left(-\frac{\epsilon^2}{2\sigma^2}\right) \quad (2.88)$$

where σ is the standard deviation of the site energies. A Gaussian shape for the density of states is a plausible assumption that is supported by the observation that the low energy tail of the absorption spectrum of disordered polymers can be fitted well to Gaussian envelope functions.

The model predicts a non-Arrhenius like temperature dependence for the mobility.

$$\mu(T) = \mu_0 \exp\left(-\left(\frac{2\sigma}{3k_B T}\right)^2\right) \quad (2.89)$$

However, in practice the parameters in the Miller-Abrahams rates as well as the standard deviation of the site energies are fitted to experimental values. Consequently the model can be used to rationalize experimental findings, but is unable to provide guidelines for the modification of chemical compounds in order improved their performance.

2.3.2. Marcus Rates

A more sophisticated description of hopping processes can be achieved by Marcus theory,^{102–104} which was initially derived for charge transfer processes in solvated metal complexes and later became popular in the description of CT in biological systems¹⁰⁵ and OSCs.^{25,30}

As shown in figure 2.3, the free energy surface of initial and final diabatic state are approximated by two parabolas. Thermal fluctuation allow the system to reach the crossing region Q^\ddagger , where the transition between initial and final state takes place with a probability depending on the electronic coupling. Subsequently the system relaxes to the minimum of the final state. The rate for this process is given as

$$k_{ET} = \frac{2\pi}{\hbar} |H_{ab}|^2 \frac{1}{\sqrt{4\pi\lambda k_B T}} \exp\left(-\frac{\Delta G^\ddagger}{k_B T}\right) \quad (2.90)$$

where H_{ab} is the electronic coupling between initial and final state, and the reorganization energy λ equals to the energy needed to transform the system coordinates into the final state without charge transfer taking place. The activation free energy ΔG^\ddagger for this reaction can be obtained as

$$\Delta G^\ddagger = \frac{(\Delta G^0 + \lambda)^2}{4\lambda} \quad (2.91)$$

The assumptions made in 2.90 are weak donor-acceptor coupling, classical harmonic nuclear motions, the Born-Oppenheimer approximation and that the transfer process takes place from a thermally fully equilibrated state with respect to the conformational dynamics of the system. However, even in cases where these assumptions become questionable and rates according to 2.90 therefore become unreliable, the three parameters still serve as elementary descriptors of a charge transfer system.

The electronic coupling can be obtained by the methods described in section 2.2 whereas structural fluctuation in soft matter usually lead to large fluctuations of H_{ab} along a trajectory, which makes statistical sampling and averaging necessary.¹⁰⁶ Thermodynamic

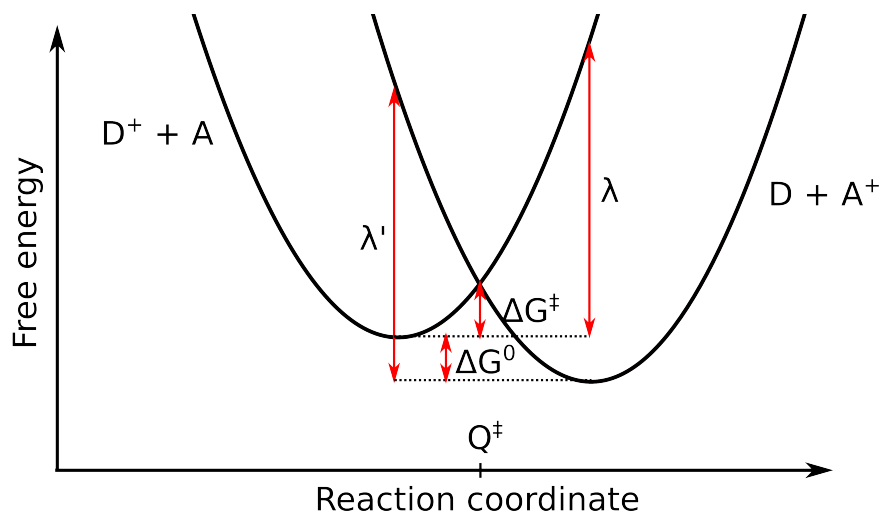


Figure 2.3.: Free energy profile for a donor acceptor system according to Marcus theory. The reorganization energy λ defines the curvature of the parabolas and ΔG_0 is the free energy difference between the initial and final state. Both parameters together define the activation free energy ΔG^\ddagger for the reaction over the transition state Q^\ddagger .

quantities like ΔG_0 can be computed e.g. from free energy methods like thermodynamic integration. The reorganization energy is usually divided in an inner-sphere (λ_i) contribution, describing the relaxation of donor and acceptor geometry, and an outer-sphere (λ_o) contribution, which captures the relaxation of the environment.

The internal part λ_i is usually computed quantum chemically as

$$\lambda_i = [E_{D^+}(D) + E_A(A^+)] - [E_D(D) + E_{A^+}(A^+)] \quad (2.92)$$

where the subscript indicates that the calculations are performed for the neutral or cationic state, respectively, and the argument in the bracket indicates for which state the geometry was optimized.

In outer-sphere reorganization energy was originally obtained by approximating the environment with a polarizable continuum

$$\lambda_o = (\Delta q)^2 \left(\frac{1}{2R_D} + \frac{1}{2R_A} - \frac{1}{R_{DA}} \right) \left(\frac{1}{\epsilon_{op}} + \frac{1}{\epsilon_s} \right) \quad (2.93)$$

where Δq is the charge transferred from one reactant to the other, R_A and R_B are the radii of the two (spherical) reactants separated by R_{DA} , and ϵ_{op} and ϵ_s are the optical and static dielectric constants of the environment. The molecular structure of the envi-

ronment can be taken into account explicitly by performing MD simulations of the initial and final state and then reevaluating the obtained trajectories on the energy surface of the opposite charge state, respectively.¹⁰⁷

$$\lambda_o = \langle E_{D^+A}^{FF} \rangle_{DA^+} - \langle E_{D^+A}^{FF} \rangle_{D^+A} \quad (2.94)$$

Here, the index within the brackets denotes the charge state that is represented by the force field, whereas the outer index represents the structural ensemble (trajectory) on which the reevaluation is carried out. Note that the parabolas in figure 2.3 are assumed to have the same curvature, which means that $\lambda = \lambda'$. If D and A (or their respective environment) differ strongly, then this is no longer the case in general and λ is usually taken as average value.

One surprising feature of Marcus theory is the prediction of an inverted region, which was later also confirmed experimentally.¹⁰⁸ Contrary to the usual increase of the rate with increasing thermodynamical driving force $-\Delta G_0$, the transfer becomes activation-less for $-\Delta G_0 = \lambda$ and starts to decrease once $-\Delta G_0 > \lambda$, as can be seen from eq. 2.91.

2.3.3. Coarse Grained Electron Ion Dynamics

The Hamiltonian shown in eq. 2.82 or approximations thereof are often used in simple parametrized models. For a quantitative modeling of the involved interplay between nuclear structure and electronic properties, however, simulations with atomistic resolution are necessary. Quantum chemical simulations for large systems are computationally very expensive when treated atomistically. A method which reduces the cost for these atomistic simulations is the coarse-graining of the electronic structure.

Coarse-graining builds a natural basis for the description of CT in molecular systems and allows for further corrections as we discuss in section 5.6 This model can be used in different propagation methods like mean-field (or Ehrenfest) simulations¹⁰⁹ or in surface-hopping simulations.¹¹⁰

In its derivation, the model follows closely the concept of DFTB2, and it introduces further approximations. It can be considered as a coarse-grained variant of DFTB, where molecular fragments take the role of single atoms. Similarly to the DFTB2 total energy in eq. 2.37, the energy of the charged system $E^+[\rho]$, where the excess charge is missing in HOMO Ψ_0 , is expanded around the energy of a neutral reference system $E^0[\rho_0]$ by

considering charge fluctuations up to the second order $E_{2nd}[\delta\rho]$

$$E^+[\rho] \approx E^0[\rho_0] - \langle \Psi_0 | \hat{H}[\rho_0] | \Psi_0 \rangle + E_{2nd}[\delta\rho] \quad (2.95)$$

As a further approximation the energy of the neutral system is represented by a classical force-field energy

$$E^0[\rho_0] \approx E_{MM} \quad (2.96)$$

The coarse-grained hole wavefunction is expanded in the HOMO orbitals of the neutral M fragments instead of atomic orbitals.

$$|\Psi_0\rangle \approx \sum_M a_M \phi_M^{HOMO} \quad (2.97)$$

This leads to a linear scaling with the number of fragments and allows furthermore the parallel computation of all monomers. With this basis set expansion we obtain the CT matrix elements as

$$\langle \Psi_0 | \hat{H}[\rho_0] | \Psi_0 \rangle = \sum_{MN} a_M^* a_N \langle \phi_M | \hat{H}[\rho_0] | \phi_N \rangle = \sum_{MN} a_M^* a_N H_{MN}^0 \quad (2.98)$$

which can be seen as coarse-grained version of eq. 2.30.

The density variation $\delta\rho$ relative to the neutral reference system is decomposed into contributions from each fragment

$$\delta\rho = \sum_M \delta\rho_M \quad (2.99)$$

which leads to a coarse-grained version of the second-order energy term of eq. 2.29

$$E_{2nd} = \frac{1}{2} \iint' \left(\frac{1}{|r - r'|} + \left. \frac{\delta^2 E_{xc}}{\delta\rho\delta\rho'} \right|_{\rho=\rho_0} \right) \delta\rho\delta\rho' dr dr' \quad (2.100)$$

The density variations $\delta\rho_M$ are approximated by charge monopoles (see eq. 2.32), which simplifies eq. 2.100

$$E_{2nd} = \frac{1}{2} \sum_{MN} \Delta Q_M \Delta Q_N \Gamma_{MN} \quad (2.101)$$

where the excess charge on fragment M can be obtained as

$$\Delta Q_M = |a_M|^2 \quad (2.102)$$

because the FO basis is orthogonalized.

However, in eq. 2.101 the function Γ_{MN} takes only the form of one of two extreme cases of eq. 2.34 and 2.35

$$\Gamma_{MN} = \begin{cases} \frac{1}{R_{MN}} & \text{for } M \neq N \\ U_M & \text{for } M = N \end{cases} \quad (2.103)$$

Here, Γ_{MM} is the Hubbard parameter or chemical hardness of site M , which describes the onsite electron-electron repulsion analogously to the atomic Hubbard, and Γ_{MN} describes the Coulomb interaction of the delocalized excess charge on fragments M and N . This is only a simplified notation, whereas the fragment charges ΔQ_m are usually projected on atomic contributions Δq_α in actual calculation, which allows a more accurate computation of the interaction energy. Note that DFT calculations of radical systems are prone to SI, and that the major part of this error arises from the unpaired electron. Therefore, a correction to the second-order term is applied in order to mitigate the effects of SI. Following the proposed scaling of the contribution of to the unpaired electron to the Hartree and exchange-correlation energy,¹¹² a common scaling factor of $C = 1/5$ is applied to the second-order term E_{2nd} .¹⁰⁹

With this expression for the second-order energy, we can write the total energy of the charged system as

$$E^+[\rho] \approx E^0[\rho_0] - \sum_{MN} a_M^* a_N H_{MN}^0 + C \left(\frac{1}{2} \sum_{MN} \Delta Q_M \Delta Q_N \Gamma_{MN} \right) \quad (2.104)$$

The derivative of the total energy with respect to the FO coefficients yields a charge dependent Hamiltonian

$$H_{MN} = H_{MN}^0 + \delta_{MN} C \sum_K \Gamma_{MK} \Delta Q_K \quad (2.105)$$

where the Kronecker delta δ_{MN} appears due to the orthogonality of the FO basis functions ϕ_m .

In order to achieve a coupled propagation of the electrons and the nuclei, the hole wavefunction is propagated with the time dependent Schrödinger equation

$$i\hbar\dot{\Psi} = \hat{H}\Psi \quad (2.106)$$

which can be written after expansion of the wavefunction according to eq. 2.97 and

multiplication from left with $\langle \phi_M |$

$$\dot{a}_M = i \sum_N H_{MN} a_N \quad (2.107)$$

Note that electrostatic interactions between the QM and MM region are accounted for by calculating the fragment orbitals ϕ_M in the presence of the point charges of the environment, and also the matrix elements H_{MN}^0 are calculated with additional QM/MM coupling terms (see eq. 2.41).

The propagated excess charge is projected subsequently onto the QM atoms α , and the forces arising from the altered force field energy E_{MM}^{tot} are obtained as

$$m_K \ddot{R}_k = - \frac{\partial E_{MM}^{tot}(q_A^0, \Delta q_\alpha)}{\partial R_k} \quad (2.108)$$

This way, the change of Coulomb interactions with the environment due to the excess charge is captured well. The molecular relaxation of a fragment due to the presence of the charge, however, is still missing to a large extent. The reason for that is the way how empirical force fields calculate the total energy, e.g. non-bonded interactions are not computed between atom pairs that are within the distance of up to three covalent bonds. In order to model this molecular relaxation, an effective correction to the Hamiltonian was applied where the site energies H_{MM} relax depending on the occupation ΔQ_M by a precalculated value λ_i . The complete form of the Hamiltonian that is applied in eq. 2.107 is therefore

$$H_{MN} = H_{MN}^0 + \delta_{MN} \left(-\lambda_i^M \Delta Q_M + C \sum_K \Gamma_{MK} \Delta Q_K \right) \quad (2.109)$$

2.4. Measurement of Charge Carrier Mobility

As already mentioned in chapter 1, the charge carrier mobility is a figure of merit for the performance of organic semiconductors (OSCs) in practical applications. Obtaining this quantity from experiment or simulation is therefore of considerable interest. For the comparison of simulations and experiment it is essential to know the details of how the charge carrier mobility μ is derived in the respective method. Here we will briefly discuss the methods that serve as experimental reference in chapter 6 and 7. For an extensive overview of techniques see e.g. ref. 113.

2.4.1. Time of Flight

For the time of flight (TOF) method, the semiconductor has to be prepared as shown in figure 2.4. The sample is irradiated with a short laser pulse through the transparent indium tin oxide (ITO) electrode, which creates a sheet of charge carriers in the organic layer near the contact. Under the influence of an applied electric field E , these charge carriers drift toward the counter electrode (Ag), resulting in a transient current through the sample. After the carriers have reached the counter electrode, the current drops to zero. The duration from irradiation until the current drops corresponds to the transit time of the carriers (t_{tr}). Depending on the polarity of the applied bias V , electrons or holes will travel through the sample thickness d . The mobility can be obtained from following equation:

$$\mu = \frac{v}{E} = \frac{d}{t_{tr} \cdot E} = \frac{d^2}{t_{tr} \cdot V} \quad (2.110)$$

A minimal sample thickness is required to prevent short circuits and typical d exceeds 100 nm. Since the complete sample thickness has to be traversed by the charge carrier, structural defects like grain boundaries can deteriorate the measured mobility significantly.

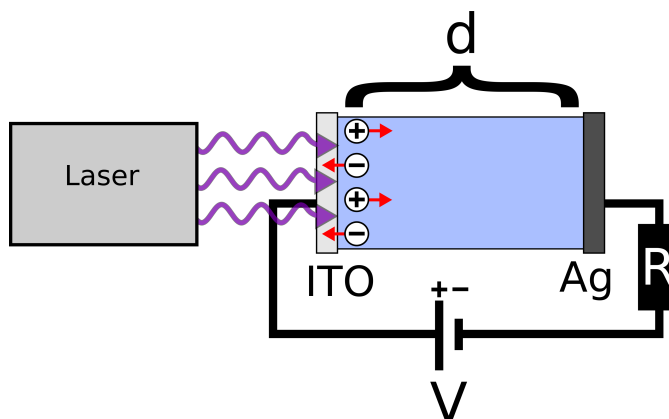


Figure 2.4.: Setup for a time of flight measurement. The organic semiconductor sample is sandwiched between two electrodes and irradiated with a laser pulse, which creates free charge carriers that get accelerated by the applied bias V .

2.4.2. Pulse-Radiolysis Time-Resolved Microwave Conductivity

In pulse-radiolysis time-resolved microwave conductivity (PR-TRMC) measurements a short pulse of high energy electrons is used to ionize the organic semiconductor, kick-

ing off secondary electrons and leaving behind cations (see figure 2.5). Many of these ionizations events will result in charge pairs that are not able to escape each other's Coulomb potential and will recombine rapidly. Some pairs, however, will be created at a sufficiently large distance and survive long enough to be detected. The produced charge carriers change the electrical conductivity ($\Delta\sigma$) of the sample which can be measured via the change in the microwave power that is reflected by the sample. It can be expressed as

$$\Delta\sigma = eN_{e-h} \sum \mu \quad (2.111)$$

where e is the elementary charge, $\sum \mu$ is the sum of electron and hole mobilities, and N_{e-h} is the density of generated electron-hole pairs. Latter can be estimated from the total absorbed microwave energy and the energy required to create one electron-hole pair, multiplied by a survival factor that accounts for pair recombinations during the duration of the pulse. In contrast to TOF measurements the excess charges are generated in the bulk and their transport properties are probed on a very narrow spatial scale. Nevertheless, charges trapped by structural defects or impurities will not respond to the microwave field and result in a decreased mobility.

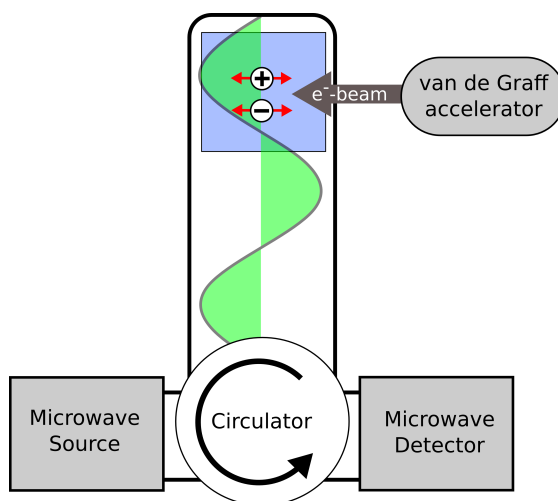


Figure 2.5.: Setup for a PR-TRMC measurement. Charge carriers are created in the organic semiconductor by an ionizing electron beam. Microwaves are routed by a circulator from a source to the sample, get reflected and are routed to the detector.

2.4.3. Thin Film Transistors

A thin film transistor (TFT) uses an electric field to control the size and shape of a conductive channel between source and drain contacts. Applying a voltage at the gate (see figure 2.6a) imposes an electric field, which attracts or repels charge carriers to or from a narrow channel (at most a few nm high) at the interface between OSC and insulator. The density of charge carriers n in turn influences the conductivity ($\sigma = ne\mu$) and thus the current I_{SD} between the source and drain.

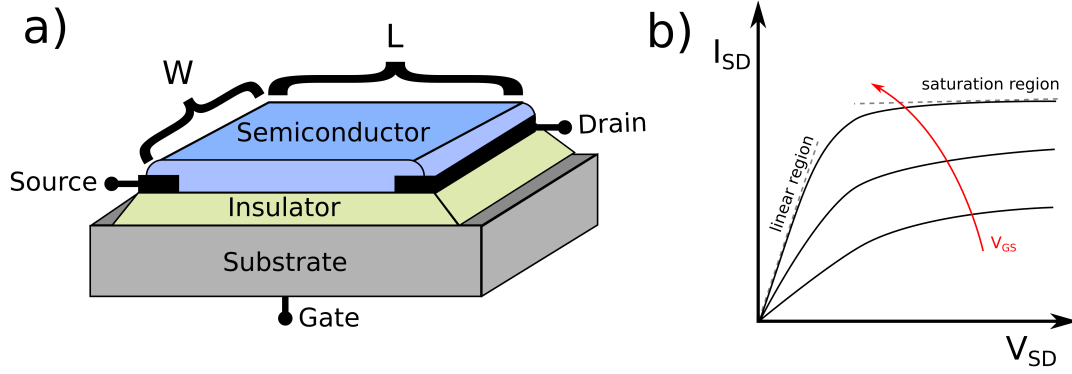


Figure 2.6.: Setup for a TFT measurement (a) and schematic output curves (b). Charge carriers are created at the interface between semiconductor and insulator by applying a gate voltage V_{GS} and allow a current between source and drain.

The charge carrier mobility μ can be determined from the output curves of the TFT, that is, the plot of the current between source and drain I_{SD} versus the applied bias V_{SD} for varying gate voltages V_{GS} . There exists a linear and a saturation region in the output curves (see figure 2.6b). The source-drain current in the linear region is defined as¹⁴

$$I_{SD} = \frac{W}{L} \mu C \left(V_{GS} - V_T - \frac{V_{SD}}{2} \right) V_{SD} \quad (2.112)$$

and in the saturation region as

$$I_{SD} = \frac{W}{2L} \mu C (V_{GS} - V_T)^2 \quad (2.113)$$

where W and L are the width and length of the conduction channel, C is the capacitance per unit area of the insulator and V_T is the threshold voltage. Therefore, the slope of I_{SD} vs. V_{GS} ($I_{SD}^{1/2}$ vs. V_{GS}) at constant V_{DS} can be used to calculate the mobility in the linear (saturation) region.

Since the conductive channel is formed at the interface between OSC and insulator, the mobility is affected by structural defects within the OSC resulting from the interface. Furthermore, the contact resistance at the source and drain electrodes has an pronounced impact on the mobility.¹¹⁴

Fragment Orbital Hamiltonian

Reproduced in part from ref. 115.

("Electronic couplings for molecular charge transfer: Benchmarking CDFT, FODFT, and FODFTB against high-level ab initio calculations.")

and also reproduced from ref. 116 with permission from the PCCP Owner Societies.

("Electronic couplings for molecular charge transfer: benchmarking CDFT, FODFT and FODFTB against high-level ab initio calculations. II.")

The efficient construction of an FO Hamiltonian is of considerable interest for the simulation of charge transport. As described in section 2.2.3 its elements can be used as approximative description of initial and final electronic states in the calculation of charge transfer rates within Marcus theory (section 2.3.2) or with Miller-Abrahams equations (section 2.3.1). The FO Hamiltonian is furthermore useful as a reasonable basis for Ehrenfest simulations as described in section 2.3.3 and allows also an efficient diagonalization of the electronic problem, which is needed e.g. for surface-hopping simulations like shown in ref. 110 and 117.

Whenever extensive conformational sampling or calculations on large molecular systems are needed, it may be required to use semi-empirical methods. In this work we focus on DFTB as approximation to DFT calculations. As already mentioned in section 2.1.2, the

orbitals that are employed in the DFTB method are optimized to improve the description of bonded systems. At intermediate distances (e.g. π -stacking), however, this procedure gives rise to severely underestimated interatomic interactions and thus CT integrals.¹¹⁸ Because it is difficult to achieve an adequate description of the interaction over a long range of interatomic distances within a minimal basis set, some computational tricks have to be introduced as shown in section 3.1 and 3.2.

3.1. Conventional DFTB FO Hamiltonian

In earlier studies¹¹⁸ a second parameter set was introduced to DFTB calculations. In the calculations of interatomic matrix elements the confinement was reduced for this parameter set, which is beneficial for the description of long-range interactions. Similar to FODFT calculations (see section 2.2.3), standard DFTB calculations are performed in a first step on the individual fragments in order to obtain the (non-orthogonalized) sets of FOs.

$$|\phi_m\rangle = \sum_{\mu} c_{\mu}^m |\eta_{\mu}\rangle \quad (3.1)$$

In a second step, however, the Hamilton matrix of the complex is constructed within a more diffuse AO basis, which is needed for the proper description of long-range interactions.¹¹⁸ This Hamiltonian is subsequently transformed into the FO basis.

$$\mathbf{H}'_{FO} = \mathbf{C}_{AO_c}^T \mathbf{H}_{AO_d} \mathbf{C}_{AO_c} \quad (3.2)$$

Here, \mathbf{C}_{AO_c} is a block-diagonal matrix of the coefficients c_{μ}^m of the fragment orbitals and the subscripts c and d denote that the confined or diffuse basis set was used in the construction of the respective matrix elements. The FO overlap matrix is constructed analogously and then used for a Löwdin orthogonalization of the FO basis.

$$\mathbf{H}_{FO} = \mathbf{S}_{FO}^{-1/2} \mathbf{H}'_{FO} \mathbf{S}_{FO}^{-1/2} \quad (3.3)$$

By applying different sets of DFTB parameters in the calculation of the matrix elements of \mathbf{C}_{AO_c} and \mathbf{H}_{AO_d} , the diagonal elements of \mathbf{H}'_{FO} are typically only a poor representation of the DFTB FO energies ϵ_i and the diagonal elements of \mathbf{S}_{FO} are not unity. Therefore, a further correction step is necessary, where the erroneous diagonal elements are replaced by the ϵ_i , obtained from the independent fragment calculations.

3.2. Improved Block DFTB Hamiltonian

In this work we introduce a more elegant method for the derivation of the FO Hamiltonian, which will directly result from a unitary transformation from the AO to FO basis without the necessity of further corrections. The problem with the optimized minimal basis of DFTB is the isotropic confinement; i.e. all p-orbitals have the same shape and differ only by their orientation along the x-, y- and z-axis. In an anisotropic system, like planar π -conjugated molecules, the AOs would experience compression from the atoms within the molecular plane of the fragment. Perpendicular to this plane, on the other hand, they would be quite free to delocalize. In such a case it would be desirable to have additional basis functions in order to model AOs that are compressed in one direction but diffuse in another direction. However, this would considerably increase the computational cost and an anisotropic confinement would add additional fitting parameters to the DFTB method. Therefore, we take another route and implement the idea of strong in-plane compression and weak out-of-plane compression by constructing the Hamilton matrix \mathbf{H}_{AO}^0 of the complex in a block matrix form

$$\mathbf{H}_{AO}^0 = \begin{pmatrix} \epsilon_1 & \alpha_{12} & \cdots & \beta_{1(N-1)} & \beta_{1N} \\ \alpha_{21} & \epsilon_2 & \cdots & \beta_{2(N-1)} & \beta_{2N} \\ \vdots & \vdots & \ddots & \vdots & \vdots \\ \beta_{(N-1)1} & \beta_{(N-1)2} & \cdots & \epsilon_{(N-1)} & \alpha_{(N-1)N} \\ \beta_{N1} & \beta_{N2} & \cdots & \alpha_{N(N-1)} & \epsilon_N \end{pmatrix} \quad (3.4)$$

where normal DFTB parameters $\alpha_{\mu\nu}$ are employed in the diagonal blocks (intramolecular interactions), parameters from a less confined set $\beta_{\mu\nu}$ are used in the off-diagonal blocks (intermolecular interactions), and N is the total number of AOs of the complex. The overlap matrix \mathbf{S}_{AO} is constructed analogously and the DFTB2 matrix elements can then be obtained as

$$H_{\mu\nu} = H_{\mu\nu}^0 + \frac{1}{2} S_{\mu\nu} \left(\sum_{\xi} \Delta q_{\xi} (\gamma_{\alpha\xi} + \gamma_{\beta\xi}) \right) \quad (3.5)$$

where $H_{\mu\nu}^0$ and $S_{\mu\nu}$ are matrix elements of the block matrix \mathbf{H}_{AO}^0 and \mathbf{S}_{AO} . Again, the FO coefficients c_{μ}^m of eq. 3.1 are obtained in conventional DFTB calculations of the independent molecules, applying the standard (confined) parameter set. However, by using the block matrix form of \mathbf{H}_{AO}^0 and \mathbf{S}_{AO} , the standard AO to FO transformation shown in eq. 3.2 and the subsequent Löwdin orthogonalization can be performed without

the necessity of additional corrections.

3.2.1. Inclusion of External Electric Fields

Previous studies with the conventional FO Hamiltonian already allowed QM/MM coupling with the environment. In these cases the FO matrix elements (especially the diagonal elements) are affected by the MM point charges Q_A . Measurements of the charge mobility often employ an additional uniform electric field (see e.g. TOF in section 2.4). Therefore, we include in this work also the possible interaction with a constant external field \vec{E} during the calculation of the FO matrix. The matrix elements shown in eq. 3.5 with additional QM/MM interaction and external field are

$$H_{\mu\nu} = H_{\mu\nu}^0 + \frac{1}{2}S_{\mu\nu} \left(\sum_{\xi} \Delta q_{\xi} (\gamma_{\alpha\xi} + \gamma_{\beta\xi}) + \sum_A Q_A \left(\frac{1}{r_{\alpha A}} + \frac{1}{r_{\beta A}} \right) + \left(\vec{E} \cdot r_{\alpha} + \vec{E} \cdot r_{\beta} \right) \right) \quad (3.6)$$

where $\vec{E} \cdot r_{\alpha}$ is the scalar product of the external field with the position vector of atom α .

3.3. Benchmarking

In the following we evaluate the performance of the FODFTB Hamiltonian, presented in section 3.2, for the calculation of electronic couplings in π -conjugated organic molecules. We benchmark the couplings H_{ab} for hole- and electron-transfer on 11 and 7 homo-dimers, respectively, as well as the corresponding exponential distance decay constant

$$|H_{ab}| = A \exp\left(-\frac{\beta d}{2}\right) \quad (3.7)$$

The benchmark set consists of small π -conjugated molecules with different number of hetero-atoms. We investigate how well less-approximative and therefore computational more demanding methods, like FODFT and CDFT, are able to reproduce the reference values and discuss their advantages and disadvantages compared to FODFTB. FODFTB calculations and FODFT calculations with the ADF program were performed by myself, whereas the remaining calculations of this benchmark were conducted by the coauthors of ref. 115 and 116. Some comparisons between the conventional and the new FODFTB method as well as the influence of the basis set confinement are given in the appendix.

3.3.1. Database

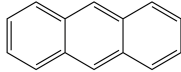
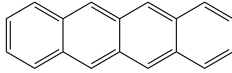
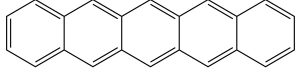
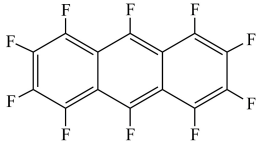
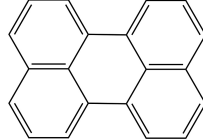
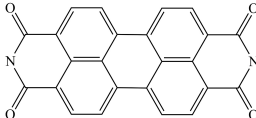
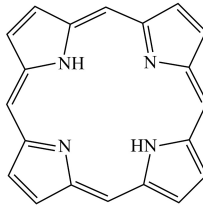
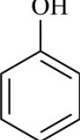
The database for hole transfer and electron transfer consists of 11 and 7 π -conjugated homo-dimers, respectively, with different sizes and various heteroatoms. See table 3.1 for an overview. The choice of molecules reflects our interest in organic semiconductors and charge carrying bio-molecules like DNA or aromatic protein side chains. However, the large computational cost of the applied high-level ab initio reference methods restricts the system size of the investigated dimers. For the hole transfer set very accurate calculations were performable for dimers with up to three conjugated double bonds. For the electron transfer set the molecules had to be larger than the ones in the hole transfer set, because all methods that actually include the excess charge need dimers that bind an excess electron. Small molecules, however, show a negative vertical electron affinity, i.e. show no stable anion. For example in the series of acenes, the two smallest molecules (benzene and naphthalene) show a negative vertical electron affinities (-1.30 eV and -0.17 eV, respectively) at the PBE/aug-cc-pVTZ level of theory. Anthracene is the smallest acene with a positive vertical electron affinity of 0.64 eV.

Depending on the size of the system, reference calculations were therefore possible at three different levels of theory:

- For the smallest molecules in the hole-transfer benchmark set, calculations with multi-reference configuration interaction singles and doubles with Davidson correction (MRCI+Q) were performable.^{119–121}
- For the larger molecules of this set we were able to apply N-electron valence state perturbation theory (NEVPT2)^{122–124}
- The benchmark set for electron transfer consists of even larger molecules (which are needed to form a stable anion) and therefore only spin-component scaled second-order approximate coupled cluster method (SCS-CC2) is applicable to these systems.¹²⁵

To provide rigorous reference values, and to further speed up the calculations, we consider initially only cofacial homo-dimers (with identical monomer geometries) as shown in figure 3.1 with the total charge of ± 1 . For these systems H_{ab} is uniquely defined as half of the first adiabatic excitation energy and does therefore not depend on the applied diabatization procedure. Extension to various different orientations is shown in section 3.3.6.

Table 3.1.: Database of organic molecules for the calculation of electronic coupling matrix elements for hole (left) and electron (right) transfer. For sake of simplicity only monomers are shown but the actual calculations were performed on cofacial π -stacks of cationic and anionic homo-dimers, respectively. Furthermore, the method at which the reference values could be obtained is shown (see section 3.3.2 for details).

Hole-Transfer Set			Electron-Transfer Set		
Name	Structure	Reference	Name	Structure	Reference
Ethylene	$\text{H}_2\text{C}=\text{CH}_2$	MRCI+Q			
Acetylene	$\text{HC}\equiv\text{CH}$	MRCI+Q	Anthracene		SCS-CC2
Cyclopropene		MRCI+Q	Tetracene		SCS-CC2
Cyclobutadiene		MRCI+Q	Pentacene		SCS-CC2
Cyclopentadiene		MRCI+Q	Perfluoroanthracene		SCS-CC2
Furane		MRCI+Q	Perylene		SCS-CC2
Pyrrrole		MRCI+Q	Perylene diimide		SCS-CC2
Thiophene		NEVPT2	Porphin		SCS-CC2
Imidazole		NEVPT2			
Benzene		NEVPT2			
Phenol		NEVPT2			

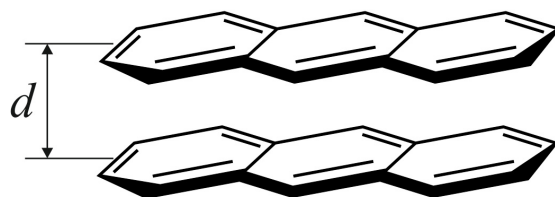


Figure 3.1.: Schematic representation of the alignment of a dimer. The neutral geometry was replicated along the axis perpendicular to the plane intercepting all heavy atoms. H_{ab} values were obtained for $d = 5.0, 4.5, 4.0, 3.5$ Å.

3.3.2. Computational Details

Geometry Optimizations

The monomers for the hole and electron charge transfer database were generated by the same protocol. The geometry of each monomer was optimized in the neutral charge state at the BP86/def2-TZVP level of theory with the resolution of identity approximation and an enlarged DFT integration grid (m4). The energy and gradient convergence criterion was set to 10^{-7} a.u. and 10^{-4} a.u., respectively. The energy minimum was confirmed by a subsequent vibrational analysis. The dimers were constructed by replicating the optimized molecule along the axis perpendicular to the molecular plane.

Reference calculations

In the reference calculations the electronic couplings were derived as half the energy splitting between ground and first excited state of the charged system (see section 2.2 for details). A state-average complete active space self-consistent field (CASSCF) wave function of the cationic system was chosen as a reference in MRCI+Q and NEVPT2 calculations. The active space consisted of all π and π^* orbitals with corresponding electrons and the averaging was usually performed over ground and first excited doublet states with equal weights. Because of the small energy differences between these states in thiophene and acetylene, the averaging was in these cases performed over the four lowest doublet states. The convergence criterion for the CASSCF energy was 10^{-7} a.u.. The aug-cc-pVTZ basis set was used for heavy atoms and the cc-pVDZ basis set for hydrogen atoms.

The computational cost of MRCI+Q grows rapidly with the number of reference functions that are extracted from the active space. Therefore only configurations with a CASSCF

weight of more than 10^{-4} were taken as references. Furthermore, the core electrons of carbon, nitrogen and oxygen atoms were treated as frozen.

In the NEVPT2 calculations, only configurations with a weight of more than 10^{-10} were taken as references. Because of software limitations, the frozen core approximation was not applied. The calculations for both multireference methods were carried out with the ORCA 2.9.1 program.

For the SCS-CC2 calculations the same basis set was applied as in the multireference calculations. The reference was an unrestricted Hartree-Fock determinant in the case of hole-transfer and a restricted open-shell wave function in the electron-transfer calculations. In both cases the energy and density convergence criterion was 10^{-7} a.u.. As scaling factors for same and opposite spin components of the elements of the Jacobi matrix the parameters of Grimme ($c_{os} = 6/5$ and $c_{ss} = 1/3$) were applied.¹²⁶ The resolution of identity (RI) approximation was used in all calculations,^{127,128} which were performed with the Turbomole suite of programs.^{129,130}

CDFT

The CDFT calculation were carried out with the CPMD program.¹³¹ The difference of Hirshfeld charges were used to constrain the charge to the donor or acceptor (see section 2.2.2 for details). Convergence was achieved when the charge difference between donor and acceptor was one elementary charge with a tolerance of 5×10^{-5} . The calculations were carried out in vacuo using the PBE functional.^{132,133} In order to evaluate the impact of exact exchange, the approximate GGA-exchange of PBE was replaced gradually with increasing percentages of exact Hartree-Fock exchange. In the following these hybrid-functionals will be denoted "CDFT/X", where X represents the percentage of GGA exchange replaced with Hartree-Fock exchange. The dimers were centred in a rectangular box with a minimum distance of 4 Å from the box edges. Only valance electrons were treated explicitly, whereas Troullier-Martins pseudopotentials were used for the description of core electrons.¹³⁴ The reciprocal space plane wave cutoff for KS-orbitals was set to 80 Ry in CDFT calculations with 100% GGA-exchange and was decreased by a factor of two in calculations where exact Hartree-Fock exchange was included.

FODFT

In the benchmarked FODFT calculations, $2N - 1$ and $2N + 1$ electrons were present in the case of hole and electron transfer, respectively, where N is the number of electrons of one monomer (see section 2.2.3). The calculations were performed with the CPMD program¹³¹ using the PBE functional and the same plane-wave cutoff, box dimensions and pseudo-potentials as in the CDFT calculations.

Further calculations with $2N$ electrons were performed in section 3.3.7 in order to evaluate the influence of the electron number on the coupling. These calculations were performed with the ADF software suite.¹³⁵ Again, the PBE functional was used, but this time with $2N$ electrons in the system and the TZ2P all-electron Slater-type basis set. Furthermore, it is to note that in ADF the electronic couplings are calculated between non-orthogonal fragment orbitals. To be consistent with the rest of our calculations, the Hamilton matrix in the basis of non-orthogonal HOMOs was transformed into an orthogonal basis according to the method of Löwdin.⁹⁴

FODFTB

In the FODFTB calculations, the block-matrix method described in section 3.2 was used at the DFTB2 level of theory. For the diagonal blocks, the halorg-0-1 parameters^{136–139} were used, whereas a weaker confinement was applied for the parameters of the off-diagonal blocks. For latter parameters, a confinement radius of 8 a.u. was applied for the wave function and ∞ for the density. The total energy of the monomer calculations was converged within 10^{-7} a.u.. Only (degenerate) HOMOs were considered on each molecule, which were orthogonalized according to the method of Löwdin.⁹⁴ In isolated acetylene molecules there are two sets of degenerate HOMOs. In order to be in accordance with the other calculations, we had to generate the HOMOs consisting of p-orbitals parallel and perpendicular to the stacking direction by the transformation shown in the appendix, and present here the coupling between the first ones.

3.3.3. Hole Transfer Couplings

In the following we will see how well FODFTB is able to reproduce the reference data in the hole transfer set compared to more elaborate methods like FODFT and CDFT. The numerical values for all 11 molecular dimers is presented in table 3.2. The quality of the results will be measured by the mean unsigned error (MUE), the mean relative signed error (MRSE), the mean relative unsigned error (MRUE) and the maximal error (MAX) evaluated over all molecules and distances.

The first thing to notice is that the reference values of the electronic couplings are very similar for a certain intermolecular separation distance, irrespective of the size or heteroatoms present in the molecule. Values of 450, 200, 100, and 50 meV are found for a distances of 3.5, 4.0, 4.5 and 5.0 Å, respectively.

Interestingly, the fragment orbital methods, FODFTB and FODFT, systematically underestimate the electronic coupling but are very similar, considering the approximate nature of DFTB. FODFTB yields only slightly worse electronic couplings than FODFT with a MRUE of 44.2% compared to 37.1%. Moreover, the decay constants are nearly identical for both FO methods, but the couplings drop too fast at higher distances, which results in an overestimation of the decay constant of 13%.

In a recent study the magnitude of the electronic coupling of fragment orbital approaches was related to the amount of non-local exchange used in the DFT method.¹⁴⁰ The authors observe a linearly increasing coupling with increasing amount of non-local exchange in the applied global hybrid-functionals. They attribute this behavior to the different distance dependences of (semi-)local and non-local exchange-correlation potentials. While former decays exponentially, latter decays with $1/r$ and yields therefore larger contributions at large distances. We also use a functional with semi-local exchange-correlation (PBE) in the FODFT calculations and PBE is also applied in the parametrization of the electronic parameters of DFTB. Therefore, we can attribute the underestimation of the couplings to the applied approximate exchange-correlation potential, which is also reflected in the overestimation of the decay constant compared to the reference calculations.

The errors of CDFT/0 are comparable to FODFT (MRUE = 38.7%), but of opposite sign, i.e. the coupling is overestimated. By admixing exact non-local exchange the artificial self-interaction error of (semi-)local DFT methods can be decreased. Various percentages were tested and the best results were found with 50% non-local exchange (CDFT/50),

which yielded an MRUE of 4.3%. Note that higher amounts of non-local exchange lead to an underestimation of the electronic coupling.¹¹⁵

Surprisingly, in CDFT calculations the inclusion of non-local (Hartree-Fock) exchange leads to a systematic *decrease* of electronic couplings, whereas in FO methods an *increase* with the amount of non-local exchange was observed.¹⁴⁰ Considering that one effect of the self-interaction error is the overestimation of delocalization of the excess charge (see section 2.1.3), it is maybe surprising that it has such a pronounced influence in CDFT calculations, where the charge is constrained to donor or acceptor and never free to delocalize. However, even though the charge is not free to delocalize over the dimer, it can still reside in more or less compact orbitals on one monomer, depending on the fraction of exact exchange. The electronic coupling, however, is approximately proportional to the overlap between the charge carrying orbitals in the two diabatic states, and will therefore be smaller for compact orbitals resulting from higher percentage of exact exchange.

Table 3.2.: Absolute values of the electronic coupling H_{ab} (in meV) between cationic dimers in the noted distance and its exponential decay constant β (in \AA^{-1}) as defined in eq. 3.7. Statistical evaluation of both quantities is given by means of mean unsigned error $MUE = (\sum_n |y_{calc} - y_{ref}|)/n$, mean relative signed error $MRSE = (\sum_n ((y_{calc} - y_{ref})/y_{ref}))/n$, mean relative unsigned error $MRUE = (\sum_n (|y_{calc} - y_{ref}|/y_{ref}))/n$ and maximum unsigned error $MAX = \max |y_{calc} - y_{ref}|$.

Dimer		CDFT/0	CDFT/50	FODFT	FODFTB	Reference
Ethylene						
H_{ab}	3.5 \AA	621.5	556.9	367.7	343.7	519.2
	4.0 \AA	314.8	278.5	169.9	171.5	270.8
	4.5 \AA	158.3	138.2	76.0	81.1	137.6
	5.0 \AA	78.4	68.0	32.6	35.6	68.5
	β	2.76	2.80	3.23	3.02	2.70
Acetylene						
H_{ab}	3.5 \AA	563.7	459.1	316.9	300.3	460.7
	4.0 \AA	273.2	218.2	139.9	151.8	231.8
	4.5 \AA	131.2	103.4	59.7	73.0	114.8
	5.0 \AA	62.4	48.7	24.3	32.5	56.6
	β	2.94	2.99	3.43	2.90	2.80

Cyclopropene						
	3.5 Å	816.1	585.7	418.8	367.4	536.6
H_{ab}	4.0 Å	369.6	259.5	179.2	168.5	254.0
	4.5 Å	164.8	116.1	75.9	75.2	118.4
	5.0 Å	73.9	52.2	31.7	32.3	54.0
	β	3.20	3.22	3.44	3.24	3.06
Cyclobutadiene						
	3.5 Å	646.3	395.9	323.3	261.6	462.7
H_{ab}	4.0 Å	326.8	195.1	148.9	117.3	239.1
	4.5 Å	164.5	95.8	67.9	50.5	121.7
	5.0 Å	87.9	43.7	30.5	20.5	62.2
	β	2.67	2.93	3.15	3.39	2.68
Cyclopentadiene						
	3.5 Å	702.1	490.5	343.3	283.2	465.8
H_{ab}	4.0 Å	346.4	234.5	157.7	130.5	234.4
	4.5 Å	167.4	113.3	71.8	57.7	114.3
	5.0 Å	80.9	54.9	32.3	24.0	53.4
	β	2.89	2.92	3.15	3.29	2.89
Furane						
	3.5 Å	598.2	452.4	315.6	280.3	440.3
H_{ab}	4.0 Å	292.5	213.7	141.6	128.2	214.9
	4.5 Å	141.0	101.5	62.8	56.2	101.8
	5.0 Å	67.0	48.2	27.5	23.2	46.0
	β	2.92	2.99	3.25	3.32	3.01
Pyrrole						
	3.5 Å	629.8	469.8	328.7	286.2	456.3
H_{ab}	4.0 Å	314.8	225.7	150.0	131.1	228.6
	4.5 Å	155.5	109.4	67.8	57.5	111.3
	5.0 Å	75.7	53.2	30.3	23.8	52.2
	β	2.82	2.90	3.18	3.32	2.89

Thiophene						
H_{ab}	3.5 Å	669.9	476.9	341.2	264.8	449.0
	4.0 Å	332.3	225.1	154.1	133.5	218.9
	4.5 Å	162.4	107.1	68.8	66.1	106.5
	5.0 Å	77.4	50.9	30.4	31.2	54.4
	β	2.88	2.98	3.22	2.85	2.82
Imidazole						
H_{ab}	3.5 Å	590.1	443.4	310.7	277.5	411.6
	4.0 Å	286.3	209.3	139.4	127.6	202.8
	4.5 Å	136.8	99.5	61.9	56.2	99.1
	5.0 Å	64.3	47.3	27.1	23.4	49.7
	β	2.95	2.98	3.25	3.29	2.82
Benzene						
H_{ab}	3.5 Å	647.8	475.5	342.4	299.9	435.2
	4.0 Å	321.7	223.5	154.8	142.2	214.3
	4.5 Å	155.6	105.6	69.2	64.5	104.0
	5.0 Å	73.8	49.8	30.6	27.4	51.7
	β	2.90	3.01	3.22	3.19	2.85
Phenol						
H_{ab}	3.5 Å	557.3	397.8	190.5	231.4	375.0
	4.0 Å	271.3	182.8	81.1	105.4	179.6
	4.5 Å	129.4	84.9	34.7	46.5	85.2
	5.0 Å	58.9	39.3	22.4	19.4	41.3
	β	3.00	3.09	2.91	3.31	2.95
MUE	H_{ab} [meV]	83.0	11.8	69.4	82.4	–
	β [1/Å]	0.07	0.13	0.37	0.33	–
MRSE	H_{ab} [%]	38.7	-0.8	-37.3	-42.9	–
	β [%]	-1.5	4.4	12.8	11.7	–
MRUE	H_{ab} [%]	38.7	5.3	37.6	42.4	–
	β [%]	2.3	4.3	13.0	12.5	–
MAX	H_{ab} [meV]	279.5	66.8	184.5	201.1	–
	β [1/Å]	0.14	0.25	0.63	0.71	–

3.3.4. Electron Transfer Couplings

Now we will evaluate how well FODFTB reproduces the reference data in the electron transfer set, compared to FODFT and CDFT. The electronic couplings and its decay constant are collected in table 3.3 and the same error estimates are applied as in section 3.3.3. In contrast to the hole-benchmark, the reference values were obtained with the SCS-CC2 method.

Again, the FO methods underestimate the electronic coupling for electron-transfer, like before in the case of hole-transfer, which we already attributed to the missing non-local exchange. However, in contrast to the cationic systems, where FODFT and FODFTB yielded very similar results, we find here more pronounced differences between both approaches. FODFT calculations perform even better than in the cationic systems (MRUE = 27.9%), whereas FODFTB shows larger deviations from the reference with a MRUE of 53.5%.

Also the value of the decay constant β is now no longer the same but much more overestimated with FODFTB (MRSE = 25.8%) compared to the very good value of FODFT (MRSE = 5.0%). One could ask, what causes the much weaker similarity of FODFTB and FODFT in the anionic systems compared to the cationic ones. There are two main differences between the FODFT and FODFTB calculations. One is obviously the approximate nature of DFTB. Another difference is the number of electrons that are present in the calculations. In FODFTB we obtain the FOs from the neutral monomers (LUMOs) and the Kohn-Sham Hamiltonian that is used to evaluate the coupling between these FOs has $2N$ electrons, whereas in the benchmarked variant of FODFT the FOs are obtained from anionic monomers (SOMOs) and the Hamiltonian in the coupling calculation has $2N+1$ electrons. The LUMOs that are used in the case of DFTB have arguably the same meaning as the SOMOs in the DFT calculations. However, in section 3.3.7 we will see that the poorer performance of FODFTB in the electron-transfer set can not be attributed to the difference between SOMOs and LUMOs. Therefore the weak coupling in FODFTB and its strong decay can be attributed to the employed minimal basis set. The basis employed for the parametrization of intermolecular interactions is nearly unconfined, but it is still derived from the atomic orbitals of a neutral atom. Even diffuser orbitals would be necessary to describe the electronic couplings in a negatively charged system, however.

CDFT/0 shows also a larger error than in the cationic systems and overestimates the couplings now by 60.8% (MRUE) and is therefore worse than the FODFTB results.

Note that again the sign of the deviation differ between CDFT and FO calculations. As before, we find an overestimation of the electronic coupling in CDFT, whereas FO methods underestimate the electronic coupling. Nevertheless, the decay constant agrees still very well with the reference (MRUE = 7%) Inclusion of exact exchange can mitigate the overestimation of the electronic couplings in CDFT and again a value of 50% exact exchange was found to yield the best results (MRUE = 8.2%).

Table 3.3.: Absolute values of the electronic coupling H_{ab} (in meV) between anionic dimers in the noted distance and its exponential decay constant β (in \AA^{-1}) as defined in eq. 3.7. Statistical evaluation of both quantities is given by means of mean unsigned error $MUE = (\sum_n |y_{calc} - y_{ref}|)/n$, mean relative signed error $MRSE = (\sum_n ((y_{calc} - y_{ref})/y_{ref}))/n$, mean relative unsigned error $MRUE = (\sum_n (|y_{calc} - y_{ref}|/y_{ref}))/n$ and maximum unsigned error $MAX = \max |y_{calc} - y_{ref}|$.

Dimer		CDFT/0	CDFT/50	FODFT	FODFTB	Reference
Anthracene						
H_{ab}	3.5 \AA	637.0	479.2	316.9	237.8	421.1
	4.0 \AA	324.5	227.8	147.3	98.8	212.3
	4.5 \AA	169.4	113.1	68.0	39.4	106.1
	5.0 \AA	87.9	58.0	30.7	14.8	52.3
	β	2.64	2.81	3.11	3.70	2.78
Tetracene						
H_{ab}	3.5 \AA	628.8	466.0	322.9	242.9	417.2
	4.0 \AA	313.1	213.8	149.2	101.6	204.3
	4.5 \AA	160.8	102.4	69.2	40.8	97.9
	5.0 \AA	81.5	50.4	32.5	15.5	45.4
	β	2.72	2.97	3.07	3.67	2.96
Pentacene						
H_{ab}	3.5 \AA	618.3	451.3	323.2	243.9	411.0
	4.0 \AA	303.0	202.4	148.5	102.7	198.0
	4.5 \AA	154.0	95.1	68.5	41.4	92.4
	5.0 \AA	77.7	45.7	32.0	15.8	41.0
	β	2.76	3.05	3.08	3.65	3.07

Perfluoroanthracene						
H_{ab}	3.5 Å	479.6	349.7	236.1	198.4	310.9
	4.0 Å	227.2	152.7	101.0	80.9	139.1
	4.5 Å	107.9	68.5	44.0	31.9	59.9
	5.0 Å	49.6	30.6	18.7	12.4	24.0
	β	3.02	3.24	3.38	3.70	3.41
Perylene						
H_{ab}	3.5 Å	633.7	460.7	324.6	236.3	423.7
	4.0 Å	324.5	222.7	156.4	98.5	220.7
	4.5 Å	174.0	114.1	77.0	39.3	116.6
	5.0 Å	94.4	61.1	39.0	15.0	62.8
	β	2.54	2.70	2.83	3.68	2.55
Perylene diimide						
H_{ab}	3.5 Å	541.8	417.7	285.1	227.0	373.8
	4.0 Å	261.0	187.4	130.5	94.1	179.2
	4.5 Å	131.2	89.2	60.9	37.5	84.1
	5.0 Å	65.1	44.0	29.1	14.4	38.0
	β	2.82	3.00	3.05	3.69	3.05
Porphin						
H_{ab}	3.5 Å	577.7	408.5	288.5	216.0	374.5
	4.0 Å	285.0	184.8	131.1	88.7	182.9
	4.5 Å	146.6	87.7	60.2	35.1	89.4
	5.0 Å	74.7	42.7	28.1	13.2	44.1
	β	2.72	3.01	3.10	3.72	2.85
MUE	H_{ab} [meV]	96.7	15.0	46.5	85.3	–
	β [1/Å]	0.21	0.08	0.15	0.74	–
MRSE	H_{ab} [%]	60.8	7.5	-27.9	-53.5	–
	β [%]	-6.8	0.8	5.0	25.8	–
MRUE	H_{ab} [%]	60.8	8.2	27.9	53.5	–
	β [%]	6.8	2.9	5.3	25.8	–
MAX	H_{ab} [meV]	215.9	58.1	104.2	187.4	–
	β [1/Å]	0.39	0.17	0.33	1.13	–

3.3.5. Compensation for Missing Non-Local Exchange

We find a very systematic deviation from the reference couplings for all methods in the cationic as well as anionic benchmark sets. This is shown in figure 3.2 (top) for the cationic systems. The correlation between the benchmarked methods and the reference is nearly linear with R^2 values of 0.9869, 0.9904, 0.9788 and 0.9853 for CDFT/0, CDFT/50, FODFT and FODFTB, respectively. A similar correlation is found for the anionic systems, which is shown in figure 3.2 (bottom). In this case the R^2 values are 0.9990, 0.9988, 0.9985 and 0.9879 for CDFT/0, CDFT/50, FODFT and FODFTB, respectively.

Hence, this suggests that a constant scaling factor for each method could improve the final results tremendously. The scaling factors were derived as the inverse of the slope of a linear fit to the data shown in figure 3.2. The final values are presented in table 3.4 and the scaled methods will be labeled with an "s"-prefix. The scaling factors for hole and electron transfer are comparable. The best method in the benchmark (CDFT/50) can practically be used without any scaling. For all other methods a significant improvement of the electronic couplings can be achieved. An interesting feature is the nearly identical scaling factor for FODFT of 1.3 for hole and electron transfer that yields couplings very close to the reference values with quite low computational cost. The scaling factors of FODFTB are quite large with 1.540 and 1.795 for hole and electron transfer, respectively. Nevertheless, after scaling the couplings for the cationic systems are even better than with sFODFT and even in anionic systems it is still possible to significantly reduce the problems of DFTB that originate from the too confined minimal basis.

3.3.6. Transferability of the Correction

In the benchmark set all dimers were in a perfect cofacial, π -stacked orientation. We found that FODFT and FODFTB systematically underestimate the electronic couplings, whereas CDFT/0 overestimates them. In the following we will further examine how well the methods perform for different orientations, where the monomers are no longer perfectly cofacial. The main question is if the same systematic error as in the cofacial orientation can be observed also for randomly orientated molecules. In this case the scaling procedure from section 3.3.5 can be a valuable tool to systematically improve the electronic couplings along an MD simulation in a black-box manner.

For the case of hole-transfer a thiophene dimer was chosen to evaluate different orientations as shown in figure 3.3: (a) One monomer is rotated about the axis through

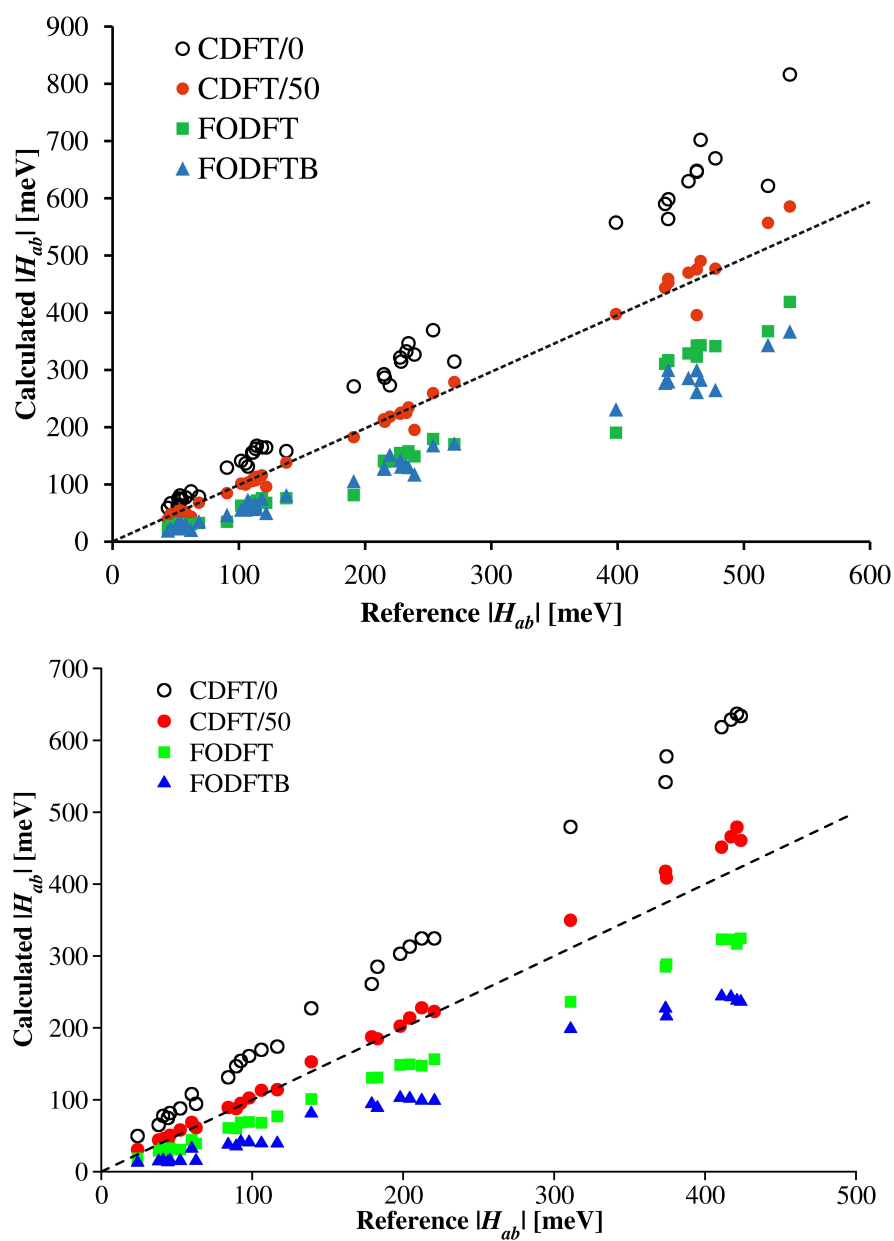


Figure 3.2.: Correlation between calculated CDFT/0, CDFT/50, FODFT, FODFTB $|H_{ab}|$ values and reference data in the cationic systems (top) and the anionic systems (bottom). The black dashed line represents perfect correlation.

Table 3.4.: Errors of H_{ab} after applying a method-specific scaling factor ("s" prefix) to each method. The original errors of the unscaled methods as derived in table 3.2 and 3.3 are given in parentheses for comparison.

	Scaling	MUE [meV]	MRSE [%]	MRUE [%]	MAX [meV]
CDFT/0	h^+ 0.721	10.6 (83.0)	-1.8 (38.7)	5.2 (38.7)	71.1 (279.5)
	e^- 0.660	5.9 (96.7)	6.1 (60.8)	7.3 (60.8)	16.2 (215.9)
CDFT/50	h^+ 0.962	11.7 (11.7)	-6.6 (-0.8)	7.1 (5.3)	81.7 (66.8)
	e^- 0.915	6.2 (15.0)	-1.7 (7.5)	4.9 (8.2)	17.3 (58.1)
FODFT	h^+ 1.348	24.7 (69.4)	-17.3 (-37.3)	17.6 (37.6)	142.1 (184.5)
	e^- 1.325	7.0 (46.5)	-4.4 (-27.9)	5.9 (27.9)	17.2 (104.2)
FODFTB	h^+ 1.540	20.0 (82.4)	-12.7 (-42.9)	13.9 (42.4)	69.7 (201.1)
	e^- 1.795	21.6 (85.3)	-15.9 (-53.5)	19.5 (53.5)	47.7 (187.4)

the center of masses of the molecules, (b) both monomers are simultaneously rotated in order to gradually break the π -stacking, (c) the monomers are put in random relative orientations at a constant centre of mass distance.

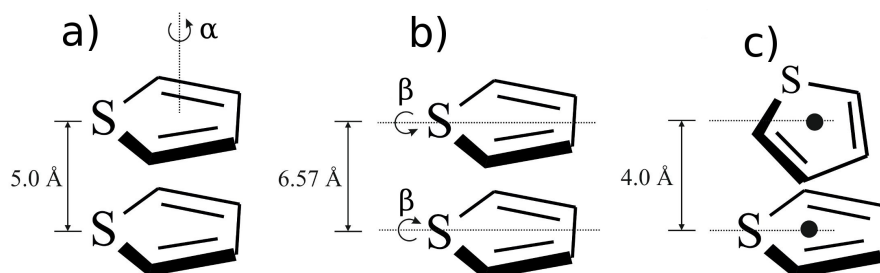


Figure 3.3.: Thiophenes in additional orientations: (a) the top monomer was rotated by angle α about the centre of mass with α ranging from 0° to 180° with a step size of 20° . (b) Simultaneous rotation of two monomers in opposing directions by angle β ranging from 0° to 90° with a step size of 10° . The intermolecular distance was set to 5, 6.57 and 4 Å in (a), (b) and (c), respectively.

As can be seen in figure 3.4 all methods show the same trend for the electronic couplings in case (a). Especially the minimum couplings of 0.0 eV coincide very well. This results from the similar nodal structure of the involved HOMOs, whose overlap is in first approximation proportional to the electronic coupling. Also in the out of plane rotation (case b) all methods show a similar trend. Almost all methods find a maximum at $\beta = 60^\circ$. Only

for CDFT/0 the maximum is shifted by 10° to $\beta = 70^\circ$. For the random orientations (case c) the reference values can no longer be derived from the adiabatic splitting due to the broken symmetry of the system. The GMH approach (see section 2.2.1) was therefore applied in these cases. As can be seen in table 3.5 FODFTB and FODFT show similar performance (especially after scaling) and the results for these random orientations are comparable to the values from the electron and hole benchmark sets. CDFT/0 performs with MRSE of 124.9% much worse than for the symmetric systems. This might be related to the tendency of the PBE functional to over-delocalize the charge, combined with the ambiguous choice of a constraining potential in CDFT. Inclusion of exact exchange mitigates the problem (MRSE=17.1%), but still the performance of CDFT/50 is not as superior as in the symmetric systems.

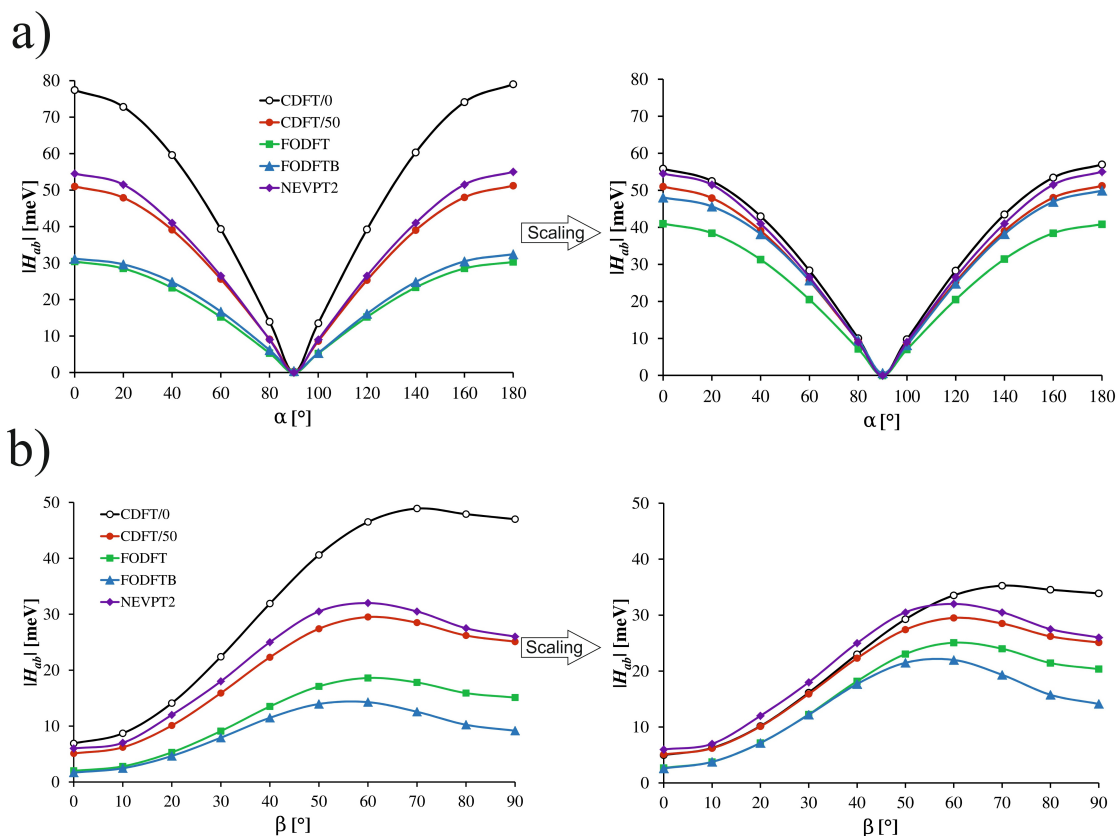


Figure 3.4.: Variation of electronic coupling along a rotation shown in figure 3.3 with angles α (a) and β (b). The right side shows the curves after application of the method-specific scaling factors (see table 3.4)

Also for the electron transfer case we investigated the performance for randomly rotated

Table 3.5.: Statistical evaluation of the error of H_{ab} calculated for 15 randomly rotated cationic thiophene dimers (see figure 3.3c). The reference data were obtained at the NEVPT2 level of theory using the GMH approach. The errors of the scaled methods ("s"-prefix) are shown together with errors of the unscaled methods in parentheses for comparison.

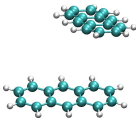
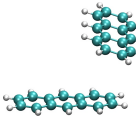
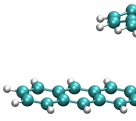
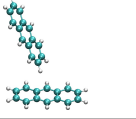
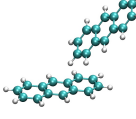
	MUE [meV]		MRSE [%]		MRUE [%]		MAX [meV]	
sCDFT/0	72.1	(160.3)	62.2	(124.9)	62.3	(124.9)	158.6	(256.0)
CDFT/50	–	(26.8)	–	(17.1)	–	(23.3)	–	(55.8)
sFODFT	25.6	(48.2)	1.4	(-24.8)	17.7	(26.6)	58.7	(94.4)
sFODFTB	26.8	(64.9)	-4.5	(-38.0)	17.1	(38.0)	69.2	(110.3)

structures. The large size of the molecules in the electron transfer set, however, restricted our calculations to 6 different orientations of the smallest member (anthracene), which are presented in table 3.6. As one could expect, the electronic couplings increase with decreasing interatomic distance between closest atoms. However, due to the nodal structure of the singly occupied orbitals, small distance is no sufficient criterion for high couplings. This can be seen on dimer 4, which shows nearly vanishing coupling for a relative close interatomic distance of 3.5 Å. Dimers 5 and 6 show larger couplings, because of a relatively short contact between fragments of about 2 Å. Nevertheless, these couplings are still smaller than in the cofacial orientations due to the reduced overlap. The small couplings of dimers 1 to 4 are prone to numerical noise of the calculations but the ordering of dimers from higher to lower electronic couplings is still relatively well reproduced with all methods. For the larger couplings of dimers 5 and 6 we can again find the same trends as in the cofacial sets with underestimation of the couplings by the FO methods and overestimation with CDFT/0. The inclusion of exact exchange (CDFT/50) can mitigate the CDFT errors only partially. A main problem of CDFT at such small distances may be, that the results are expected to exhibit a significant dependence on the choice of the weighting function, leading to increased uncertainties in H_{ab} , as discussed in refs. 93 and 92.

3.3.7. Influence of Electron Number in FO Calculations

In CDFT calculations we are obtaining an initial and final diabatic state for the charge transfer reaction in form of two constrained Slater determinants. In the FO methods, however, we are only approximating the initial and final diabatic state with a single

Table 3.6.: Electronic coupling matrix elements calculated for six randomly oriented anionic anthracene dimers (in meV). For each molecule the closest contact is given. Unscaled $|H_{ab}|$ values are given in brackets

Dimer	Closest contact [Å]	sCDFT/0	sCDFT/50	sFODFT	sFODFTB	Ref.
1 	5.46	0.9 (1.3)	0.7 (0.8)	1.3 (1.0)	0.1 (0.0)	0.0
2 	4.79	8.7 (13.2)	5.3 (5.8)	5.7 (4.3)	3.3 (1.8)	2.6
3 	4.59	6.0 (9.1)	4.6 (5.0)	5.6 (4.2)	2.0 (1.1)	1.7
4 	3.52	0.9 (1.4)	2.7 (2.9)	2.8 (2.1)	0.3 (0.1)	2.3
5 	2.24	174.4 (264.2)	73.6 (80.4)	31.3 (23.6)	27.3 (15.2)	46.4
6 	2.14	287.7 (435.9)	200.6 (219.2)	70.6 (53.3)	52.3 (29.1)	91.5

orbital (HOMO/LUMO in case of hole and electron transfer, respectively). Up to now, we constructed the dimer Hamiltonian in our FODFT calculations with $(2N\pm 1)$ electrons, i.e. the actual number of electrons in the system. In contrast to this, FODFTB as well as several other different FODFT implementations perform both the monomer and dimer calculations for neutral systems, i.e. introduce an additional approximation. We tested the influence of the number of electrons on the resulting electronic coupling for all molecules of both benchmark sets at a separation distance of 3.5 Å and present the results in table 3.7. FODFT($2N\pm 1$) denotes the CPMD implementation with correct number of electrons that was also used up to now, whereas FODF($2N$) denotes results for ADF calculations where the systems are neutral (see section 3.3.2 for details). Interestingly, FODFT calculations with $(2N)$ electrons yield smaller MRUE than with $(2N\pm 1)$ electron for both sets, even though the charged system is approximated with the neutral one. Note that the influence of other factors besides the electron number, like application of different basis sets in ADF and CPMD, was found to be negligible in ref 115. This is especially surprising for the electron transfer set, because in FODFT($2N$) calculations the coupling is evaluated between LUMOs, which have no real physical meaning whereas in FODFT($2N\pm 1$) the coupling is evaluated between SOMOs, which should in principle be a better representation of the charge residing on one molecule. While both DFT methods perform better in the electron benchmark set, FODFTB($2N$) shows the opposite trend. The reason can be found in the minimal basis set. Even though special parameters resulting from uncompressed atomic orbitals are used, these orbitals are nevertheless resulting from a neutral reference atom. For the description of the electronic coupling in anionic systems, however, more diffuse orbitals are required. If we compare FODFTB($2N$) with FODFT($2N$) instead of FODFT($2N\pm 1$) the error introduced by the minimal basis of DFTB and its approximate nature seems to be slightly more pronounced. After scaling, however, the differences between FODFTB($2N$) and FODFT($2N$) will again decrease since FODFT($2N$) will just need a smaller scaling factor to optimize the electronic couplings.

3.4. Discussion and Conclusion

For DFT calculations at the GGA level (and also of DFTB, which is parametrized using a GGA functional) we found that FO methods perform as well as CDFT calculations, even though they approximate the electronic coupling between diabatic states with a coupling between fragment orbitals. We furthermore found that the errors are systematic,

Table 3.7.: Comparison of electronic coupling matrix elements calculated with and without explicit charge in the system for the hole transfer set (top) and electron transfer set (bottom). Expressions in parentheses denotes number of electrons used in the dimer Hamiltonian. The MUE is evaluated over both sets. Reference values are reported in the last column at the same level of theory as in table 3.2 and 3.3. All couplings are in meV.

	FODFT(2N±1)	FODFT(2N)	FODFTB(2N)	Ref(2N±1)
Ethylene	367.7	388.4	343.7	519.2
Acetylene	316.9	345.3	300.3	460.7
Cyclopropene	418.8	439.4	367.4	536.6
Cyclobutadiene	323.3	345.6	261.6	462.7
Cyclopentadiene	343.3	358.7	283.2	465.8
Furane	315.6	333.7	280.3	440.3
Pyrrole	328.7	347.7	286.2	456.3
Thiophene	341.2	356.1	264.8	449.0
Imidazole	310.7	328.2	277.5	411.6
Benzene	342.4	354.1	299.9	435.2
Phenol	190.5	279.5	231.4	375.0
MRUE [%]	28.6	22.7	36.3	–
Anthracene	316.9	342.1	237.9	421.1
Tetracene	322.9	339.2	242.8	417.2
Pentacene	323.2	335.4	243.9	411.0
Perfluoroanthracene	236.1	237.8	198.4	310.9
Perylene	324.6	344.9	236.4	423.7
Perylene diimide	285.2	292.5	227.0	373.8
Porphin	288.5	300.7	215.9	374.5
MRUE [%]	23.3	19.9	41.1	–

of similar magnitude, but with different sign. Both FODFTB and FODFT calculations underestimate the electronic coupling for electron and hole transfer, whereas CDFT/0 overestimates it. We found that inclusion of non-local exchange in CDFT calculations can significantly reduce the electronic couplings and good results are obtained by replacing 50% of GGA exchange with non-local exchange. The opposite trend was reported for FODFT calculations, where inclusion of non-local exchange lead to an increases H_{ab} .¹⁴⁰ The dependence of the electronic coupling in FODFT calculations was attributed to the exponentially decaying exchange-correlation potential in semi-local functionals (like PBE), whereas the correct potential had to decay with $1/r$ in order to cancel the SI. As a result, these functionals yield too small contributions to the coupling at intermolecular distances. By varying the amount of exact HF exchange from 0% to 100% the electronic coupling increases by roughly a factor of two.¹⁴⁰ The same underestimation can be expected using DFTB, since electronic coupling integrals are obtained with the PBE functional during its parametrization.

As computationally inexpensive alternative to the inclusion of non-local exchange, a simple scaling of the electronic couplings with a constant method-specific factor was tested. This also enables an easy correction for DFTB, which otherwise could include non-local exchange only implicitly via a complete re-parametrization, using a non-local exchange correlation functional instead of PBE. We found that by scaling the electronic coupling, relative errors can be reduced by at least a factor of 2.

We found that the performance of FODFT is similarly good for both cations and anions. When results are scaled by a factor of 1.3, FODFT with PBE is almost as accurate as the significantly more demanding CDFT/50 method. For FODFTB, larger errors were found in electron benchmark set compared to the hole benchmark set. This was attributed to the applied minimal basis set, which is obtained from neutral atomistic calculations and is therefore probably not sufficiently diffuse for an adequate description of the LUMO orbitals. However the deviations are systematic and a larger scaling factor can mitigate the error. After scaling, a similar MRUE for the positively and negatively charged systems is found, with 14% and 20%, respectively. The number of electrons in FO calculations has only little impact on the results, and for the studied cases the errors were even smaller for calculations on the neutral system.

The transferability of this scaling factor was tested on rotated and randomly orientated dimers for hole and electron transfer. A systematic improvement of the results in any cases could be observed, which suggest that our findings can be likely generalized to

larger π -conjugated systems of relevant organic semiconductors. We furthermore observed that FO calculations perform equally well for the randomly oriented dimers as for the symmetric benchmark set, whereas CDFT calculations showed a deterioration of the performance. The robustness of the FO methods for arbitrary geometries is a necessary feature for a method that will be applied along MD simulations.

For practical applications one has to balance the accuracy that is achievable within the method with the computational efficiency, which allows for more thorough sampling and investigation of larger systems. Our FODFTB implementation is about six orders of magnitude faster than FODFT as implemented in CPMD (see figure 3.5 for comparison) with a sufficiently small error especially if scaling is applied. To put the accuracy of FODFTB into perspective, we note that a MRUE of 20% leads to an uncertainty of a factor of 1.4 in the non-adiabatic charge transfer rate ($k \sim |H_{ab}|^2$, see figure 3.5 bottom). This is similar or even smaller than the uncertainties in the rate resulting from the DFT calculation of the other quantities that enter the rate expression such as reorganization energy^{44,141} and driving force.¹⁴² In conclusion, scaled versions of FODFT or FODFTB are the best choice for large molecules, to obtain fast estimates, and for series of calculations on different structures.

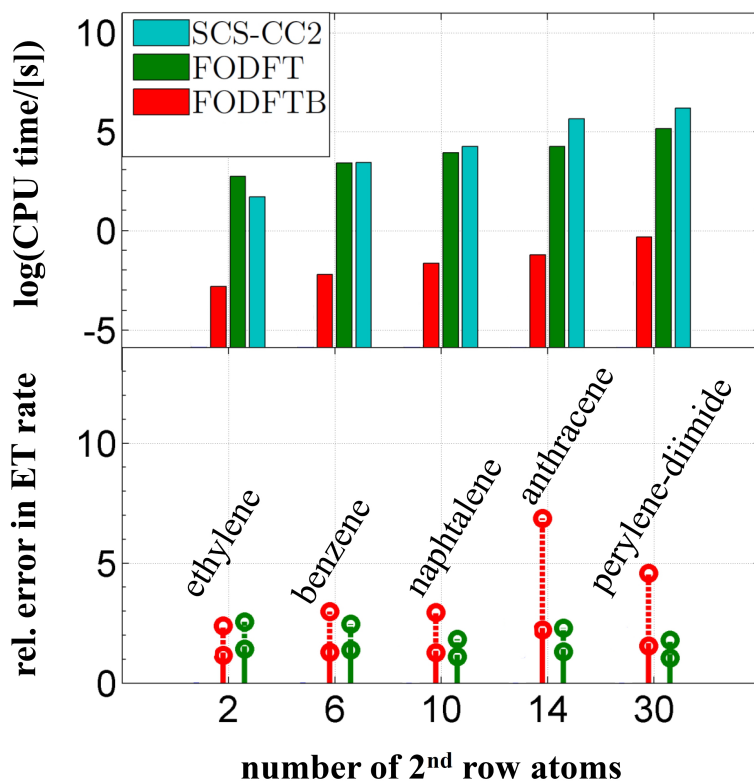


Figure 3.5.: Total CPU time for H_{ab} calculations with respect to the system size for selected methods (top panel) and corresponding relative errors in the ET rate due to the error in H_{ab} (bottom panel). The latter is shown for the unscaled (dotted line) and scaled (solid line) variant of the FODFTB and FODFT method calculated as $\max\left[\frac{H_{ab}^{SCS-CC2}}{H_{ab}}; \frac{H_{ab}}{H_{ab}^{SCS-CC2}}\right]$, where $H_{ab}^{SCS-CC2}$ is the SCS-CC2 reference value. Results for ethylene, benzene and naphthalene are for hole transfer, while the results for anthracene and perylene diimide are for electron transfer.

Bridge-mediated Couplings

In the last chapter we have seen how we can calculate the direct (through vacuo) coupling between donor and acceptor. In systems where donor (D) and acceptor (A) are separated by a bridge (B), however, super-exchange over the bridge becomes the dominant contribution to their total electronic coupling T_{DA} . The calculation of bridge-mediated couplings becomes important e.g. for CT in bimolecular organic crystals¹⁴³ or charge recombination in dye sensitized solar cells.¹⁴⁴

T_{DA} can be calculated exactly for small systems by fixing the nuclear coordinates at the configuration where the non-adiabatic D and A energy surfaces cross, diagonalizing the Hamiltonian of the total system, and extracting T_{DA} as half the energy splitting between the eigenstates with the most dominant D and A character.^{145–147} A more general approach to calculate T_{DA} , which is also applicable when donor and acceptor are not in resonance, is the partitioning according to Löwdin.^{148,149} The Schrödinger equation in an orthogonalized basis takes the form

$$\mathbf{HC} = E\mathbf{C} \quad (4.1)$$

In fragment orbital calculations, as shown in the last chapter, we apply an orthogonalized basis set consisting of the HOMOs of the donor, acceptor and all intermediate bridge molecules, respectively. By partitioning the basis into D/A (P) and bridge (Q) subspace, and reordering eq. 4.1, we can write

$$\begin{pmatrix} \mathbf{H}_{pp} - E\mathbf{1}_{pp} & \mathbf{H}_{pq} \\ \mathbf{H}_{qp} & \mathbf{H}_{qq} - E\mathbf{1}_{qq} \end{pmatrix} \begin{pmatrix} \mathbf{C}_p \\ \mathbf{C}_q \end{pmatrix} = 0 \quad (4.2)$$

Here, \mathbf{H}_{pq} is a submatrix of \mathbf{H} with elements H_{ij} , where i is a basis function in subspace P and j in subspace Q . After solving one linear equation for \mathbf{C}_q and substituting the

result into the other equation, one can contract the original secular equation 4.1 to an equivalent secular equation of only the D/A subspace.

$$\mathbf{H}_{pp}^{eff} \mathbf{C}_p = E \mathbf{C}_p \quad (4.3)$$

with the effective (contracted) 2×2 Hamiltonian

$$\mathbf{H}_{pp}^{eff} = \mathbf{H}_{pp} + \mathbf{H}_{pq}(E\mathbf{1}_{qq} - \mathbf{H}_{qq})^{-1}\mathbf{H}_{qp} \quad (4.4)$$

However, the effective Hamiltonian, entering equation 4.3 is itself dependent on the eigenvalue E and therefore a self-consistent calculation has to be applied. If the states in subspace P are energetically separated from and weakly coupled to the states in Q , then the energy E of the tunneling charge carrier will be close to the unperturbed D(A) energies. As a starting point E is set to the average of the D and A state energies, and then iteratively converged as the average of the resulting eigenvalues of \mathbf{H}_{pp}^{eff} , until self-consistency is reached within a defined tolerance. T_{DA} is finally obtained as the off-diagonal element of \mathbf{H}_{pp}^{eff} , which can be written as¹⁵⁰

$$T_{DA}(E) = H_{DA} + \sum_{ij}^{bridge} H_{Di} G_{ij}(E) H_{jA} \quad (4.5)$$

where H_{DA} is the direct electronic coupling matrix element between D and A , H_{Di} (H_{iA}) is the coupling of the donor (acceptor) to the bridge orbital i , and G_{ij} is an element of the Green's function matrix of the bridge $\mathbf{G} = (E\mathbf{1}_{bb} - \mathbf{H}_{bb})^{-1}$.

Here, we implement this method with the FODFTB framework shown in section 3.2, and test it against CDFT calculations, where the density of the D-B-A system is constrained to donor and acceptor. The FODFTB calculations were performed by myself, whereas the CDFT calculations were conducted by my collaborator Natacha Gillet.

4.1. Studied Systems

Here, we study hole-transfer between equivalent donor and acceptor molecules over various bridges. Our aim is to measure the influence of barrier height (IP or HOMO energy difference), and barrier width on the electronic coupling. To this end we consider a group of D-B-A system built from hetero-cyclopentadienes such as pyrrole, imidazole or furane shown in figure 4.1. In these systems the type and number of bridging molecule can

vary, as well as the distance between donor and acceptor. The distance between each molecule is 3.5 Å (for system **1**, **2**, **3**, **6**, **7**), 4.5 Å (for system **4**), or 5.5 Å (for system **5**). The angle between the π -system has obviously a great influence on the electronic coupling, but in order to facilitate the modeling and to increase the coupling, we choose parallel stacks of the molecules. For modeling of hole-transfer, the bridge needs to have a higher energy than the donor and acceptor molecules in order to avoid barrierless charge transfer to the bridge. This was confirmed by calculation of the ionization potential (IP) and HOMO energy for each molecule at the DFT level with various functionals and with DFTB.

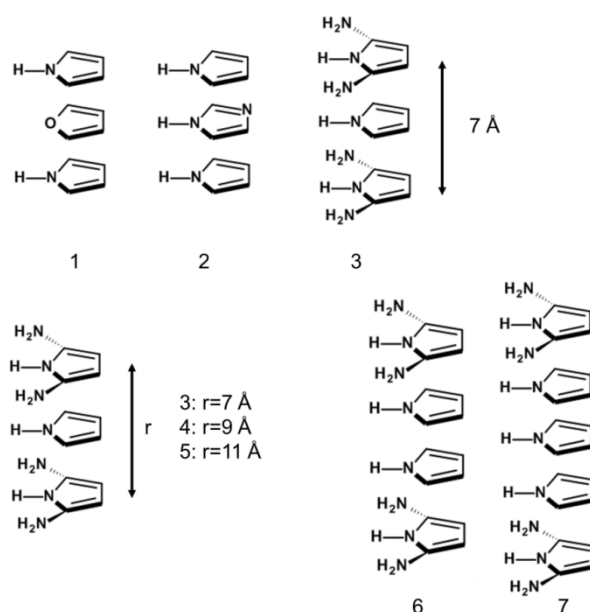


Figure 4.1.: Hetero-cyclopentadiene systems for studying various factors that affect T_{DA} . First set (system **1**, **2**, **3**): influence of the energetic separation between B and D/A. Second set (systems **3**, **4** and **5**): influence of D-A distance. Third set (systems **3**, **6**, **7**): influence of the number of bridging molecule.

4.2. Computational Details

4.2.1. Geometry Optimization

The monomers of all hetero-cyclopentadienes were optimized within the GAMESS computational chemistry software, using the DFT functional B97-D,¹⁵¹ a very fine grid, tight

convergence, and the triple- ζ basis KTZCPP.¹⁵² The energy minimum of the monomers was confirmed by a subsequent vibrational analysis. The D-B-A systems were constructed by placing the monomers in a cofacial orientation at the respective distances shown in figure 4.1.

4.2.2. DFTB Calculations

In the calculations of the bridge-mediated coupling, the block-matrix method described in section 3.2 was used for the construction of the FO Hamilton matrix at the DFTB2 level of theory. For the diagonal blocks, the mio-1-1 parameters^{136,138,139} were used, whereas a weaker confinement was applied for the parameters of the off-diagonal blocks. For latter parameters, a confinement radius of 8 a.u. was applied for the wave function and ∞ for the density. The total energy of the monomer calculations was converged within 10^{-7} a.u.. Only HOMOs were considered on each molecule, which were orthogonalized according to the method of Löwdin.⁹⁴ All the other DFTB calculations were performed with the DFTB+ program¹⁵³ with the same energy convergence criterion and the mio-1-1 parameters.

4.2.3. CDFT Calculations

CDFT calculations were performed with the deMon2k program using various GGA and hybrid functionals and the cc-pVTZ basis set. The applied functionals were PBE¹³² (0%), TPSS^{154,155} (0%), B3LYP¹⁵⁶ (20%), PBE0¹⁵⁷ (25%), PBE50 (50%), BHHLYP¹⁵⁸ (50%) with the different fraction of non-local Hartree-Fock exchange indicated in the brackets. An SCF energy convergence criterion of 10^{-8} a.u. was requested for all calculations and a convergence criterion of 10^{-4} were requested for CDFT constraint. An adaptive grid with a tolerance of 10^{-6} a.u. was used for the numerical integration of the XC energy and matrix elements of the associated potential. Fixed fine-grid accuracy is also specified for the Hirshfeld charge analysis.

4.3. Results

The results for all systems are collected in table 4.1. For FODFTB the contribution of direct through space coupling between D and A to the total electronic coupling T_{DA} can be distinguished. As expected, this contributions is quite small ($<10\%$) for the

studied systems and gets negligible at larger distances. In general, CDFT calculations yield decreasing values for T_{DA} with increasing fraction of exact exchange included in the functional. This is the same behavior that we already observed in section 3.3.

Table 4.1.: Total electronic coupling T_{DA} (in eV) for systems shown in figure 4.1 with D-A distance R_{DA} (in Å). For FODFTB also the direct through vacuo coupling H_{DA} is given.

sys.	R_{DA}	CDFT						FODFTB	
		PBE	TPSS	B3LYP	PBE0	PBE50	BHLYP	T_{DA}	H_{DA}
1	7.0	0.1923	0.1657	0.1480	0.1297	0.0961	0.0957	0.1580	0.0114
2	7.0	0.1742	0.1500	0.1330	0.1154	0.0849	0.0852	0.1700	0.0092
3	7.0	0.1714	0.1509	0.1257	0.1096	0.0777	0.0767	0.0804	0.0079
4	9.0	0.0163	0.0124	0.0088	0.0064	0.0040	0.0044	0.0031	0.0002
5	11.0	0.0004	0.0003	0.0003	0.0002	0.0001	0.0001	0.0001	0.0000
6	10.5	0.1859	0.1523	0.0794	0.0575	0.0251	0.0250	0.0412	0.0003
7	14.0	0.2648	0.2198	0.0712	0.0401	0.0085	0.0085	0.0221	0.0000

Stretching the System

Lets start with the simplest set of systems. Systems **3**, **4**, and **5** are basically the same D-B-A complex with exceedingly increased D-A distance, which allows us to describe the distance dependence of the electronic coupling. All methods give similar results, which are shown in figure 4.2. As expected, a strong exponential decay can be observed following $T_{DA} \sim e^{\beta R_{DA}}$ with a decay constant β of roughly -1.5 \AA^{-1} . This value is in agreement with the decay constants found in section 3.3.3 for cyclopentadien, considering the slightly different definition of the decay constant (see eq. 3.7).

Increasing the Length of the Bridge

In a second set of systems (systems **3**, **6**, **7**) we investigate how the decay changes, when we increase the D-A distance by placing additional bridge molecules in the system. Note that the nature of D,A, and B molecules and their nearest neighbor distance still remains the same. Again, an exponential dependence of T_{DA} on the distance can be observed. However, largely different values for β can be found.

For FODFTB calculations, we find a decrease of T_{DA} with distance, but the decay constant β is only about 10% the value of the previous set. The weaker decay is expected,

if we consider that by placing bridge molecules in the gaps we decrease the tunneling barrier from the vacuum level to the bridge HOMO level in this regions.

For CDFT calculations, the exponential decay of T_{DA} gets weaker with decreasing fraction of non-local exchange in the functional, up to the point where T_{DA} *increases* with the length of the bridge. This unexpected behavior might be explained in the context of fragment orbitals. Strong coupling between the HOMOs of the bridge molecules leads to an energetic splitting between delocalized bridge orbitals. If this splitting is sufficiently large, the barrier between D/A and lowest bridge orbital decreases, which counteracts the decrease of T_{DA} resulting from the increased distance. How well this fragment orbital consideration carries over to CDFT calculations is uncertain, however.

Changing the Barrier Height

Last we study the set where the bridge molecules are altered in order to change the tunneling barrier height ΔE . Before turning to the electronic coupling, we first check what values of ΔE are predicted by each method. The barrier height is defined as

$$\Delta E = I_B - I_{D/A} \quad (4.6)$$

where I_B and $I_{D/A}$ are the vertical IPs of the B and D/A molecule, respectively. As can be seen in table 4.2, all DFT calculations agree that the highest barrier is found in system **1**, followed by system **2** and system **3**. However, there is a significant deviation of more than 0.3 eV from barriers that are calculated from the experimental IPs.¹⁵⁹ For the last systems no experimental reference is given, because no experimental data was available for the IP of 1H-pyrrole-2,5-diamine. Compared to DFT, DFTB2 gives a different ordering for the barrier heights of these systems.

Nevertheless, we compare the resulting T_{DA} of all methods with the respective ΔE in figure 4.4. Here, we see that the effective Hamiltonian method yields the expected decrease of T_{DA} with increasing barrier height. In CDFT calculations, on the other hand, slightly increased values of T_{DA} are obtained with higher barriers. This unphysical behavior might partly result from our definition of ΔE , which is calculated from the IP of isolated molecules in vacuo, whereas in the complex interactions with neighboring molecules would affect the IP of the individual molecules. Nevertheless, CDFT calculations seem to experience serious problems in the description of these systems.

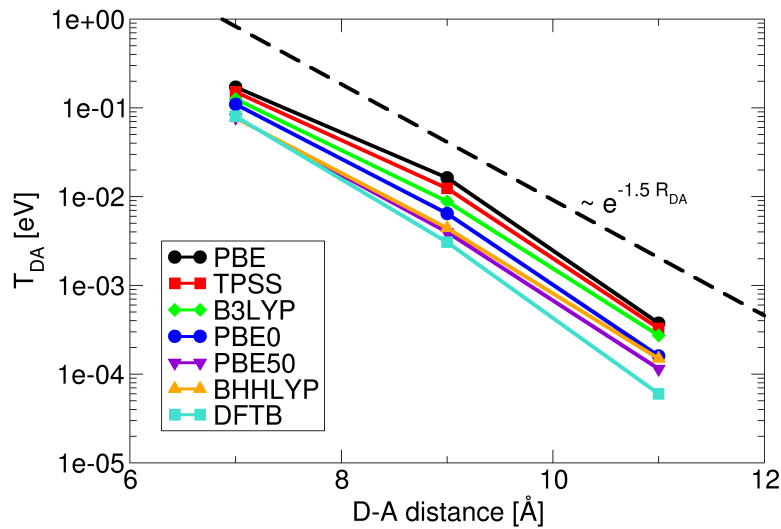


Figure 4.2.: T_{DA} for increasing D-A distance (system **3**, **4**, **5**). For all methods a similarly strong exponential decay with increasing distance can be found. The dashed line serves as a guide to the eye and shows a decay constant of 1.5 \AA^{-1} .

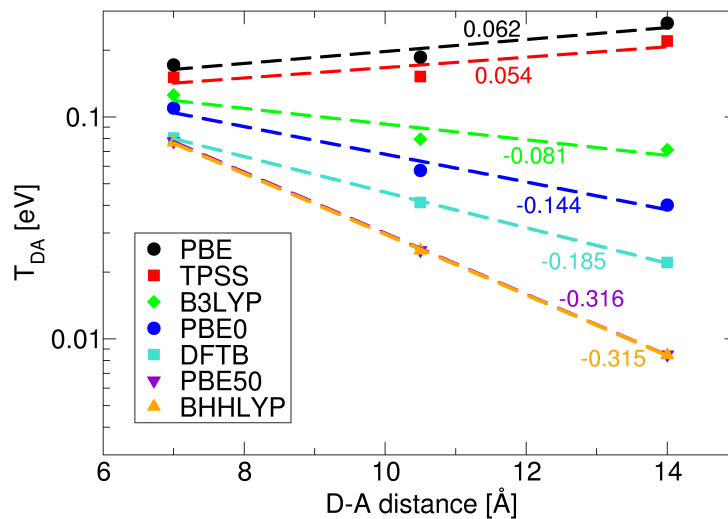


Figure 4.3.: Dependence of T_{DA} on the length of the bridge (system **3**, **6**, **7**), which can nicely be fitted with $T_{DA} = C * \exp(n * R_{DA})$ (dashed lines) with the resulting exponent n (in \AA^{-1}) shown in the graph. A weaker decay than in figure 4.2 can be observed, strongly dependent on the fraction of non-local exchange in the DFT functional.

Table 4.2.: Tunneling barriers for the systems shown in figure 4.1 calculated as difference between vertical IPs of B and D/A. Reference values are differences of experimental IPs (8.88, 8.21, and 8.81 eV of furan, pyrrole and imidazole, respectively).¹⁵⁹

Method	System		
	1	2	3-7
PBE	1.161	0.701	0.681
TPSS	0.789	0.693	0.630
B3LYP	1.029	0.700	0.608
PBE0	1.117	0.691	0.600
PBE50	1.071	0.678	0.553
BHHLYP	1.023	0.681	0.536
DFTB2	0.416	0.330	0.652
Reference	0.67	0.60	–

For the same barrier height we find higher couplings for functionals with smaller fraction of non-local exchange. This shows that different barrier heights are not the cause for the observed functional dependence of T_{DA} . This is in agreement with the findings in section 3.3, where the same trend was observed for barrier-less transport between donor and acceptor molecules. In ref. 115 the decreasing CDFT coupling with increasing fraction of non-local exchange was attributed to more confined spin densities and thus smaller overlap between the localized states.

4.4. Discussion and Conclusion

In conclusion we find that the dependence of T_{DA} on the conformational changes of the systems is quite well reproduced within all methods. Here, we only investigated an increase of the D/A distance, whereas in further studies also other changes in the relative orientation of D,A and B have to be investigated. Nevertheless, these first results are promising for the application of FODFTB for the sampling of T_{DA} in different molecular conformations along MD simulations.

In contrast, the effect on T_{DA} resulting from molecular changes of the system, like increase of the bridge length or altering the bridging molecules, is difficult to predict. One problem that arises in this context is the precise prediction of the tunneling barrier height. Due to approximations in the exchange-correlation potential of presently available DFT functionals, the relative energy levels of D,B, and A are not always well reproduced,

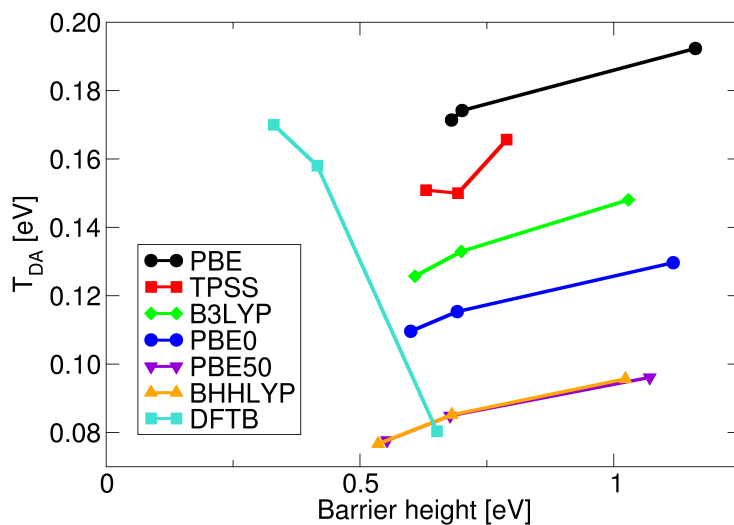


Figure 4.4.: T_{DA} for different bridging molecules (system **1**, **2**, **3**) and thus barrier heights. The expected decrease of T_{DA} with increasing barrier height is only found with the effective Hamiltonian DFTB method, whereas in CDFT calculations even a slight increase can be observed.

which obviously affects the resulting T_{DA} . With an effective FO Hamiltonian approach, however, it is possible to correct the erroneous energy landscape, as we have discussed in ref. 173 in detail. This is achieved by calculating site energies accurately at a high level of theory in order to obtain reliable reference values. The erroneous site energies can then be corrected by applying a constant shift during the T_{DA} calculation.

Advancements in Coupled Electron Ion Dynamics

Reproduced in part with permission from
A. Heck, J. Kranz, T. Kubař and M. Elstner, *J. Chem. Theory
Comput.*, 2015, **11**, 5068–5082.
© 2015 American Chemical Society.

Our goal is to derive an approximate simulation technique that is efficient while still making use of essential atomistic information. After revealing the shortcomings of the conventional coupled electron ion dynamics (CEID) method (see section 2.3.3) in section 5.1, we derive in the same spirit a total energy expression of the system, which allows to make use of established time-propagation schemes. Since a time-dependent QM description of a realistic system consisting of more than 1000 atoms is too costly, several approximations are needed, which can be summarized as follows:

- First (section 5.2), we restrict the dynamic evolution of the electron density to certain parts of the electronic system, considering the remainder as electronically frozen. On the one hand, we divide the system into two regions: a quantum mechanical (QM) region, where the charge carrier is located, and the remainder of the system, which is described by a classical force field (molecular mechanics: MM), i.e. we introduce the common QM/MM separation. However, we further simplify the description of the charge carrier by considering only several frontier

orbitals around the Fermi level, e.g. highest occupied molecular orbitals (HOMOs) in case of hole transfer and lowest unoccupied molecular orbitals (LUMOs) in case of electron transfer, whereas strongly bound core states are approximated to stay unaffected in the charged system.¹⁰⁹ The wave function $|\Psi\rangle$ describing the state of the charge carrier is then expressed as a linear combination of these orbitals. Therefore, we go beyond the standard QM/MM separation, freezing not only states that are spatially, but also states that are energetically well separated from the orbitals that are relevant for charge transport.

- Second (section 5.2.1), we partition the system via a fragment orbital (FO) formalism, which leads to a linear scaling with the system size. In molecular semiconductors, this partitioning refers to the molecular building blocks naturally. Therefore, the QM region is dissected into N QM regions (fragments) containing one organic molecule each. For every fragment, a quantum chemical calculation is performed, and the orbitals $|\phi_m\rangle$ at each molecular fragment are used to build the wave function $|\Psi\rangle$ of the charge carrier. As will be discussed below, several HOMO or LUMO orbitals per molecule can be included for the representation of $|\Psi\rangle$.
- Third (section 5.2.2), we use an approximate DFT method for the QM calculations on the fragments, the density functional tight-binding (DFTB) method. This is a method derived from DFT, which is roughly 2-3 orders of magnitude faster than DFT with medium sized basis sets and thus accelerates the simulations significantly.
- Fourth, to derive coupled equations of motion for the electronic (section 5.3) and nuclear (section 5.4) subsystems, we apply the standard mean-field (Ehrenfest) propagation techniques. This allows a classical propagation of the nuclei combined with a propagation of the time dependent Schrödinger equation for the hole/electron wave function.

5.1. Influence of Self-Interaction on the Charge Evolution

In our model we describe the molecular organic semiconductors in a basis of charge localized diabatic states, where each state describes the charge carrier residing on one molecule. However, by propagating the charge we go beyond a hopping description and allow the excess charge to delocalize in a linear combination of these states, which leads to partial charged molecules. In section 2.1.3 we have seen how partial charged systems get stabilized by the self-interaction. Ultimately, however, we are not interested in the

total energy but rather the charge carrier dynamics. To this end, we will study the time evolution of the charge carrier in a simple model system. Our model consists of two sites A and B without any electron-phonon coupling. First, we use a charge-independent Hamilton matrix as self-interaction-free reference

$$\mathbf{H} = \mathbf{H}_0 = \begin{pmatrix} \epsilon_A & J \\ J & \epsilon_B \end{pmatrix} \quad (5.1)$$

where the matrix elements represent $\langle \Psi_A | \hat{H} | \Psi_B \rangle$ with \hat{H} being the exact Hamiltonian shown in eq. 2.2 and $|\Psi_A\rangle$ as well as $|\Psi_B\rangle$ are charge-localized diabatic states as in eq. 2.65. We choose for the site energies $\epsilon_A = \epsilon_B = 0$ and for the electronic coupling $J = 50$ meV, which is a reasonable value for π -stacked molecules.

Propagation of an initially localized wave function with this Hamiltonian leads to the expected time evolution shown in the top panel of figure 5.1. Since we do not start in an eigenvector of \mathbf{H}_0 , an oscillation of the wavefunction can be observed, where the charge gets completely transferred between site A and B with a frequency of about 40 fs.

In previous applications to biomolecules^{109,110} the QM energy term from eq. 2.104 was used with additional charge dependent contributions

$$E_{QM}^+ = - \sum_{AB} c_A^* c_B H_{AB}^0 + \frac{1}{2} \sum_{AB} |c_A|^2 |c_B|^2 \Gamma_{AB} \quad (5.2)$$

which leads to a charge dependent Hamiltonian

$$H_{AB} = -H_{AB}^0 + \delta_{AB} \sum_{K=A,B} (\Gamma_{AK}) \Delta Q_K \quad (5.3)$$

where Γ_{AA} is a molecular Hubbard parameter, describing charge dependent relaxation effects, Γ_{AB} describes electrostatic interactions between the charged sites with $1/R_{AB}$, ΔQ_K is the occupation of site K , and δ_{AB} is the Kronecker delta. We consider the same \mathbf{H}_0 as in eq 5.1, set $\Gamma_{AB} = 4.0$ eV/e², representing the electrostatic repulsion of partial charges in 3.5 Å distance, and take a molecular Hubbard parameter of $\Gamma_{AA} = 5.4$ eV/e², which is a reasonable value for medium sized π -systems. When this Hamiltonian is used for the propagation, the charge transfer is completely suppressed, and the initial wave function stays localized at its initial site. It was pointed out that the introduction of charge dependent terms to achieve a self-consistent Hamiltonian has effects similar to the SI in DFT, leading to over-delocalization and erroneous dissociation behavior.⁶⁸

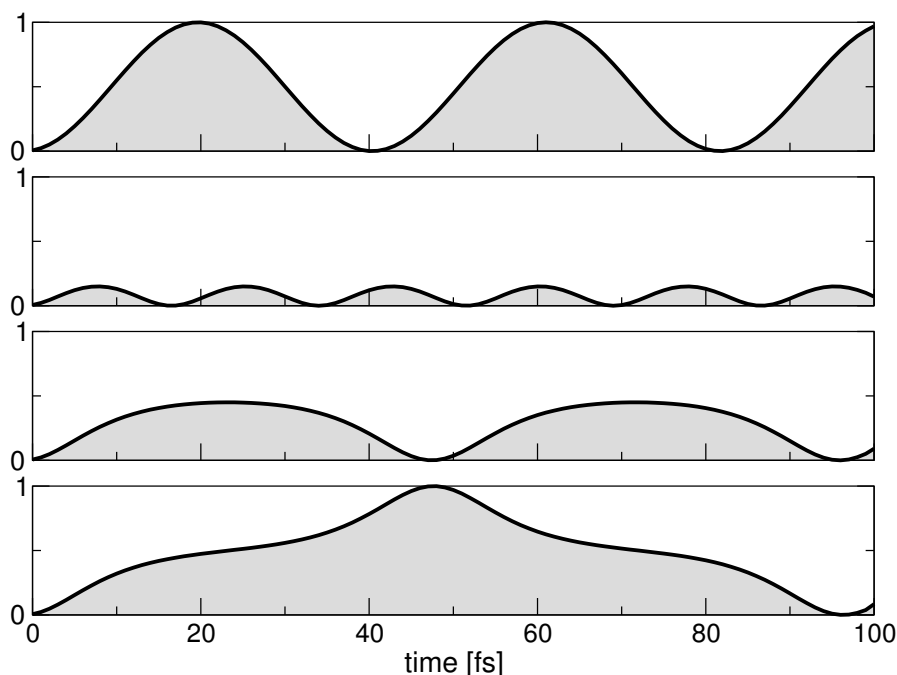


Figure 5.1.: Time evolution of the occupation of the acceptor in a two-site system. Without artificial stabilization of the delocalized state (top panel) the occupation oscillates between donor and acceptor. With a Hamiltonian where the charge-dependent terms are reduced to 20%, like in eq. 5.3, only little charge gets transferred (second panel). The threshold where complete charge transfer gets possible is when the charge-dependent terms are further reduced such that the artificial stabilization of the delocalized charge is 1 meV larger (third panel) or smaller (bottom panel) than the coupling J . The transfer is nevertheless hindered in both cases.

Therefore, this example is to some extent also showing the problems one might encounter with SI-prone methods in general. It was proposed to scale the second terms in eq 5.3 with a factor of 0.2 in order to mitigate the SI of the additional charge carrier.¹⁰⁹ However, even with the scaled second order terms only a small fraction of charge gets transferred to the acceptor as can be seen in the second panel of figure 5.1.

Following the work of Irle et al. we will quantify the artificial stabilization.⁶⁸ Minor differences are that the QM energy of the cationic system is calculated relative to the neutral MM reference system and spin polarization is ignored in our QM/MM framework. The general findings are, however, the same. Like above we consider a symmetric dimer

and calculate the site energy of a monomer in different charge states.

$$E(A) = 0 \quad (5.4)$$

$$E(A^+) = -\epsilon_A + \frac{1}{2}\gamma_{AA} \quad (5.5)$$

$$E(A^{+0.5}) = -\frac{1}{2}\epsilon_A + \frac{1}{2} \times 0.5 \times 0.5 \times \gamma_{AA} = -\frac{1}{2}\epsilon_A + \frac{1}{8}\gamma_{AA} \quad (5.6)$$

where $E(A)$, $E(A^+)$, $E(A^{+0.5})$ are the energies of the molecule with a net charge of zero, one, and one half, respectively. The delocalization energy (E_{del}), that is, the stabilization of the delocalized solution compared to the localized one, is at infinite distance given as:

$$E_{del}(R = \infty) = 2E(A^{+0.5}) - (E(A) + E(A^+)) = -\frac{1}{4}\gamma_{AA} \quad (5.7)$$

While the delocalization error is the largest at infinite distance, a spurious stabilization of the delocalized solution can be expected at all distances. At shorter distances, however, additional contributions to the delocalization energy emerge. For fragments at vdW distance and beyond, the electronic coupling is small, and the interaction between the two fragments is dominated by Coulomb interactions. This causes an additional charge repulsion term for the delocalized solution

$$E_{coul} = 0.5 \times 0.5 \times \gamma_{AB}(R_{AB}) \quad (5.8)$$

which is positive for all separation distances R_{AB} of the monomers and therefore counteracts the delocalization. The delocalization energy due to the self-interacting charge is therefore

$$E_{del}(R_{AB}) = 2E(A^{+0.5}) - E(A) - E(A^+) + E_{coul} = -\frac{1}{4}(\gamma_{AA} - \gamma_{AB}) \quad (5.9)$$

After quantifying the artificial stabilization we want to see what happens for $|J| > |E_{del}|$ and $|J| < |E_{del}|$. As long as the delocalization energy is larger than the coupling, the charge never gets completely transferred to the acceptor, as can be seen in the third panel of figure 5.1. For the case where the coupling is larger than the delocalization energy, there is an oscillation between site A and B, however, the transfer is hindered significantly compared to the SI-free propagation shown in the first panel. The qualitatively different dynamics for $E_{del} > J$ and $E_{del} < J$ further confirms the delocalization energy as the cause of the unphysical dynamics.

Note that the fluctuation of site energies, caused by electron-phonon coupling, will ob-

secure the erroneous dynamics. In aqueous environments, the polarization of the environment leads to site energy differences of more than 1 eV,^{109,110,160,161} which completely overrules the effect of the SI error. In organic semiconductors, however, the site energy differences are significantly smaller. Therefore, simulations of anthracene with the charge-dependent Hamiltonian lead to the described trapping of the charge carrier on a single site.

5.2. Self-Interaction-Free Total Energy Expression of the Charged System

Since the SI leads to erroneous charge dynamics, we will set up a SI-free total energy expression, from which we can derive equations of motions for the excess charge and the nuclei. The starting point is the DFT energy of the charged system where environmental effects are included via classical force field terms.

$$E^+ = E_{DFT}[\rho] + E_{MM} + E_{QM/MM} \quad (5.10)$$

Here, ρ is the density of the QM zone including the hole charge carrier, and $E_{QM/MM}$ is its electrostatic coupling to the neutral MM environment E_{MM} .

According to Janak's theorem, $E_{DFT}[\rho]$ of a cationic system can be divided into the energy of the neutral QM zone with density ρ_0 and the negative of its HOMO energy.

$$E^+ = E_{DFT}[\rho_0] - \langle \Psi^0 | H[\rho_0] | \Psi^0 \rangle + E_{MM} + E_{QM/MM} \quad (5.11)$$

Note that the calculation of a charged system with an odd electron number is avoided also, this way. For such cases, it is known that the SI error of DFT has tremendous influence on the localization of the charge.⁶⁷ In principle, there are three factors that may reduce the SI error: a high relaxation energy, a short distance between the fragments, and asymmetric fragment energies.⁶⁷ However, the opposite is the case in organic semiconductors regarding all factors. Note that anionic systems would be treated analogously by adding the LUMO energy in eq 5.11. For clarity, we will restrict ourself to the cationic case in this work.

Next, also $E_{DFT}[\rho_0]$ will be approximated with the MM force field, which reduces the complexity dramatically and enables to combine the energy of the neutral QM zone with

that of the environment

$$E_{DFT}[\rho_0] + E_{MM} + E_{QM/MM} \approx E_{MM}^{tot} + \Delta E_{QM/MM} \quad (5.12)$$

where E_{MM}^{tot} is the force field energy of the *whole* neutral system including all atoms of the MM as well as QM region, and $\Delta E_{QM/MM}$ is the change of QM/MM interaction relative to the neutral system. Note that this approximation may even be superior to the original expression in eq 5.11, since it ensures that unoccupied molecules inside the QM region experience the same potential energy surface as the molecules of the classical environment. For example, the unit cell of molecular crystals might have a slightly different geometry when calculated with QM or MM methods. Therefore, treating equal molecules at different levels of theory, depending on their classification as QM or MM, could compromise the translational symmetry of the crystal.

5.2.1. Fragmentation of the System

In the following, we make use of the morphology of organic semiconductors, which consist of weakly bound molecules. In contrast to Bloch waves of inorganic crystalline semiconductors, organic bulk materials preserve the underlying molecular electronic structure to a large extent (see Figure 5.2). This allows a coarse graining of the electronic structure of the complex by expressing the total density as a superposition of molecular densities, and expanding the hole wavefunction as a linear combination of molecular orbitals $|\phi_m\rangle$ on fragment molecules A .

$$|\Psi^0\rangle = \sum_A \sum_{m \in A} a_m |\phi_m\rangle \quad (5.13)$$

$$\rho_0 = \sum_A \rho_A^0 \quad (5.14)$$

The orbitals and densities of the fragments can be obtained in independent calculations leading to linear scaling and parallelizability. Inserting eq 5.12 and 5.13 into 5.11 we obtain the total energy expressed in a fragment orbital basis

$$E^+ \approx E_{MM}^{tot} - \sum_{AB} \sum_{m \in A} \sum_{n \in B} a_m^* a_n \langle \phi_m | H[\rho_0] | \phi_n \rangle + \Delta E_{QM/MM} \quad (5.15)$$

Whenever needed, the representation in the atomic orbital basis is available via the expansion of FOs in AOs

$$|\phi_m\rangle = \sum_{\mu} c_{\mu}^m |\mu\rangle \quad (5.16)$$

leading to

$$E^+ \approx E_{MM}^{tot} - \sum_{\mu\nu} b_{\mu}^* b_{\nu} \langle \mu | H[\rho_0] | \nu \rangle + \Delta E_{QM/MM} \quad (5.17)$$

with $b_{\mu} = \sum_A \sum_{m \in A} a_m c_{\mu}^m$. However, the FO description gives access to corrections of the QM method. On the one hand, the off-diagonal elements can be scaled, as suggested in section 3.3.5, in order to compensate for missing non-local exchange. On the other hand, the FO representation allows to correct the relative site energies by applying a shift to the FO diagonal elements.

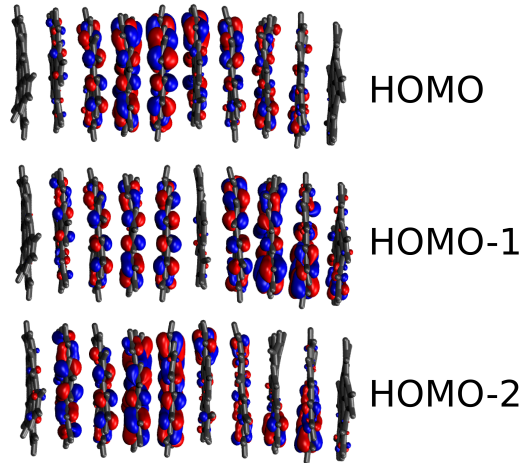


Figure 5.2.: Highest occupied molecular orbitals obtained at the PBE/def2-SVP level during a molecular dynamic simulation. The MOs of the complex are linear combination of MOs of the individual molecules.

In many cases, the HOMO of the system $|\Psi^0\rangle$ is already well described by a linear combination of the HOMO of each fragment. Additional FOs can be included in cases where lower lying orbitals have similar energy. The construction of coarse grained FO basis functions shows some analogies to contracted basis sets like GTOs. Whereas several Gaussians are contracted to yield a suitable atomic basis function, in our case, several AOs are contracted into an FO basis function that can properly describe a hole on this fragment. The dimension of the Hamilton matrix in this coarse grained representation is significantly reduced compared to a full AO basis, while it is still able to describe

the hole wavefunction accurately. While FOs on the same fragment are orthogonal by construction, there is a small overlap between FOs on different fragments. To facilitate further calculations, the included FOs are orthogonalized at every step with the Löwdin method.⁹⁴ In this work, fragment orbitals $|\phi_m\rangle$ and their FO coefficients c_μ^m will denote the respective quantities after the orthogonalization procedure, whereas a prime will be added to denote their non-orthogonalized counterparts.

5.2.2. Approximations in the Quantum Calculations

In a next step, the matrix elements $\langle\mu|H|\nu\rangle$ in eq 5.17 have to be computed with a quantum chemical method, which can be HF, DFT or a semi-empirical one. For simulations over several picoseconds and meaningful statistical sampling, DFT calculations are prohibitively slow, and greater efficiency is needed. Recent tests have shown that semi-empirical methods are able to compute such matrix elements in DNA with a very good accuracy, comparable to HF and DFT.^{118,162} Furthermore, in chapter 3 we have proven the applicability of DFTB for the calculation of electronic couplings in a wide range of organic π -conjugated molecules, explicitly.

For this reason, we use the approximate DFT method DFTB described in section 2.1.2, which provides an additional speed up of three orders of magnitude compared to DFT-GGA calculations.^{56,163}

By equating $\langle\mu|H[\rho_0]|\nu\rangle = H_{\mu\nu}^{DFTB}$ we obtain e.g. within the DFTB2 formalism (see section 2.1.2)

$$H_{\mu\nu}^{DFTB} = H_{\mu\nu}^0 + \frac{1}{2}S_{\mu\nu} \sum_{\xi} \Delta q_{\xi} (\gamma_{\alpha\xi} + \gamma_{\beta\xi}) \quad (5.18)$$

$H_{\mu\nu}^0$ are DFTB1 Hamilton matrix elements between atom α and β , where the neutral atomic densities are used in the effective Kohn-Sham potential. The γ functions are introduced in DFTB2 and describe how deviations from the reference density (expressed as Mulliken charge differences Δq_{ξ} on atom ξ) affect the total energy. The charge-dependent terms require a self-consistent solution, which is beneficial for polar systems with a sizeable charge transfer between the atoms. For non-polar molecules like the organic molecules studied in this work, the charge-density fluctuations are negligible, i.e. the DFTB1 approach gives nearly identical results to DFTB2, as discussed in detail in ref. 164. At the same time, the self-consistent solution due to the charge dependence in DFTB2 requires about ten times more computation time than the non-self-consistent DFTB1 scheme. Therefore, we limit our calculations in this work to DFTB1 due to

the non-polar character of the investigated molecules, gaining an additional order of magnitude in speed.

For long-range interactions, the density is represented in DFTB as atomic point charges, which leads to the following QM/MM term:

$$\Delta E_{QM/MM} = \sum_A \sum_{m \in A} |a_m|^2 \sum_K \sum_{\alpha \in A} \left(\frac{\Delta q_\alpha^m q_K^0}{|R_\alpha - R_K|} \right) \quad (5.19)$$

where q_K^0 is the force-field partial charge on atom K of the neutral environment, and $\Delta q_\alpha^m = \frac{1}{2} \sum_\mu \sum_{\nu \in \alpha} (c_\mu^{m*} c_\nu^m S_{\mu\nu} + c_\nu^{m*} c_\mu^m S_{\nu\mu})$ is the change of Mulliken charge on atom α resulting from a hole residing in orbital m .

By applying the variational principle, we obtain an additional term in our Hamiltonian

$$H_{\mu\nu}^{QM/MM} = \frac{1}{2} S_{\mu\nu}^{\alpha\beta} (\varphi_\alpha + \varphi_\beta) \quad (5.20)$$

where μ is located on atom α , ν is on atom β . The electrostatic potential on the position of atom α is given as

$$\varphi_\alpha = \sum_K \frac{q_K^0}{R_{\alpha K}} \quad (5.21)$$

where $R_{\alpha K}$ is short for $|R_\alpha - R_K|$. This potential can be obtained from summation in real-space or for periodic systems the calculation of long-range electrostatic can be performed with the particle-mesh Ewald method, which is already implemented in MD programs like Gromacs.^{165,166}

5.3. Propagation of Electronic Degrees of Freedom

With the total energy expression at hand, equations of motions for atoms and electrons can be derived in the framework of time-dependent DFT. Similarly to previous work,^{109,110} we apply the Lagrangian formalism:

$$L = T - V \quad (5.22)$$

$$T = \sum_K \frac{1}{2} m_K \dot{R}_K^2 + \langle \Psi | -i \frac{\partial}{\partial t} | \Psi \rangle \quad (5.23)$$

$$V = E_{MM}^{tot} - \langle \Psi | H[\rho_0] | \Psi \rangle + \Delta E^{QM/MM} \quad (5.24)$$

The Lagrangian in FO basis reads

$$L = \sum_K \frac{1}{2} m_K \dot{R}_K^2 - i \sum_{mn} \left[a_m^* a_n \langle \phi_m | \dot{\phi}_n \rangle + a_m^* \dot{a}_n \langle \phi_m | \phi_n \rangle \right] \quad (5.25)$$

$$- E_{MM}^{tot} + \sum_{mn} a_m^* a_n \langle \phi_m | H[\rho_0] | \phi_n \rangle - \sum_m |a_m|^2 \frac{\Delta q_\alpha^m q_K^0}{R_{\alpha K}} \quad (5.26)$$

Using the Lagrangian equation for the electronic degrees of freedom

$$\frac{\partial L}{\partial a_m^*} - \frac{d}{dt} \frac{\partial L}{\partial \dot{a}_m^*} = 0 \quad (5.27)$$

where

$$\frac{\partial L}{\partial \dot{a}_m^*} = 0 \quad (5.28)$$

we arrive at

$$\frac{\partial L}{\partial a_m^*} = -i \sum_n \left[a_n \langle \phi_m | \dot{\phi}_n \rangle + \dot{a}_n \langle \phi_m | \phi_n \rangle \right] + \sum_n a_n \left[\langle \phi_m | H[\rho_0] | \phi_n \rangle - \delta_{mn} \sum_\alpha \sum_K \frac{\delta q_\alpha^m q_K^0}{R_{\alpha K}} \right] \quad (5.29)$$

Since we are using an orthogonal basis ($\langle \phi_m | \phi_n \rangle = \delta_{mn}$) we arrive at

$$\dot{a}_m = -i \sum_n H_{mn} a_n - \sum_n a_n \langle \phi_m | \dot{\phi}_n \rangle \quad (5.30)$$

where H_{mn} are the matrix elements of the FO Hamiltonian from eq 3.2, incorporating QM/MM interactions. The last term in eq 5.30 vanishes if a spatially fixed orthogonal basis (e.g. plane waves) is used. In an atom-centred basis set, however, additional terms arise from the time dependent origin of the basis functions.¹⁶⁷ By writing $\langle \phi_m | \dot{\phi}_n \rangle$ as $\langle \phi_m | \frac{\partial}{\partial R} | \phi_n \rangle \frac{\partial R}{\partial t}$, it becomes clear that the coupling gets important for high-velocity collisions and atoms that are close to each other, but it vanishes for sites that are far apart and at low temperature. As a first approximation, these terms are therefore omitted in the propagation according to 5.30.

However, the coupling terms $\langle \phi_m | \dot{\phi}_n \rangle$ give also rise to transitions between orbitals on the same molecule, whose impact we will examine in section 6.7. In general, if the non-adiabatic coupling between $|\phi_m\rangle$ and $|\phi_n\rangle$ is small while they are energetically crossing, the charge carrier will follow its initial state through the crossing region and end up in the excited state. If, on the other hand, the coupling is large, the charge carrier will stay in the ground state all the time. To evaluate the influence of the non-adiabatic coupling

between the degenerate FOs, we apply two different approaches in the simulation of HBC. (1) We take no special care in the expansion of the charge carrier wavefunction when the (nearly) degenerate FO basis functions of one molecule cross. A charge carrier residing in the highest FO will therefore remain in the highest FO after a crossing event, which corresponds to the limit of a large non-adiabatic coupling. (2) After the propagation $t_1 \rightarrow t_2$ performed in the basis at t_1 , we project the obtained wavefunction $|\Psi(t_2)\rangle_{t_1}$ onto the new basis at t_2 .

$$|\Psi(t_2)\rangle_{t_2} = \sum_m |\phi_m(t_2)\rangle \langle \phi_m(t_2)|\Psi(t_2)_{t_1}\rangle = \sum_{mn} a_n |\phi_m(t_2)\rangle \langle \phi_m(t_2)|\phi_n(t_1)\rangle \quad (5.31)$$

This way, the charge carrier is forced by projection to the orbital with the same character, which corresponds to the limit of zero non-adiabatic coupling. We approximate $\langle \phi_m(t_2)|\phi_n(t_1)\rangle$ by calculating $\langle \phi'_m(t_2)|\phi'_n(t_1)\rangle$ on each site in the non-orthogonal basis.* Note that a projection would only be norm-conserving with a complete basis set. Therefore the wavefunction has to be renormalized after the projection.

5.4. Propagation of Nuclear Degrees of Freedom

The Lagrange equation for the nuclear degrees of freedom is given by

$$\frac{d}{dt} \frac{\partial L}{\partial \dot{R}_k} = \frac{\partial L}{\partial R_k} \quad (5.32)$$

which yields

$$m_K \ddot{R}_k = -\frac{\partial E_{MM}^{tot}}{\partial R_k} + \sum_{mn} a_m^* a_n \frac{\partial}{\partial R_k} \langle \phi_m|H[\rho_0]|\phi_n\rangle - \frac{\partial}{\partial R_k} \Delta E^{QM/MM} \quad (5.33)$$

where k denotes x, y, z of atom K . The first term originates from the force field and would be the only contribution in a standard molecular dynamic simulation (MD) of a neutral system. The sum contains the diagonal and off-diagonal elements of the coarse grained Hamiltonian. The derivatives of diagonal elements with respect to atomic coordinates are related to the internal relaxation of a single fragment. The derivatives of intermolecular electronic couplings yield the forces resulting from bonding and anti-bonding linear combinations of FOs; terms that are missing in a localized hopping description of the

*During a 100 fs simulation of a dimer of HBC, which is studied in chapter 6, the largest difference in these matrix elements was as small as 7.3×10^{-3} and the RMSD was only 1.2×10^{-5} .

charge dynamics. The last term covers the interaction of the charge carrier with the MM environment and is related to the external (outer-sphere) reorganization energy.

By expanding the FOs in AOs

$$|\phi_m\rangle = \sum_{\mu} c_{\mu}^m |\mu\rangle \quad (5.34)$$

and by approximating $H[\rho_0]$ with the DFTB1 Hamiltonian, we obtain for the second term on the right hand side of eq 5.33

$$\sum_{mn} a_m^* a_n \frac{\partial}{\partial R_k} \langle \phi_m | H[\rho_0] | \phi_n \rangle = \sum_{mn} \sum_{\mu\nu} a_m^* a_n c_{\mu}^m c_{\nu}^n \frac{\partial H_{\mu\nu}^0}{\partial R_k} \quad (5.35)$$

with $\frac{\partial H_{\mu\nu}^0}{\partial R} = \langle \frac{\partial \mu}{\partial R} | H | \nu \rangle + \langle \mu | \frac{\partial H}{\partial R} | \nu \rangle + \langle \mu | H | \frac{\partial \nu}{\partial R} \rangle$ being the derivative of the tabulated DFTB1 matrix elements.

However, the FOs are not only *explicitly* dependent on R via $|\mu\rangle$. The displacement of an atom is also accompanied by a change of the expansion coefficients c_{μ}^m in order to restore the norm of the FO ϕ_m . In order to obtain correct forces, it is therefore necessary that the change of the total energy with respect to all quantities depends on the atomic coordinates explicitly as well as implicitly.^{168,169}

The change in overlap between two AOs is the largest for neighboring atoms of the same fragment, whereas atoms located on different fragments have significant smaller overlap due to its exponential decay. Following this reasoning, the implicit dependence on R is only considered in the diagonal elements of the coarse grained Hamiltonian.

$$\frac{\partial}{\partial R_k} \langle \phi_m | H[\rho_0] | \phi_m \rangle = \sum_{\mu\nu} c_{\mu}^m c_{\nu}^m \frac{\partial H_{\mu\nu}^0}{\partial R_k} + \sum_{\mu\nu} \left(\frac{\partial c_{\mu}^m}{\partial R_k} H_{\mu\nu}^0 c_{\nu}^m + c_{\mu}^m H_{\mu\nu}^0 \frac{\partial c_{\nu}^m}{\partial R_k} \right) \quad (5.36)$$

Here, the first term is the derivative of quantities explicitly dependent on R , which was already present in eq 5.35, whereas the second term captures the additional change of c_{μ}^m that is necessary to conserve the norm.

Since the FOs are (orthogonalized) eigenfunctions of the respective fragment, we approximate

$$\sum_{\mu} H_{\mu\nu}^0 c_{\nu}^m \approx \epsilon_m \sum_{\mu} S_{\mu\nu} c_{\nu}^m \quad (5.37)$$

which transforms the second sum of eq 5.36 into

$$\sum_{\mu\nu} \epsilon_m S_{\mu\nu} \frac{\partial(c_\mu^m c_\nu^m)}{\partial R_k} = \epsilon_m \frac{\partial}{\partial R_k} \left(\sum_{\mu\nu} S_{\mu\nu} c_\mu^m c_\nu^m \right) - \epsilon_m \sum_{\mu\nu} c_\mu^m c_\nu^m \frac{\partial S_{\mu\nu}}{\partial R_k} \quad (5.38)$$

Now, we can demand that the norm of the FO does not change

$$\frac{\partial}{\partial R_k} \langle \phi_m | \phi_m \rangle = \frac{\partial}{\partial R_k} \left(\sum_{\mu\nu} S_{\mu\nu} c_\mu^m c_\nu^m \right) = 0 \quad (5.39)$$

which eliminates the first term on the right hand side of eq 5.38. With this, we get for the diagonal terms of eq 5.36

$$\frac{\partial}{\partial R_k} \langle \phi_m | H[\rho_0] | \phi_m \rangle = \sum_{\mu\nu} c_\mu^m c_\nu^m \left(\frac{\partial H_{\mu\nu}^0}{\partial R_k} - \epsilon_m \frac{\partial S_{\mu\nu}}{\partial R_k} \right) \quad (5.40)$$

Within the DFTB1 method, this is equivalent to $\frac{\partial(E^0 - E^+)}{\partial R}$, where E is the total energy of one fragment molecule in the neutral state and with the charge in orbital ϕ_m , respectively, within the frozen orbital approximation.

For a practical evaluation of the QM/MM coupling term of eq 5.33

$$\frac{\partial}{\partial R_k} \Delta E^{QM/MM} = \frac{\partial}{\partial R_k} \sum_{\alpha A} \frac{\Delta q_\alpha q_A^0}{|R_\alpha - R_A|} \quad (5.41)$$

the instantaneous Mulliken charges of the hole wavefunction Δq_α are added to the force field, which then handles the calculation of forces. The total force expression for the complex is therefore

$$m_K \ddot{R}_k = - \frac{\partial E_{MM}^{tot}(q_A^0, \Delta q_\alpha)}{\partial R_k} + \sum_{mn} \sum_{\mu\nu} a_m^* a_n c_\mu^m c_\nu^n \left(\frac{\partial H_{\mu\nu}^0}{\partial R_k} - \delta_{mn} \epsilon_m \frac{\partial S_{\mu\nu}}{\partial R_k} \right) \quad (5.42)$$

where $E_{MM}^{tot}(q_A^0, \Delta q_\alpha)$ denotes the force field energy of the total system with adapted partial charges.

5.5. Outlook: Electronic Polarization

In our method, the polarization of the neutral sites by the point charges of the environment are considered via the QM/MM coupling terms. Since we add the excess charge to the force field we also capture the slow polarization of the environment originating from the reorientation of the atomic point charges. The instantaneous electronic polarization of the environment, however, is missing as long as non-polarizable force fields are applied. Application of a polarizable force field and considering not only the atomic point charges but also the polarizable dipoles in the QM/MM coupling terms could therefore be a next step in the improvement of the accuracy of CEID simulations.

Furthermore, the FO basis that we obtain within our method can also be seen as approximation to a basis of diabatic states, as described in section 2.2. These diabatic states, represented by a $(N \pm 1)$ electron wave function with the excess charge localized on a single molecule, can be obtained with CDFT calculations (see section 2.2.2).¹⁷⁰ By taking the excess charge explicitly into account in CDFT calculations of the coarse-grained Hamilton matrix elements, the effect of electronic relaxation on the site energies can be captured. However, describing the whole complex with CDFT is computationally too expensive for reasonable system sizes. Furthermore, CDFT calculations are computationally less stable than FO calculations and therefore difficult to apply along MD simulations in a black-box manner. Besides that, the constraint will place the excess charge always in the HOMO/LUMO of the respective molecule, whereas in cases of (nearly) degenerate orbitals there are several states close in energy that are equally important for the transport (see also section 6.9).

A better suited method for capturing the shift of site energies due to electronic polarization is the recently proposed quantum patch approach.^{32,171} Here, electronic relaxation is achieved in independent molecular calculation similar to our FO procedure. In order to capture the effect of electronic polarization on site i , molecule i has to be charged and self-consistency is obtained by relaxing the density of every molecule of the complex in the electric field of its neighbors. The same procedure has to be repeated for every site in order to get its site energy including electronic polarization effects. Since the molecular densities are relaxed stepwise in individual molecular calculations, linear scaling is achieved.

However, as long as all sites have (nearly) the same environment, like in most of the crystal and liquid crystal studied in this work, the stabilization due to electronic polarization

is only a constant shift to the site energies, which can therefore be omitted. In amorphous materials, on the other hand, the sites have environments with different polarizabilities and their site energies will consequently experience different stabilizations.

5.6. Discussion

In the development of quantum chemical approaches one strives to balance the computational speed and the accuracy required for the specific application. Here, we focused on a fragment orbital approach in combination with a QM/MM algorithm. This has a computational advantage but also one connected with accuracy:

First, the fragmentation allows for an independent calculation of the molecular subsystems. This leads to a linear-scaling ($\mathcal{O}(N)$) computational scheme, where the computer time increases linearly with system size. There is no threshold in system size for the efficiency gain, since no larger systems than the monomers have to be considered, in contrast to other $\mathcal{O}(N)$ schemes, where dimers/trimers or larger buffer regions have to be computed, depending on the particular implementation. This is obviously due to the combination with a force field and the particular constitution of the systems treated here, where no covalent bonds are dissected upon the fragmentation of the system.

Equally important is the aspect of accuracy, which is also enhanced by this approximation. There are two problems to be considered when using an approximate method like DFT or HF approaches with small (minimal) basis sets. One is connected to the basis set issue, and the other is related to the inherent limitations of mean field electronic structure calculations. An efficient way to deal with a minimal basis was shown in section 3.2, where two different basis sets are combined in the block matrix form of the FODFTB Hamiltonian. This approach was proven to yield couplings comparable to triple- ζ DFT calculations in chapter 3 if an appropriate correction factor is applied. The FO scheme also allows to correct the methodology for the SI error, which shows up in the total energy and the coarse-grained matrix elements:

a) SI occurred in the total energy of the original CEID method shown in section 2.3.3 as second order energy term, which depends on the square of the charge density. The self-interaction hinders the dynamics of the charge carrier, as shown in section 5.1. In an uncorrected scheme, SI leads additionally to an over-delocalization of the charge carrier

over the different fragments. The SI-corrected total energy in eq 5.11 has the QM contribution $\langle \Psi | H[\rho_0] | \Psi \rangle$. This term is a simple tight-binding Hamiltonian, which depends only linearly on the electron density. This implies, that this energy contribution exhibits the desired 'straight-line' behavior when computing the charge dependent energies,¹⁷² i.e. it is SI-free.

b) Furthermore, the SI-error is also present in the calculations of the CT parameters i.e. the FO matrix elements:

- On the one hand, HOMO and LUMO orbital energies $\epsilon_m = H_{mm}$ show large deviations from the respective IP and EA values. These errors are not systematic, i.e. a different error occurs for a different chemical species. This does not pose a problem for the homogeneous materials studied in this work, but if different molecular sites are present like in the simulation of donor acceptor interfaces or doped materials, then a correct reproduction of relative energies becomes crucial. A correction scheme has been discussed in detail in ref. 173, where the relative site energies have to be calculated only once at a high level of theory to obtain the reliable reference values. During the Ehrenfest simulation the erroneous site energies can then be corrected by applying a constant shift. In the coarse grained description, it is therefore straightforward to correct collectively several shortcomings of the QM method that lead to wrong relative energies, whereas this is not possible in AO methods.
- On the other hand, the SI (more precisely non-exact exchange correlation) leads to a systematic underestimation of fragment orbital couplings $J = H_{mn}$,¹⁴⁰ as we already discussed in section 3.4. In chapter 3, it has been shown that the deviation is systematic and that the intermolecular DFTB coupling can be corrected with a universal scaling factor of 1.540 for holes¹¹⁵ and 1.795 for electrons.¹¹⁶ The same correction factors for the intermolecular coupling elements are applied throughout this work.

Therefore, the FO scheme not only accelerates the computations significantly, it allows also to improve the accuracy in a simple way by correcting (i) for basis set effects (ii) for SI at the FO total energy level and (iii) constructing a very accurate FO Hamiltonian H_{mn} , where the site energies $\epsilon_m = H_{mm}$ are corrected to reproduce IP/AE differences, and the electronic couplings $H_{mn}(m \neq n)$ are corrected by scaling.^{115,116}

The method includes local and non-local electron-phonon couplings explicitly via coupled equations of motion for the charge carrier and the nuclear degrees of freedom. We

therefore expect that such a bottom-up approach can complement experimental efforts in the understanding of the complex interplay between molecular structure and charge transport characteristics, and that it will become a valuable tool in the rational design of OSC with improved charge transport properties. The method is expected to show its strengths for materials where a crossover of mechanisms is expected, because it does not rely on a specific mechanism. For the description of totally disordered amorphous materials, hopping models are definitely better suited, because simulation time scales have to be very long due to their very low mobilities and the localized character of the charge carrier. Pure crystals, on the other side, can be treated with model approaches parametrized from DFT in most cases, due to their high periodic order. Therefore, they are also not the main application area of this multi-scale approach. Definitely interesting are materials with morphologies that are in between totally ordered and disordered, where the excess charge gets partially localized by fluctuations, which may require a dynamic approach.

Evaluation of Coupled Electron Ion Dynamics on Anthracene and HBC

Reproduced in part with permission from
A. Heck, J. Kranz, T. Kubař and M. Elstner, *J. Chem. Theory
Comput.*, 2015, **11**, 5068–5082.
© 2015 American Chemical Society.

For the evaluation of the method we need a test system that is experimentally well-defined. Uncertainties, like the concentration and depth of trap states that result from impurities and defects, would make a comparison between experiment and simulation very difficult.¹⁵ We will therefore apply CEID to an anthracene single crystal, which can be obtained at very high purity.¹⁷⁴ Experimental data for the anisotropic mobility along different crystallographic axes (see figure 6.1) is available and can be compared with our simulations.¹¹¹

For wide-range applications, single crystals are not very well suited. Their major drawbacks are both the cost and time-effort associated with the growth of sufficiently large single crystals. Promising materials are liquid crystals since they obtain self-assembling and self-healing properties.¹⁷⁵ A second system for the testing of CEID is therefore a liquid crystal of hexabenzocoronene (HBC) with racemic branched (3,7-dimethyloctanyl)

side-chains (HBC-LC).⁷ This molecule features an interesting electronic structure with degenerate frontier orbitals and gives rise to more disordered morphologies, showing 1-dimensional transport.

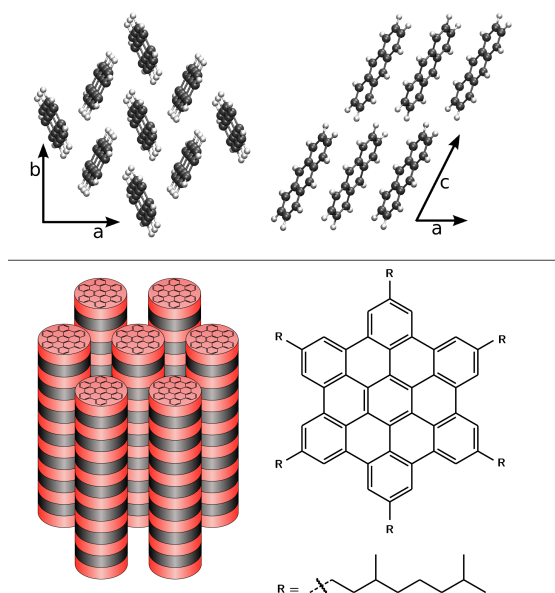


Figure 6.1.: Crystal structure of anthracene (top) and HBC-LC (bottom), where monomers (black/red) stack with a mutual twist of 30° around the columnar axis.

6.1. Simulation Setup

The anthracene single crystal was modeled as a super-cell consisting of $20 \times 20 \times 20$ unit cells, each containing two molecules amounting to a total of 8000 molecules. The initial coordinates of a unit cell were obtained from the herringbone crystal structure known from experiment.¹⁷⁶ The atomic partial charges were fitted according to the RESP protocol.¹⁷⁷ All MD simulations of anthracene in this chapter were performed at a temperature of 300 K.

The HBC liquid crystal was modeled as 9 columns arranged in a hexagonal lattice, each consisting of 110 molecules. The molecules were stacked with a twist of 30° , and a random configuration at the stereogenic centers of the side chains was used. Extracting partial charges according to the RESP protocol was not possible with the antechamber tool-kit,¹⁷⁸ due to technical problems caused by the molecular structure of HBC. For this

reason, Mulliken-charges were derived with DFTB and corrected according to the CM3 method.¹⁷⁹ HBC was simulated in its liquid crystalline phase at 400 K.

In both systems bonded and vdW interactions were modeled with the GAFF⁶⁹ force field parameters. Periodic boundary conditions with particle-mesh Ewald¹⁸⁰ electrostatics were used in all simulations. The temperature and pressure equilibration of the neutral systems was performed with the Berendsen⁷³ scheme and lasted for several nanoseconds in both cases. During the production runs, the Parrinello-Rahman^{76,77} barostat and the Nosé-Hoover^{74,75} thermostat were used to yield a correct canonical ensemble at 1 bar and the respective temperature for each system. The electron ion dynamic is implemented in a local version of Gromacs 4.6,¹⁶⁶ which was also used for the equilibration runs.

6.2. Evaluation of Site Energies

The diagonal elements of the coarse-grained Hamiltonian represent the energy of the system with one electron taken out of the HOMO of the respective molecule. This value would be exactly the vertical IP of that molecule in SI-free DFT. In most practical calculations, however, the orbital energies are not corrected for the SI, which is the reason why the HOMO energy is merely an approximation to the IP. To assess if the difference between IP and HOMO energy will have any effect on our calculations, we compare their time evolution during an MD simulation of an anthracene crystal. The IP is calculated as difference of the self-consistent DFTB2 total energies of the cationic and neutral molecule, and compared to the (non-)self-consistent HOMO energy at the (DFTB1) DFTB2 level. As can be seen in Figure 6.2, there is a large difference between site energies obtained with the different approaches. However, the difference constitutes a constant shift and has therefore no effect on the physics of the system. The energy fluctuations, on the other hand, are the same with all approaches. Note that in systems containing multiple types of molecules, like organic polymer blends or doped materials, special care has to be taken in order to correctly reproduce the relative energies. Approximating site energies with HOMO energies might lead to erroneous energetics in these cases. In a previous work, we presented a detailed comparison between DFT and DFTB2 site energies and their fluctuations along MD trajectories.¹¹⁸

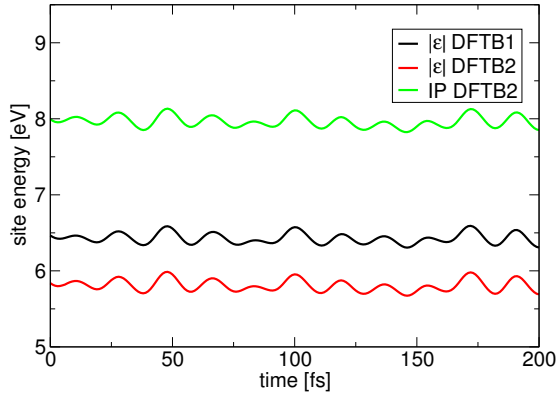


Figure 6.2.: Comparison of HOMO energies obtained without (black) and with self-consistency (red) to the ionization potential (green) of an anthracene molecule in an MD simulation of the crystal. Site energies are shifted but show the same fluctuations.

6.3. Evaluation of Electronic Couplings

The electronic couplings obtained with DFTB were recently benchmarked against high-level ab initio calculations for hole¹¹⁵ and electron¹¹⁶ transfer. Here we further assess if the excellent performance of DFTB is also transferable to the herringbone crystal structure of anthracene by comparing the electronic coupling between nearest neighbors to DFT calculations. As can be seen in Table 6.1, remarkably good agreement with DFT calculations at the B3LYP/TZ2P level is achieved. The highest electronic coupling is found along the b-direction with 48 meV. The coupling between the two molecules in the unit cell is with 21 meV about a factor of two smaller and the coupling along the c-direction is nearly zero. Note that structural fluctuations during the MD simulation will also give rise to non-zero electronic couplings along the c-direction.

Table 6.1.: Electronic coupling between nearest neighbors for the anthracene crystal structure obtained with FODFTB and with FODFT at the B3LYP/TZ2P level

Direction to nearest neighbor	Electronic coupling [meV]	
	DFT	DFTB
Same unit cell	20.8	25.5
b-axis	47.9	41.0
c-axis	0.8	0.0

6.4. Influence of the Environment

To evaluate the influence of the environment, the site energies of a single HBC molecule were calculated at every step along a 100 ps MD simulation, including and excluding the electrostatic potential (ESP) of the environment. The standard deviation of the site energies increases from 61 meV to 81 meV due to the electrostatic interactions with the environment. The time scale of those fluctuations was examined with a power spectrum (Fourier transform of the autocorrelation function).

As can be seen in Figure 6.3, the site energies are mainly modulated by an intramolecular vibration with $\tilde{\nu}=1720\text{ cm}^{-1}$. The environment, on the other hand, gives rise to several site fluctuations with lower frequencies, with dominant contribution below 100 cm^{-1} .

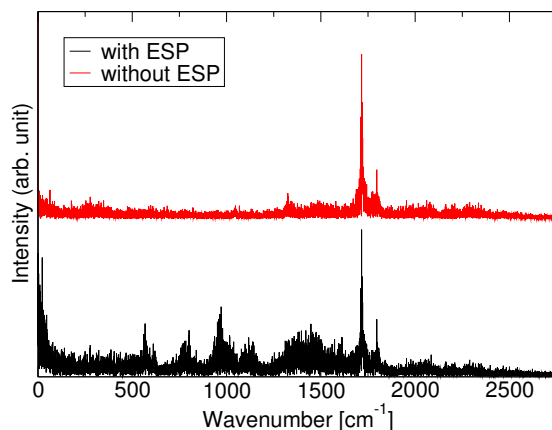


Figure 6.3.: Power spectrum of site energies with and without the electrostatic potential (ESP) of the environment. Intramolecular vibrations give rise to a distinct peak at $\tilde{\nu}=1720\text{ cm}^{-1}$ whereas a broad distribution of slow oscillations are introduced by the environment.

6.5. Electron-Phonon Coupling

An important aspect of our method is the inclusion of electron-phonon coupling. We tested how the molecular relaxation affects the site energies of anthracene and HBC. The energy (eq 5.15) of a single molecule A was minimized in the neutral ($|a_m|^2 = 0 \forall m \in A$) and cationic ($|a_m|^2 = \delta_{m,HOMO}$) state. As expected the relaxation of the structure is accompanied by a decrease of the site energy $|H_{mm}|$ thus effectively lowering the IP. As can be seen in Figure 6.4, the HOMO of anthracene gets shifted by 84 meV. For HBC,

Jahn-Teller distortion can be observed, causing the degenerate site energies split by 86 meV. The relaxation of 60 meV with respect to the neutral HOMO level corresponds to approximately 3/4 of the anthracene value. This is in accordance with the finding that larger aromatic cores exhibit smaller internal reorganization energies.¹⁸¹ These values are slightly smaller than DFT results at the PBE/def2-TZVP level, where a shift of 97 meV is found for anthracene and the splitting and relaxation in HBC are 94 meV and 71 meV, respectively.

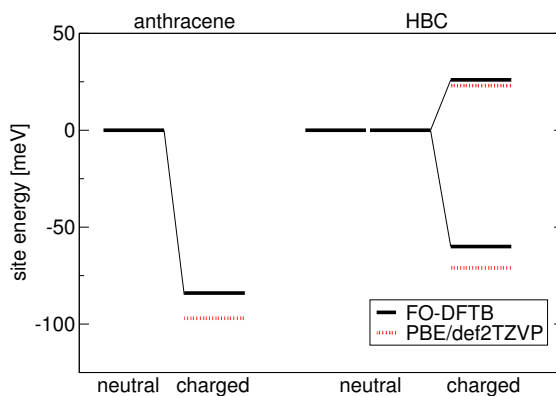


Figure 6.4.: Relaxation of site energies upon charging. Data for anthracene and HBC molecules obtained with the presented multi-scale approach as well as DFT calculations at the PBE/def2-TZVP level.

6.6. Picture of the Charge Transport

The QM zones during the charge transport simulations are shown in figure 6.5 and figure 6.6 for anthracene and HBC, respectively. Transport along each crystallographic axis of anthracene was modeled with 18 sequential molecules in the QM zone. The QM zone of HBC consisted of 30 molecules along a single columnar stack, and a capping scheme was applied to substitute the side-chains.

Each charge dynamics simulation was preceded by a 500 fs simulation where the charge was restricted to a single molecule to allow for the relaxation caused by the excess charge carrier. In the subsequent charge dynamics simulations, the lowest eigenvector of the coarse grained Hamiltonian was used as the starting wave function. The time step of the MD was 1 fs; note that the Runge-Kutta method used to integrate the time-dependent Schrödinger equation performs a large number of shorter time steps internally.

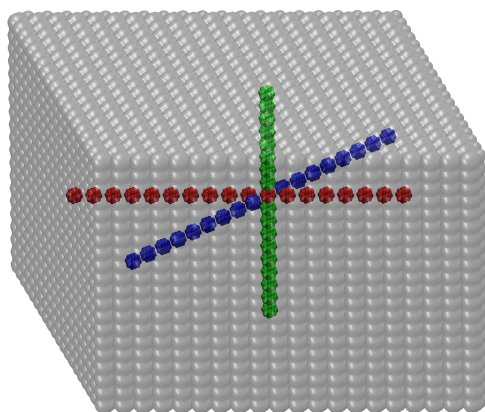


Figure 6.5.: The three QM zones of anthracene along the a (red), b (green), and c (blue) crystallographic axis. 18 sequential molecules from the 8000 molecules in the box were selected.

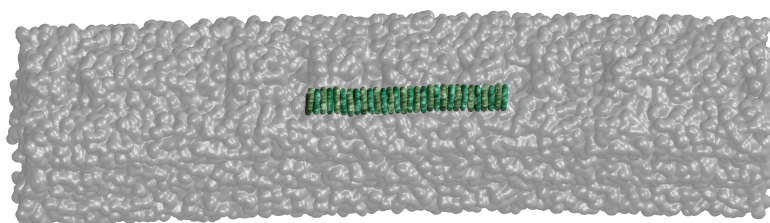


Figure 6.6.: QM zone (green) of HBC. From the 9 columns in the box the QM zone was constructed as 30 sequential molecules in a single column.

Every single simulation of the propagation of a charge carrier evolves differently due to different initial conditions, and averaging over an ensemble of simulations is needed to derive observable quantities. Nevertheless, all these individual simulations share some common features, that will be discussed on two selected trajectories.

First, we take a look at a simulation of anthracene. As can be seen in Figure 6.7 (left), the charge initially forms a polaron that travels over several sites. After about 50 fs, the charge gets scattered on a phonon and the polaron dissociates. Following this event, the localized wave function gets continuously broadened, and it is delocalized over nearly the entire system after less than 500 fs. Notably, the charge carrier gets transferred very fast between neighboring molecules without significant residence time. The occupation of one site lasts only a few tens of femtoseconds. Such an activation-less transfer is expected considering the relatively high electronic coupling and small reorganization energy of anthracene, and it underlines the impact of nuclear vibrations on the dynamic evolution of the charge carrier.

A similar behavior is found for HBC (Figure 6.7 right) with a progressive broadening of the charge carrier wave function. Additionally a splitting of the wave packet can be seen, especially after 300 fs two diverging wave packets can be observed. Such a behavior is a result of the Ehrenfest approach where the system evolves on an ensemble of adiabatic states. In contrast to surface hopping simulations it is not possible to relax to a single adiabatic surface, either where the charge is represented by the left wave packet or by the right wave packet. Similar observations were made with a very similar approach in DNA.¹¹⁰ Application of a mean field approach led to partial delocalization in poly-adenine stacks, whereas restricting the nuclear dynamics to a single adiabatic surface by applying a surface hopping approach led to a localized charge. However, application of a surface-hopping description to our systems is quite involved due to frequent crossings of adiabatic surfaces resulting from the relatively small electronic coupling and energetic disorder of the molecular sites.

6.7. Charge Carrier Mobilities

Next, we calculate hole mobilities and compare them to experimental values. The mobility μ is derived from the diffusive motion of the charge carrier according to the Einstein-Smoluchowski equation

$$\mu = \frac{eD}{k_B T} \quad (6.1)$$

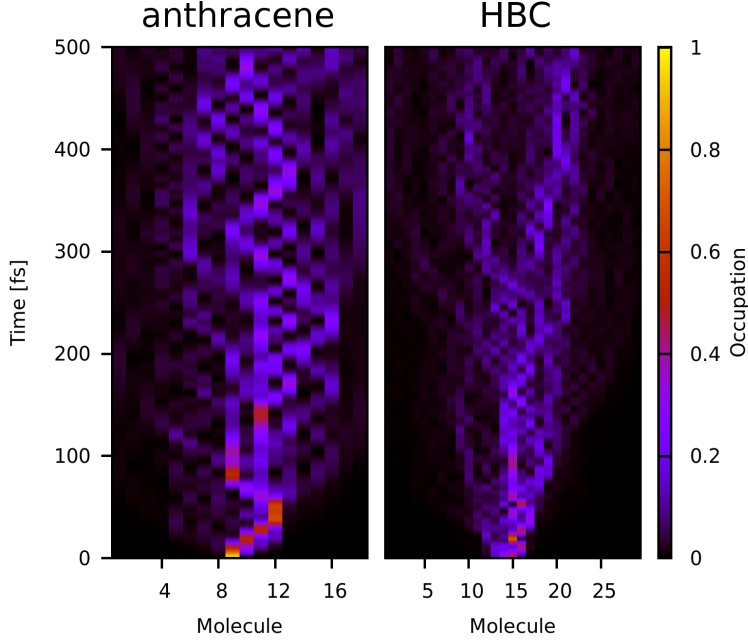


Figure 6.7.: Exemplary time evolution of the hole in anthracene and HBC. The initially localized polaron in anthracene gets scattered at around 50 fs and dissociates until it is completely delocalized at the end of the simulation. For HBC the polaron dissociates after 300 fs into two separate wave packets.

where k_B is the Boltzmann constant, and e denotes the elementary charge. The diffusion constant D is obtained as

$$D = \frac{\langle \Delta x^2(t) \rangle}{nt} \quad (6.2)$$

where $\langle \Delta x^2(t) \rangle$ is the mean squared displacement of the charge at time t and n takes the value of 2, 4 or 6 for 1-, 2- or 3-dimensional systems respectively. The mean squared displacement is defined as

$$\langle \Delta x^2(t) \rangle = \sum_A (x_A(t) - x_0)^2 p_A(t) \quad (6.3)$$

with $x_A(t)$ denoting the center of mass of molecule A , and x_0 is the initial position of charge carrier at $t = 0$. $p_A(t)$ is the occupation of molecule A at time t given as $p_A(t) = \sum_{m \in A} |a_m|^2$, where a_m is the wave function coefficient in the FO basis. To capture the influence of different starting conditions, the mean square displacement is averaged over 100 simulations. The mobility was obtained from a linear fit of $\langle \Delta x^2(t) \rangle$ versus time during the first 100 fs.

Table 6.2.: Hole mobilities for anthracene at 300 K along crystallographic axes as well as for liquid crystalline HBC at 400 K along the columnar stacking direction. HBC(1) and HBC(2) denote the different approaches to intramolecular orbital transitions (see section 5.3).

System	Mobility [cm^2/Vs]		Reference
	calculated	experimental	
Anthracene (a)	0.80	1.14 (TOF)	111
Anthracene (b)	1.94	2.93 (TOF)	111
Anthracene (c)	0.48	1.05 [†] (TOF)	111
HBC(1)	1.16	~ 0.4 (PR-TRMC)	182
HBC(2)	1.55	~ 0.4 (PR-TRMC)	182

[†] The crystallographic c direction used in our simulations differs by about 35° from the orthogonalized coordinate system $a \perp b \perp c'$ that was used in the experiment.

As can be seen from Table 6.2, an excellent agreement with time-of-flight (TOF) experiments is achieved for anthracene. The crystallographic b direction has been correctly identified as the best transport direction, with a mobility of $1.94 \text{ cm}^2/\text{Vs}$. The transport along the a and c directions is similarly fast but slower than along the b direction. The calculated mobilities are within a factor of two of the experimental values.

The calculated mobilities for HBC deviate slightly more from the experimental values obtained with the pulse-radiolysis time-resolved microwave conductivity technique (PR-TRMC), but are still within the same order of magnitude. The different treatment of transitions between degenerate orbitals discussed in section 5.3, leads to a notable difference in the calculated mobilities, however, both values are still reasonable compared to experimental results. Without non-adiabatic coupling between the degenerate HOMOs (method 2), the charge can pass the crossing events of the HOMOs and continue in the excited state. This excitation counteracts the energetic relaxation due to polaron formation and aids in achieving resonance with non-relaxed (unoccupied) neighboring sites. Therefore, a higher mobility can be observed within this approach. The mobility is overestimated in HBC in contrast to anthracene. However, these values can be seen as upper boundary, since impurities, defects and losses at the contacts are not taken into account in our simulations. A further explanation for the underestimated mobility in anthracene in contrast to the overestimation in HBC is that our anthracene simulations are artificially restricted to one dimension whereas the charge carrier can circumvent mobility bottlenecks introduced by thermal vibrations in actual 3-dimensional system. Note that the charge transport through HBC, on the other hand, is truly 1-dimensional.

6.8. Charge Transport Mechanism

The time evolution of the wave function following Ehrenfest dynamics shows a spreading similar to that of a 1-dimensional wave packet propagated with the Schrödinger equation known from quantum mechanics text books. The spreading is an ensemble property, and therefore does not directly inform about the localization/delocalization of the charge carrier. A measure of intrinsic delocalization can be obtained from the delocalization of the adiabatic states.

$$|\varphi_i\rangle = \sum_m c_m^i |\phi_m\rangle \quad (6.4)$$

Therefore, we calculated the adiabatic states for HBC and the anthracene *b*-direction along the 100 simulations by diagonalizing the fragment orbital Hamiltonian at every step. The number of molecules over which one adiabatic state *i* is delocalized was defined as $N_{del}^i = \frac{1}{\sum_A (p_A^i)^2}$ where p_A^i is the charge on molecule *A* in state *i* given as $p_A^i = \sum_{m \in A} |c_m^i|^2$. The delocalization fluctuates strongly, and the wave function was occasionally delocalized over up to 20 HBC molecules or 10 anthracene molecules. However, these are quite rare events, and the delocalization is significantly smaller in average. The averaged delocalization for a certain energy interval as well as the density of states (DOS) are shown in Figure 6.8. As can be seen from these figures, the DOS can be described very well by a Gaussian distribution with a standard deviation of 0.11 eV and 0.12 eV for HBC and anthracene, respectively. The states at the tails of the DOS are significantly stronger localized compared to the states near the center. However, even the localized states at the tails are still not restricted to a single molecule. Note that for anthracene, in contrast to HBC, the DOS and delocalization do not represent bulk material properties since we are restricting our simulations to 1-dimensional QM zones. Rather are these quantities meant to facilitate the understanding of our charge-dynamics simulations.

For the ideal crystal or stack (no static and dynamic disorder), a delocalization over the entire system would occur, while dynamic disorder leads to localization of the states to 2-4 sites for the systems at finite temperatures. Since the adiabatic states, especially those at the tail of the DOS, are quite localized compared to the wave function that is observed in our Ehrenfest simulations, we can already conclude that the transport is non-adiabatic and occurs via occupation of higher adiabatic states. This is further quantified in Figure 6.9 where we show the percentage of adiabatic states that are occupied on average during our simulations. The occupation $P_i = |b_i|^2$ of an adiabatic surface is

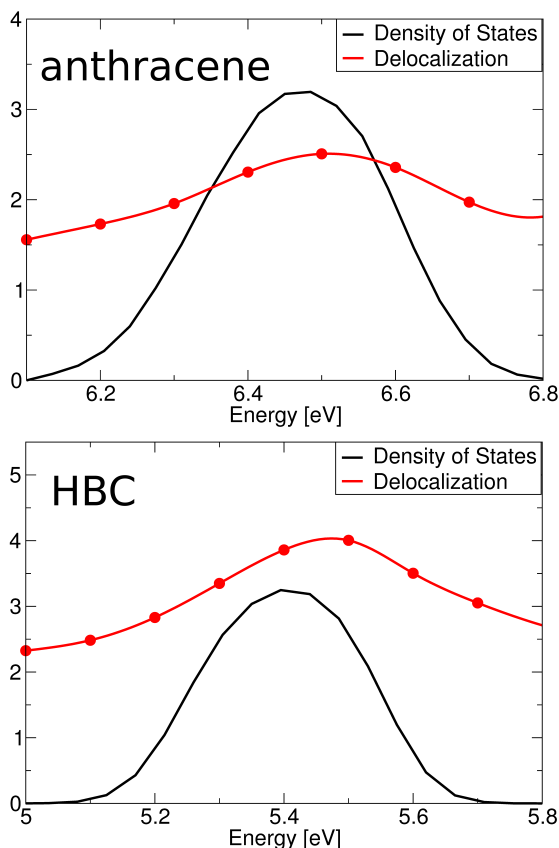


Figure 6.8.: Density of states and the number of molecules over which these states are delocalized. Shown values are averages over each simulation of the anthracene b-direction.

obtained by projecting the wave function on the adiabatic states

$$\Psi = \sum_m a_m |\phi_m\rangle = \sum_{im} |\varphi_i\rangle \langle \varphi_i | \phi_m \rangle a_m = \sum_i b_i |\varphi_i\rangle \quad (6.5)$$

The ratio of occupied adiabatic states is defined as $N_{adi} = \frac{1}{\sum_i P_i^2} \times \frac{1}{N_{tot}}$ where N_{tot} is the total number of adiabatic surfaces. Note that only the highest adiabatic states, resulting from linear combinations of the HOMOs, are present in our calculations. At the end of our simulations, about two thirds of the adiabatic states are occupied in anthracene, and nearly all states of HBC. Surprisingly, the occupation of additional adiabatic states sets in significantly more quickly in HBC compared to anthracene. This might in part be explained by the smaller nuclear relaxation of HBC (see Figure 6.4) which leads to a smaller stabilization of the adiabatic ground state at the starting conditions, facilitating the occupation of higher states. The faster transition from a single adiabatic state into an

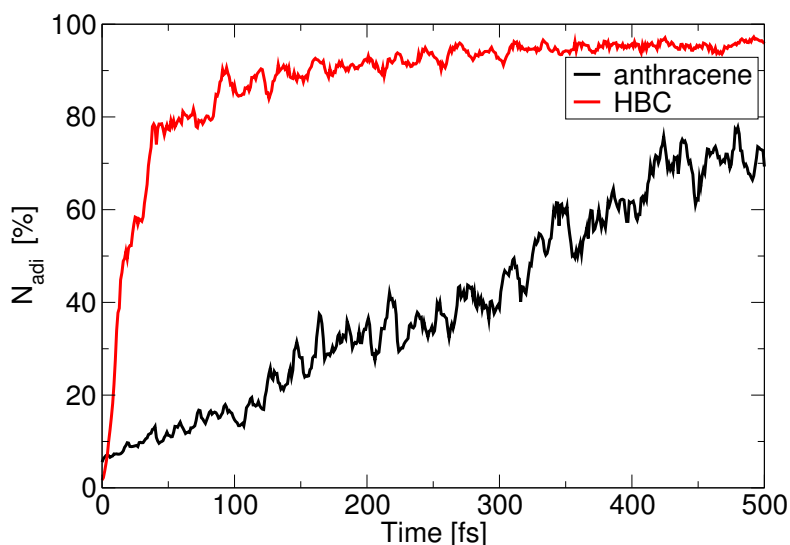


Figure 6.9.: Percentage of adiabatic states that are occupied, averaged over 100 simulations. The simulation of the anthracene *b*-direction and HBC(1) are shown.

ensemble in HBC compared to anthracene gives rise to a stronger impact of the mean-field error, which also leads to an overestimation of the mobility in this case.

6.9. Relevance of Lower-lying Orbitals

As mentioned before, the basis set of the FO Hamiltonian can be expanded if desired for a more accurate description of the system. For anthracene, this has only negligible influence on the mobility since the HOMO-1 lies about 1 eV below the HOMO. Our calculations showed an increase of mobility by $\sim 10\%$, which is within the error of our method. HBC, on the other hand, features a much more involved electronic structure. Besides the degenerate HOMO orbitals, there is also a relatively high-lying HOMO-2.

To evaluate the energy difference between HOMOs and HOMO-2, the SAOP method^{183,184} was applied as a reference, since it yields accurate orbital energies due to the correct asymptotic description of Coulomb interactions. The reference calculation on the structure optimized at the PW91/TZ2P level yields 0.271 eV for the energy difference, which is reasonably well reproduced by the DFTB1 value of 0.390 eV. Note that Hartree-Fock calculations, on the other hand, overestimate the energy difference of these orbitals tremendously with 0.685 eV. Further orbitals are well separated by more than 1 eV and therefore omitted safely.

A further factor that increases the importance of the HOMO-2 is the staggered stacking of molecules along the liquid crystalline columns, leading to a minimal electronic coupling* between the degenerate HOMOs of neighbouring molecules, whereas the coupling between the HOMO-2 shows a maximum (see Figure 6.10).

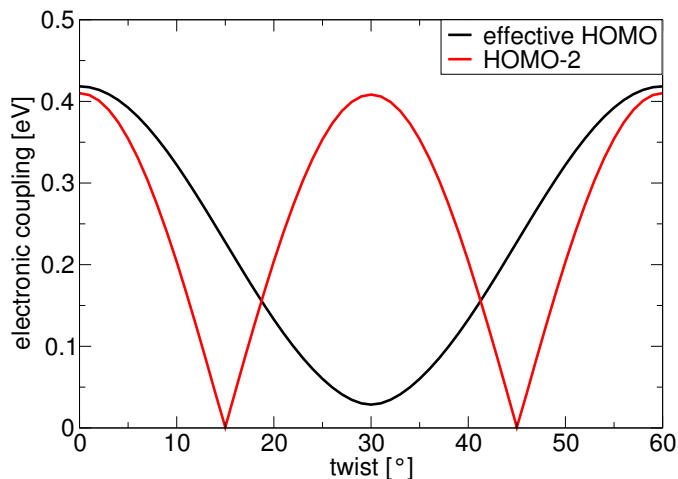


Figure 6.10.: Dependence of the electronic couplings on the relative rotation of two HBC molecules around the columnar axis.

The cumulative effect of these large couplings leads to the surprising behaviour that the HOMO of the stack is not a linear combination of the HOMOs of the individual molecules but rather of their HOMO-2, as can be seen in Figure 6.11. Therefore, the HOMO-2 plays the dominant role in the propagation of the charge carrier and its inclusion increases the mobility tremendously, from 1.16 to 7.05 cm²/Vs, whereas inclusion of the HOMO-3 has no further impact on the mobility (7.15 cm²/Vs). Note that the inclusion of the lower-lying HOMO-2 increases the deviation of the calculated mobility from the experimental value. However, experimental preparation conditions can have a much larger influence on the device performance and affect the mobility by several orders of magnitude.^{185,186} Therefore, the importance of the HOMO-2 can not be discarded solely by comparison of the calculated mobility with the experiment. Furthermore, since our method overestimates the energetic difference between the HOMOs and the HOMO-2 compared to the reference calculation, we are confident that the HOMO-2 actually plays an important role.

*Note that there are four different coupling elements between degenerate orbitals on two molecules and an effective coupling can be derived as $H_{AB}^{eff} = \sqrt{\frac{1}{2} \sum_{m \in A, n \in B} |H_{mn}|^2}$.

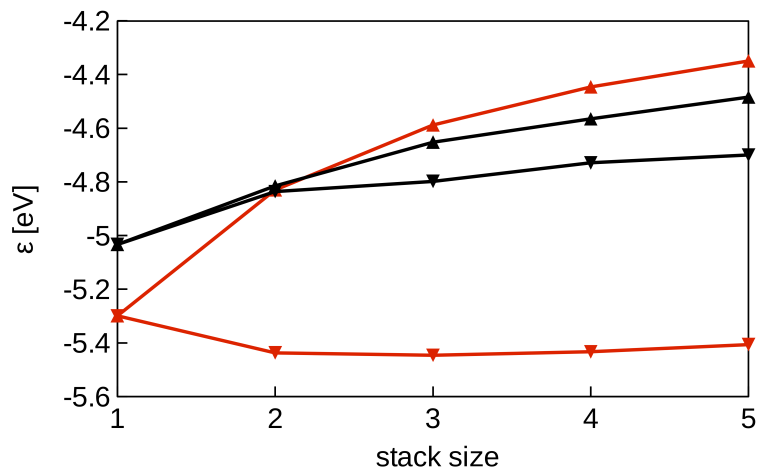


Figure 6.11.: Energies of molecular orbitals for an HBC stack of different size calculated at the PBE/def2-TZVP level. Only the energetically highest (▲) and lowest (▼) linear combination of HOMOs (black) and HOMO-2 (red) of the single molecules are shown.

The dominant influence of lower-lying FOs is an uncommon mechanism and usually not considered when the optimization of mobilities is discussed. The prevalent guiding principle is still maximization of the intermolecular HOMO coupling as well as minimization of the energetic disorder and reorganization energy. Our calculations suggest that also the maximization of the coupling between lower-lying FOs and the minimization of their stabilization with respect to the HOMO level should be considered as an additional route. Hopping calculations, as previously performed for HBC,^{33,34,187} usually consider only the (degenerate) HOMOs or use constrained DFT to calculate electronic couplings. This way the influence of lower lying orbitals can not be captured. Ehrenfest simulations in a AO basis, on the other hand, incorporate the influence of lower molecular orbitals only implicitly. Further analysis of the simulated charge dynamics is necessary to make the explicit connection between the transport through the bulk material, described in an AO basis, and the MO structure of the individual molecules. The FO method presented here is therefore a valuable tool for guiding the design of new molecular semiconductors by drawing a connection between the electronic structure of the synthesized monomer and its performance in the bulk material.

6.10. Discussion

In this chapter we applied the CEID method, presented in chapter 5, to anthracene and HBC-LC. Essential features of this method are the combination of a linear-scaling fragment orbital approach with classical molecular dynamics, which allows to access extensive length and time scales that are necessary for a realistic description of bulk materials. Furthermore local and non-local electron-phonon couplings are considered and SI errors were corrected for.

As a result, CEID can reproduce the absolute value as well as anisotropy of hole mobility for the studied systems. Besides reproduction of experimental measurements, a detailed understanding of the charge transport mechanism is also accessible. The adiabatic eigenstates of the system are localized on few molecules at all times, due to thermal disorder. We consider the estimates of the localization to be reliable, since the DFT delocalization error was corrected for. Even though the adiabatic states are delocalized over only a few molecules, no stable polaron was found for both materials at the simulated temperature, a finding similar to recent reports for other systems.^{29,188} The 'non-existence' of the small polaron for materials with high mobility has been discussed in detail in ref. 43. Therefore, the success of hopping models for such materials^{33,34,187,189} may be based on fortunate cancellation of errors. Furthermore, we have observed that it is insufficient to consider only the two degenerate HOMOs of HBC in the hole dynamics, as often assumed in hopping models, because lower lying orbitals can have significant influence on the mobility.

Despite its strengths, the proposed approach also has several shortcomings, which have been characterized well:

1) Quantum back reaction and mean field error:

The presence of the excess charge introduces a distortion in the nuclear system (quantum back reaction), which in turn changes the electronic dynamics. In the Ehrenfest description, the charge is not restricted to a single adiabatic surface, because the propagation of the time dependent Schrödinger equation allows to occupy an ensemble of adiabatic states. This way, however, the potential energy of the system is also an average over all (adiabatic) states, weighted by their occupation. The nuclear dynamics of the system then follows this mean potential energy surface (PES), whereas each member of the ensemble should in principle relax according

to its respective adiabatic PES, leading to diverging trajectories. Therefore, relaxation of the molecular structure will be progressively underestimated with the increasing degree of delocalization. This drawback is significant e.g. whenever two adiabatic states with localized charge diverge in a polar environment, which has been discussed in detail for CT in DNA.¹⁰⁹ The different PESs, arising from each adiabatic state will differ significantly, and propagating the atoms on an averaged PES will therefore lead to a qualitatively wrong dynamics. In the studied OCS, on the other hand, the adiabatic states are already spread out over several sites, and the local relaxation (reorganization energy λ_i) is very small. The relaxation of site m can be written as a function of charge as $E_{rel}^m = \frac{1}{2}\lambda_i Q_m^2$,¹⁰⁹ i.e. it becomes negligible for a delocalization over 4 sites compared to the thermal site energy fluctuations (assuming the reorganization energies $\lambda_i \approx 0.1eV$). Therefore, the Ehrenfest mean-field error probably does not contribute much to the error in the mobilities.

2) Non-Boltzmann population in Ehrenfest simulations

On one hand we have the problem, that an entire ensemble is described with a single Ehrenfest trajectory. On the other hand we have seen that the adiabatic state populations, reached during our Ehrenfest simulations, do not obey a Boltzmann distribution. Note that this behavior is an intrinsic problem of the Ehrenfest method and not resulting from the approximations of our methodology. Similar spreading over all adiabatic states was also found in ab initio Ehrenfest dynamics.¹⁹⁰ By restricting the transitions from lower to higher surfaces with a Boltzmann factor, however, the authors were able to suppress this behavior and achieve dynamics similar to a surface hopping simulation.

One could ask, whether the artificial population of thermally non-accessible states may affect the calculated mobilities. In the case of anthracene, all adiabatic states are built from the same fragment orbital, due to the large energetic separation of the HOMO from the remaining molecular orbitals. Therefore, we find similar electronic couplings between the sites no matter which adiabatic state is occupied. Therefore, we do not expect the CT characteristic to be affected here. In the case of HBC, on the other hand, adiabatic states can be built either from degenerate HOMOs or lower-lying HOMO-2, whereby the electronic couplings between the latter ones are significantly stronger than between the former ones. Therefore, one can expect that allowing the occupation of thermally forbidden states affects the

CT depending on the contribution of HOMOs and HOMO-2 to the respective state.

To summarize, for the two materials with sizeable mobilities, no polaronic effects were found, and the charge carriers are substantially delocalized. This, however, implies that the quantum back reaction is not a critical issue, and it has been neglected from the beginning e.g. in ref. 190. We have argued that Ehrenfest dynamics, which has several flaws that should be considered seriously, is applicable in this context. Since polaronic effects are small, the factors governing CT in these materials are the values and the fluctuations of the CT parameters, i.e. the site energies ϵ_m and the couplings H_{mn} . As has been shown before, the average couplings for a certain material can be very small, but the fluctuations can be such that transfer is governed by non-equilibrium structures.⁴² This highlights the importance of bottom-up modeling, since the dependence of H_{mn} on the molecular structure is quite complex and not easy to implement into simple models. Therefore, atomistic simulations may be indispensable to understand material characteristics.

Temperature Dependence of Mobilities

The correct reproduction of the temperature dependence of the mobility is a formidable challenge, because completely opposite trends can be observed in different materials. In single crystals the temperature usually decreases with increasing temperature following a power-law

$$\mu(T) = C \cdot T^{-n} \quad (7.1)$$

with an exponent typically in the range between 0.5 and 3. This temperature dependence is typical for band transport and originates from increased scattering of the charge carrier at higher temperatures.

On the contrary, in disordered materials the mobility usually increases with temperature, which is typical for hopping transport. In these materials the charge is trapped in a localized state and needs thermal activation for a transfer to a neighboring site. The trapping can originate from (1) a disordered morphology, giving rise to a broad distribution of site energies, (2) guest molecules (i.e. impurities) with lower site energies acting as trapping centers, (3) or due to self-trapping, if the response of the nuclei to the charge causes a sufficiently large relaxation ($\lambda \gg H_{ab}$).

There are two widely used rate equations that are applied to disordered systems. Assuming a Gaussian disorder of site energies and applying Miller-Abrahams rates for the charge transfer, the temperature dependent mobility can be obtained as

$$\mu(T) = \mu_{\infty} \exp \left\{ - \left(\frac{T_0}{T} \right)^2 \right\} \quad (7.2)$$

The second common rate equation was derived by Marcus, and features a more involved temperature dependence with temperature intervals where the rate may also decrease with increasing temperature. When applying Marcus rates to derive mobilities, its temperature dependence therefore strongly depends on the system parameters entering the equation and no universal trend can be given. Nevertheless, the temperature dependence of the mobility can be used as indication of the underlying physics in these materials.

In section 6.7 we have already obtained room temperature mobilities in very good agreement with the experiment. We will now try to validate that our CEID simulations also model the correct physics that are necessary to reproduce the correct temperature dependence of the mobility. In section 7.2 and 7.3 we will therefore compare the temperature dependent mobility of the anthracene single crystal to amorphous α -NPD; systems for which significantly different transport mechanisms are expected. Furthermore, we will extend our study to polymers and liquid-crystals whose morphologies fall in between completely ordered and disordered and try to rationalize the experimental findings with help of our simulations. Finally, we will investigate how modifications in the morphology may lead to a better transport properties. The Lewis structures of the respective molecules are shown in figure 7.1.

7.1. General Simulation Setup

Bonded and vdW interactions were modeled in all systems with the GAFF⁶⁹ force field parameters if not stated otherwise. Periodic boundary conditions with particle-mesh Ewald¹⁸⁰ electrostatics were used in equilibration runs and in the CEID simulations. The temperature and pressure equilibration of the neutral systems was performed with the Berendsen scheme⁷³ and lasted for several nanoseconds in all cases. During the CEID runs, the Parrinello-Rahman barostat and the Nosé-Hoover thermostat were used to yield a correct canonical ensemble at 1 bar and the respective temperature for each system. The global time step of the MD was 1 fs, but note that the Runge-Kutta method used to integrate the time-dependent Schrödinger equation performs a large number of shorter time steps internally to achieve a sufficiently accurate integration.

The mobility for each temperature was obtained as described in section 6.7. Averages were again taken over 100 runs. The feasible duration of the runs was limited by the time it takes for the excess charge to reach the edge of the quantum region and therefore depends on the mobility of the material and size of the QM zone.

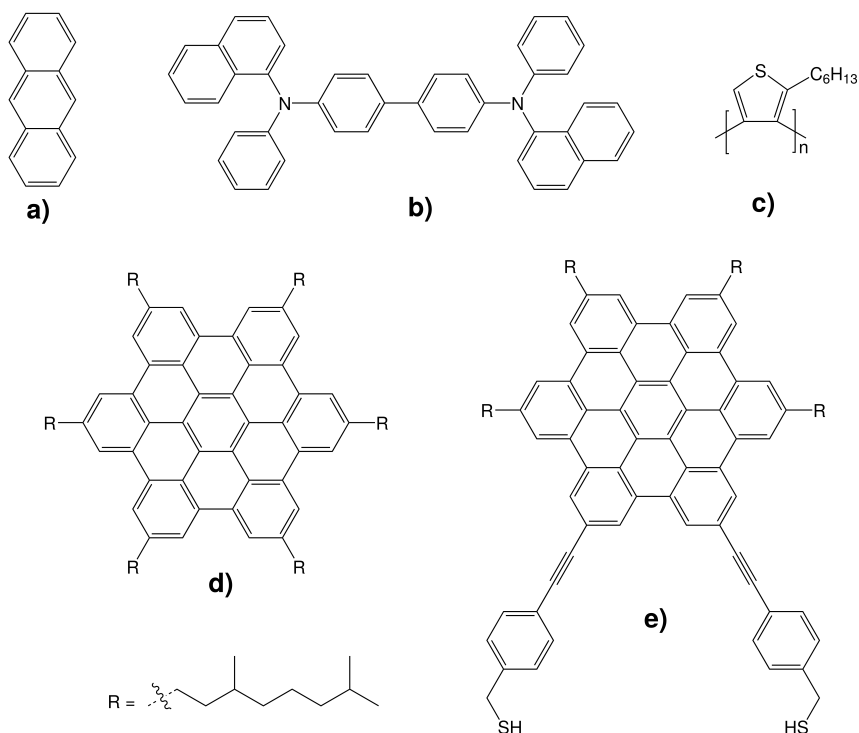


Figure 7.1.: Molecular building blocks of the systems studied in this chapter. a) anthracene b) α -NPD c) P3HT d) HBC-LC e) HBC-SAM.

7.2. Study of an Ordered Material: Anthracene

As a typical ordered system we again studied a single crystal of anthracene. The same simulation setup as in section 6.1 was used with the QM zone shown in section 6.6, with a single HOMO per molecule entering the CEID calculations. Simulations were performed for temperatures in the range of 150 to 400 K and the duration of each individual CEID run was 500 fs.

7.2.1. Results and Discussion

As can be seen from figure 7.2, the simulated hole mobilities range from 0.3 to 5.8 cm^2/Vs and decrease with temperature. The temperature dependence is well described by a power-law and least square fitting of $\mu = C \cdot T^{-n}$ to the simulated data yields exponents n between 1 and 1.5, depending on the crystallographic axis with coefficient of determination for the fits of $r^2 > 0.988$. Such a thermal dependence of the mobility

is characteristic of large-polaron, band-like behavior. Since anthracene is an ultra-pure organic crystal this is the behavior one would expect.

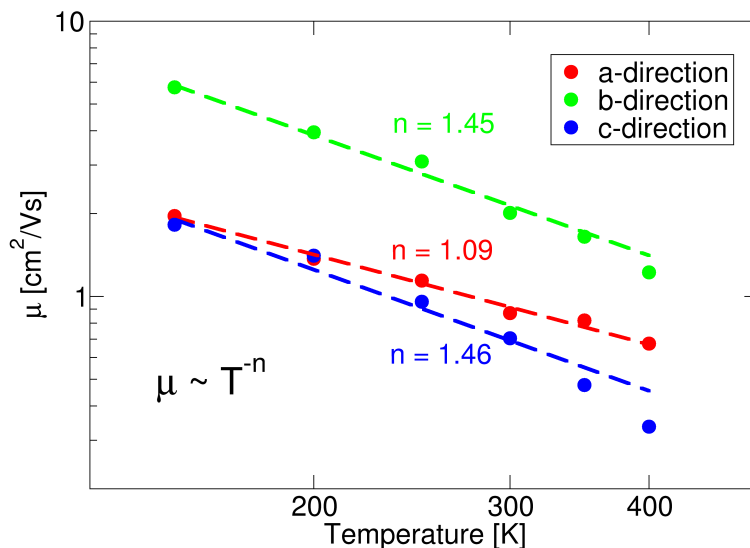


Figure 7.2.: Hole mobilities in anthracene at different temperatures in direction of the three crystallographic axes as shown in figure 6.5 and fits of $\mu = C \cdot T^{-n}$ to the simulated data.

The simulated mobilities are in very good agreement with the experiment as can be seen in table 7.1. Compared to TOF measurements on highly purified single crystals, the simulated mobilities deviate by less than a factor of 2. The same holds true for the exponent in the power law, which describes the temperature dependence of the mobility. The slightly underestimated mobility in anthracene could be caused by the artificial restriction of the QM zone to one dimension, whereas in an actual 3-dimensional system the charge carrier could circumvent bottlenecks introduced by thermal fluctuations in the CT parameters.

7.3. Study of a Disordered Material: α -NPD

As a typical disordered material, we studied the amorphous phase of N,N'-bis(1-naphthyl)-N,N'-diphenyl-1,1'-biphenyl-4,4'-diamine (α -NPD, also called NPB), which is widely used

Table 7.1.: Comparison of the simulated hole mobilities of anthracene with experimental values obtained from TOF measurements.¹¹¹ Mobilities are only shown for three selected temperatures at which the mobility tensor was given in ref. 111 together with the exponent n after fit of $\mu = C \cdot T^{-n}$ to all simulated and experimental data, respectively.

	a-direction		b-direction		c-direction [†]	
	sim.	exp.	sim.	exp.	sim.	exp.
200 K	1.37	2.22	3.95	5.05	1.41	1.98
250 K	1.14	1.51	3.09	3.74	0.96	1.20
300 K	0.87	1.14	2.01	2.93	0.70	0.85
n	1.09	1.50	1.45	1.34	1.46	2.38

[†] An orthogonalized coordinate system $a \perp b \perp c'$ was used in the experiment, where c' differs by about 35° from the crystallographic c direction used in our simulations.

in OLEDs as a hole-injection layer,¹⁹¹ hole-transport layer^{192,193} or electron-blocking layer.¹⁹⁴

7.3.1. Simulation Setup

Hole transport in the amorphous phase of α -NPD was modeled at temperatures from 150 to 400 K. Force field parameters were provided by Denis Danilov and consist of GAFF⁶⁹ parameters for bonded interactions with partial charges from PM6 calculations. For the generation of the amorphous starting structures an annealing procedure was performed where a simulation box of 300 molecules was first melted at 700 K and then successively cooled down. The cooling steps consisted of a temperature reduction of 50 K over 1 ns, followed by a 1 ns simulation at constant temperature, from which the starting structures were extracted.

A subset of 27 molecules was included in the QM region shown in figure 7.3. To picture the energetic disorder realistically and capture the rate-limiting detrapping steps, the HOMO energies of all 300 molecules were scanned at the start of each simulation. The initial position of the hole was then assigned to the molecule with the highest HOMO energy (lowest site energy) and the QM zone was constructed around this molecule with the closest 26 neighbors. Because of the low mobility of α -NPD, the individual charge transport runs could be performed for 10 ps before the charge reached the QM/MM boundary.

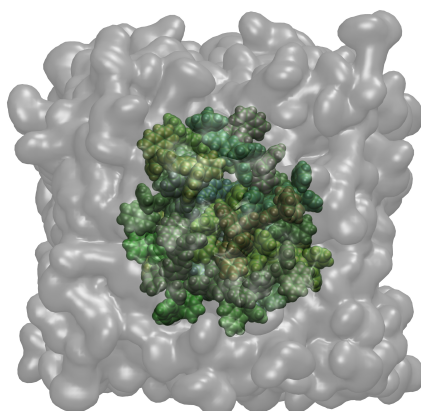
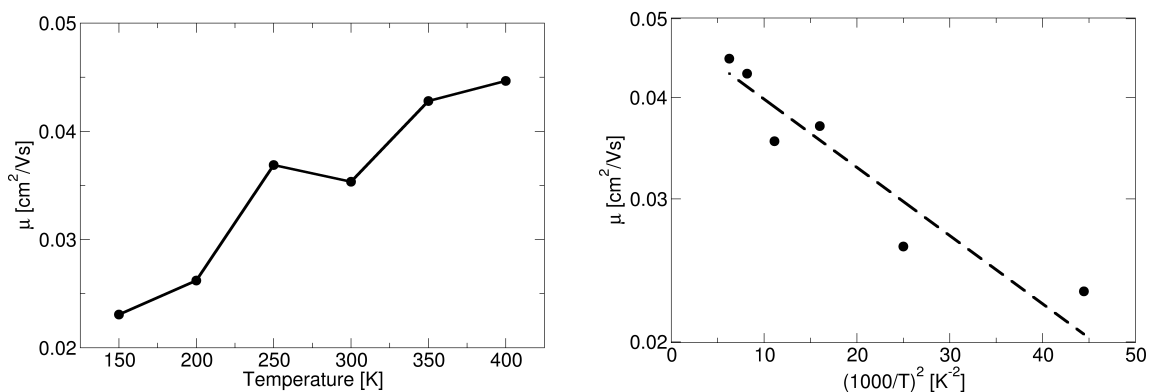


Figure 7.3.: QM zone of α -NPD (green). From the 300 molecule in the box the QM zone was constructed as cluster of 27 molecules around the single molecule with the lowest IP.

7.3.2. Results and Discussion

As can be seen from figure 7.4a, a completely different temperature dependence compared to the previous system is found. The mobility *increases* with temperature, which indicates activated hopping, and ranges from 2.3×10^{-2} to 4.5×10^{-2} cm^2/Vs . Such a temperature dependence can be expected considering the strong disorder in the amorphous material. The temperature dependence can be explained by the Gaussian disorder model and is fitted quite well by $\mu = \mu_\infty \cdot \exp[-(\frac{2\sigma}{3kT})^2]$ with $r^2 > 0.892$ (see 7.4b). The fit yields a high-temperature limit of the mobility of $\mu_\infty = 4.8 \times 10^{-2}$ cm^2/Vs .

TOF measurements at room temperature on vacuum vapor deposited thin films yield hole mobilities of $3 - 4 \times 10^{-4}$ cm^2/Vs ,¹⁹⁵⁻¹⁹⁷ and similar results are also obtained under the same preparation conditions but applying admittance spectroscopy,¹⁹⁸ whereas TFT measurements yielded mobilities one order of magnitude lower.¹⁹⁷ Therefore, compared to experimental values our calculated room temperature mobility is about two orders of magnitude too high. However, the room temperature mobility (μ_{RT}) is strongly affected by impurities and defects inside the material and is therefore not a very good estimate for the intrinsic transport properties of an organic material. For amorphous materials such as α -NPD, the purification is more difficult than for crystalline materials and the reduction of μ_{RT} due to defects and impurities can be expected to be a dominant factor.



(a) Absolute value of the mobility for different temperatures. (b) Fit of $\mu = \mu_\infty \cdot \exp[-(\frac{2\sigma}{3kT})^2]$ to the simulated mobilities of α -NPD.

Figure 7.4.: Simulated mobilities of α -NPD for different temperatures in the range of 150 to 400 K.

It was argued that the high-temperature limit of the mobility (μ_∞) is better suited for the description of the intrinsic mobility, because at high temperatures the temperature activated detrapping of the excess charge ceases to be the limiting factor.¹⁹⁹ This was illustrated in ref. 199 for α -NPD, doped with various compounds. Nearly the same μ_∞ was found for all dopants, whereas μ_{RT} differed by more than one order of magnitude.

Our simulated high-temperature limit of the mobility $\mu_\infty = 4.8 \times 10^{-2}$ is very similar to the experimental value of $\mu_\infty = 1.7 \times 10^{-2} \text{ cm}^2/\text{Vs}$. The weaker increase of mobility with temperature points to smaller energetic disorder in our simulations compared to experiment. Reasons for this behavior could be the lack of impurities in our simulations or the simulation of a too ordered morphology. Latter may be caused by non-optimal force field parameters or by different routes to the amorphous morphology (evaporation in the experiment and freezing a melt in the simulation).

7.4. Study of a Semi-Ordered Material: P3HT

Many conjugated polymers exhibit complex morphologies, where crystalline domains are embedded in an amorphous matrix.²⁰⁰ The simulation of such an involved structure is, however, beyond the scope of this work. Therefore, we focus on a single aspect of CT in polymers, namely the interchain transport in crystalline domains. The model system we are studying is poly(3-hexylthiophen) (P3HT), which is widely used in bulk

heterojunction solar cells as hole transporting layer together with phenyl-C61-butyric acid methyl ester (PCBM) as electron transporting layer.

7.4.1. Simulation Setup

Inter-strand hole movement in an ordered section of regioregular P3HT has been considered at different temperatures ranging from 150 to 350 K. The simulation box consisted of 400 parallel strands, each built of 20 monomers. Force field parameters were taken from ref. 201, where OPLS-AA^{70,71} force field parameters were used with partial charges from ref. 202 and dihedral parameters were fitted to a B3LYP/6-311+g(d,p) potential energy scan. The initial structure corresponds to morphology I' as described in ref. 201. A single fragment in the CEID calculations was formed of 10 sequential monomers on a single strand, and for each fragment the 10 highest occupied orbitals were taken to form the basis for the hole wavefunction. This ensures that the whole length of the fragment may be covered with, potentially localized, states. The remainders of the strands were cut off from the QM zones and capped by hydrogen atoms. The total quantum region consisted of 20 sequentially π -stacked fragments (see figure 7.5).

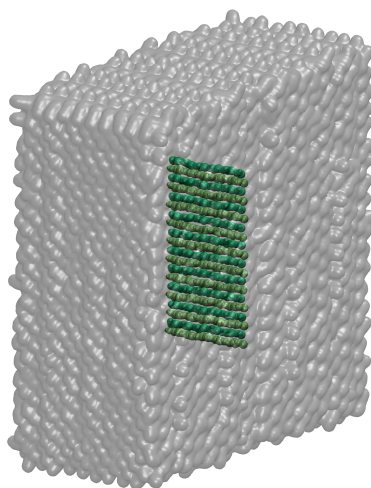


Figure 7.5.: QM zone (green) of P3HT. The central 10 monomers of 20 strands were selected from the 400 strands in the box.

7.4.2. Results and Discussion

As can be seen from figure 7.6, we find mobilities in the range of 1.5 to 4 cm²/Vs, which decrease with increasing temperature. Again the mobility follows a power-law ($\mu \sim T^{-n}$) with an exponent of $n = 1.05$, indicating large-polaron, band-like behavior. The coefficient of determination of the fit is $r^2 = 0.981$.

In carefully prepared FETs mobilities as high as 0.1 cm²/Vs are obtainable,²⁰³ which is one order of magnitude smaller than our simulated mobility. Direct comparison of these values to experiment is difficult, however, because, we face again uncertainties regarding the purity of the material and its influence on the mobility as discussed already in section 7.3.2. This difficulty is illustrated by the fact that the field-effect transistor (FET) mobility of regioregular P3HT can change by three orders of magnitude depending on the preparation conditions and applied solvent.²⁰⁴ Additionally, the morphology of P3HT is dependent on its molecular weight and can change after annealing.²⁰⁵ While we simulate a single crystalline domain, standard experiments like TOF or PR-TRMC probe polycrystalline materials with grain boundaries between the crystallites, which reduce the observed direct current (DC) mobility. The formation of grain boundaries appears to be strongly dependent on the molecular weight of the polymer with low molecular weight P3HT layers being more crystalline than their high molecular weight counterpart.⁹ It was further proposed that long polymer chains might bridge crystallites in high molecular weight P3HT, leading to higher mobilities.⁸

One possibility to get rid of grain boundaries and measure the pure interchain transport in crystalline domains of P3HT is the study of Nanofibers. In these fibers the P3HT chains align perpendicular to the fiber direction and stack on top of each other.²⁰⁶ Contacting opposing ends of a fiber thus allows measurement of interchain transport along the fiber. Four-point-FET measurements yield a mobility of 0.06 cm²/Vs for the transport along a single fiber.²⁰⁷ Activated transport was found in webs of these fibers, in contrast to the band-like temperature dependence of our simulations. However, reducing the polarity of the SiO₂ surface by treatment with hexamethyldisilazane reduces the activation barrier from 108 meV to 65 meV,²⁰⁷ which indicates a strong influence of the surface on the intrinsic mobility. Furthermore, the polymer in our simulation is 100% regioregular, which is not achievable in the experiment. The best commercially* obtainable P3HT has a regioregularity of >98%, but values around 95% are also quite common.

*Sigma-Aldrich, October 2015

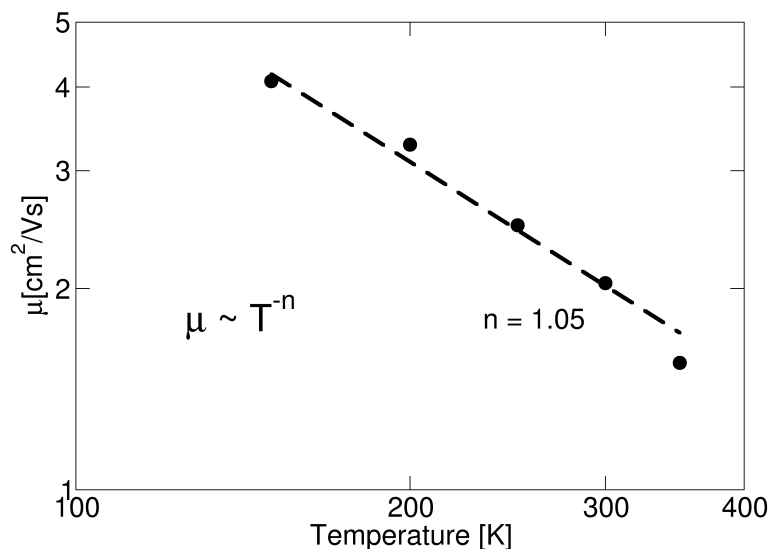


Figure 7.6.: Simulated mobility of P3HT at different temperatures, which can be fitted by a power-law.

7.5. Enforcing Order: HBC

In this section we will continue the simulations of HBC-LC, which were performed for constant temperature in section 6.7 and additionally study the temperature dependence. Furthermore, we will investigate how HBC can be modified to engineer materials with higher mobilities.

In the liquid crystalline phase of HBC, the molecules stack in an unfavorable conformation, where the intermolecular coupling between the molecular HOMOs is near its minimum (see figure 6.10). By modifying the side chains, the relative orientation of molecules in columnar liquid crystals can be changed, which can result in higher mobilities.²⁰⁸ However, one drawback remains in these liquid crystals: The hardly known degree of impurities and defects in solvent-processed HBC derivatives, combined with their strong impact on the charge carrier mobility, complicates the comparison between experiment and simulation. For example in ref. 34 the mobility from PR-TRMC measurements and hopping simulations of a disordered columnar liquid crystal agree quite well, but as soon as the disorder is removed in the simulation by proper annealing, the mobility increases by nearly 2 orders of magnitude, indicating that structural defects

may play an important role in these materials.

Interesting systems that have the potential to reduce the amount of defects and allow to monitor intrinsic mobilities are self-assembling monolayers (SAMs) of π -stacking organic molecules. With SAMs it is possible to obtain very ordered stacks, where the absence of defects can be probed with scanning tunneling microscope (STM) scans.^{209,210} Band-like behavior was proposed for a similar SAM²⁰⁹ and room temperature mobilities of up to $6.8 \text{ cm}^2/\text{Vs}$ were found,²¹⁰ which clearly exceeds the performance of liquid crystalline phases.

In this section we will simulate the temperature dependence of the mobility in HBC-LC to enable a better comparison with the experiment. Additionally, we will study a SAM derived from HBC, where two side chains are functionalized with thiol groups that anchor the molecule to a gold surface and compare how the altered morphology influences the charge transport characteristics.

7.5.1. Simulation Setup

For hexa(3,7-dimethyloctanyl)hexa-peri-hexabenzocoronene (HBC-LC) the same simulation setup as in section 6.1 was used with the QM zone shown in section 6.6, with two degenerate HOMOs per molecule entering the CEID calculations. The duration of the individual simulations was 500 fs. The simulations were performed in the temperature range from 400 K to 600 K, because below 350 K a phase transition from the liquid crystalline to the crystalline phase occurs.⁷

2,5-bis[4-(S-acetylthiomethyl)phenylethynyl]-8,11,14,17-tetrakis(3,7-dimethyloctanyl)hexa-peri-hexabenzocoronene (HBC-SAM) is a derivative of HBC where two side chains are functionalized with thiol groups. The SAM was modeled as 110 molecules in a single stack. The last atom of both anchoring side chains were kept fixed during the simulation to mimic the anchoring to the surface. The gold surface was not modeled explicitly, since in such an upright orientation the molecules stand on their anchoring side chains, leaning on each other, and therefore no significant interaction with the surface can be expected. The angle between the molecular plane and the surface correlates with the degree of surface coverage. Several degrees of molecular coverage were tested, and the experimental NEXAFS angle of 65° was reproduced best with an intermolecular spacing of 3.9 \AA along the stacking direction.²¹⁰ No pressure coupling was applied, with fixed box dimensions in the surface plane of 42.9 nm and 3 nm along and perpendicular of

the stacking direction, respectively. 3-dimensional periodic boundary conditions were applied, enabling particle-mesh-Ewald (PME) electrostatics. However, the box axis perpendicular to the surface was increased to 6 nm to avoid steric interactions and a force and potential correction was applied in the PME calculations to produce a pseudo-2D summation.

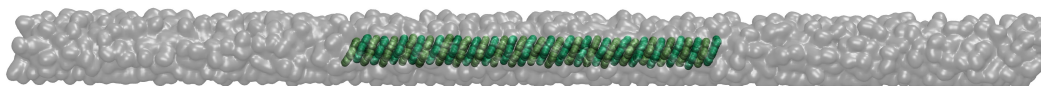


Figure 7.7.: The 30 molecules in the QM zone (green) of HBC-SAM. The monolayer was modeled as a single column of 110 molecules with increased box dimension perpendicular to the virtual gold surface.

7.5.2. Results and Discussion

As can be seen in figure 7.8 we find decreasing mobility with increasing temperature for both systems. In HBC-LC the mobility ranges from 1.81 cm²/Vs at 400 K to 1.19 cm²/Vs at 600 K and follows a power-law ($\mu \propto T^{-n}$) with an exponent of $n = 1.06$. A band-like behavior is less expected in the HBC liquid crystal compared to the anthracene single crystal, due to the increased disorder. However, the good fit ($r^2 > 0.965$) of $\mu = C * T^{-n}$ to the simulated data and the exponent of $n = 1.06$, which is in the typical range for band-like transport, strongly indicate that large-polaron, band-like transport is the predominant charge transport regime for the defect-free liquid crystal.

Due to the different morphology, significantly larger values were observed in HBC-SAM ranging from 3.99 to 4.93 cm²/Vs. At 400 K the mobility is larger by a factor of two, compared to HBC-LC, and also the temperature dependence is significantly weaker with an exponent of $n = 0.45$.

Compared to PR-TRMC measurements on the liquid-crystalline phase of HBC derivatives we overestimate the mobility roughly by a factor of five.¹⁸² Furthermore, the experimental mobility is observed to be nearly temperature independent in this phase. As already mentioned in section 6.7, missing impurities and defects would explain an overestimation of the mobility. Furthermore, since the detrapping of the charge is temperature-activated, the inclusion of defects in the simulation will counteract the trend of decreasing

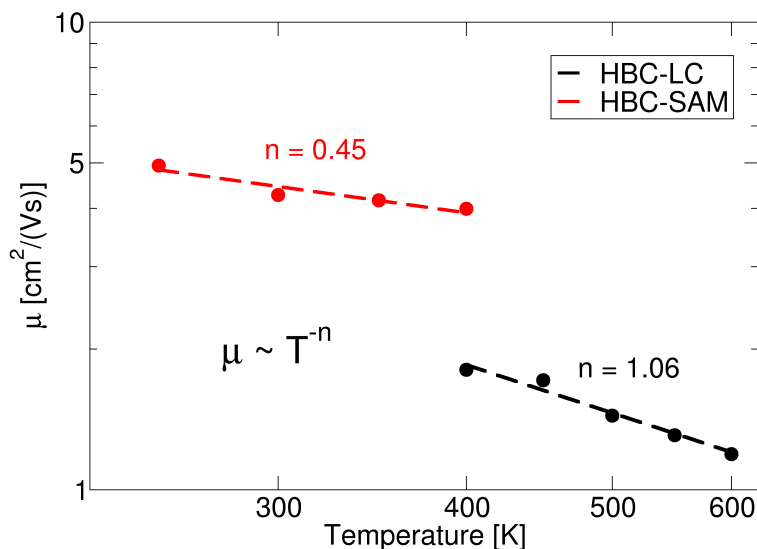


Figure 7.8.: Simulated mobility of the liquid crystalline derivative of HBC (HBC-LC) and of the self-assembling monolayer of HBC (HBC-SAM) for different temperatures fitted by a power-law ($\mu = C * T^{-n}$).

mobility at higher temperatures, yielding a temperature dependence in better agreement with the experiment. Another observation, strengthening the assumption that defects may be responsible for the differences in the mobility between experiment and simulation, is that even in the crystalline phase of a variety of HBC derivatives an increasing mobility with higher temperatures was found.^{182,211} It was argued that such a temperature dependence in crystalline materials points to insufficient purification and does not reflect the intrinsic mobility of the material.²⁹ Furthermore, it is known that rotations of the molecular disks around the columnar axis are possible in the liquid crystalline phase.²¹² Considering the strong dependence of the electronic coupling on the relative orientation of two molecules (see figure 6.10), such structural defects can have a strong impact on the charge carrier dynamic of the system. In our MD simulations, however, these slow structural changes are not observable on the nanosecond time scale. In order to get better insight into these kind of defects, more elaborate methods like umbrella sampling²¹³ have to be applied. The calculation of relative activation barriers for the rotation of a single molecule versus the concerted rotation of a larger part of the columnar stack could be a first step, followed by a CEID simulation of systems with such structural defects.

For the single molecular layer in HBC-SAM it is not possible to derive mobilities with standard techniques like TOF, PR-TRMC or TFT measurements. However, it is possible to derive some estimates from STM data.^{209,210} For this system a mobility of $6.8 \text{ cm}^2/\text{Vs}$ was estimated, significantly higher than the PR-TRMC experiments of the liquid crystal, and in good agreement with our calculation. Furthermore, for a similar system with a single anchoring side chain an increasing mobility at lower temperatures was derived from the STM data, which is in agreement with our predicted temperature dependence for pure HBC-SAMs and liquid crystals.

7.6. Conclusion

In summary we were able to predict mobilities in a range of three orders of magnitude as shown in figure 7.9 and were also able to reproduce the typical temperature dependencies that are significant for band-like transport in single crystals like anthracene, as well as activated hopping in amorphous materials like α -NPD. However, we find decreasing mobility with increasing temperature also in semi-crystalline materials like the liquid crystal HBC-LC and the polymer P3HT, in contrast to experimental observations. From the extrapolation of the mobility to the high-temperature limit in α -NPD we concluded that we are underestimating the depth of the charge-trapping. This can result either from a too small energetic disorder, a too weak molecular relaxation or the absence of impurities. Furthermore, we have shown for HBC that small modifications of the molecules can lead to higher and less temperature sensitive mobilities, which is a desirable feature for high-performance devices. Atomistic bottom-up simulation of charge carrier dynamic with the CEID method is thus a valuable tool for complementing experimental results and might be used for the rational design of OSCs in the future.

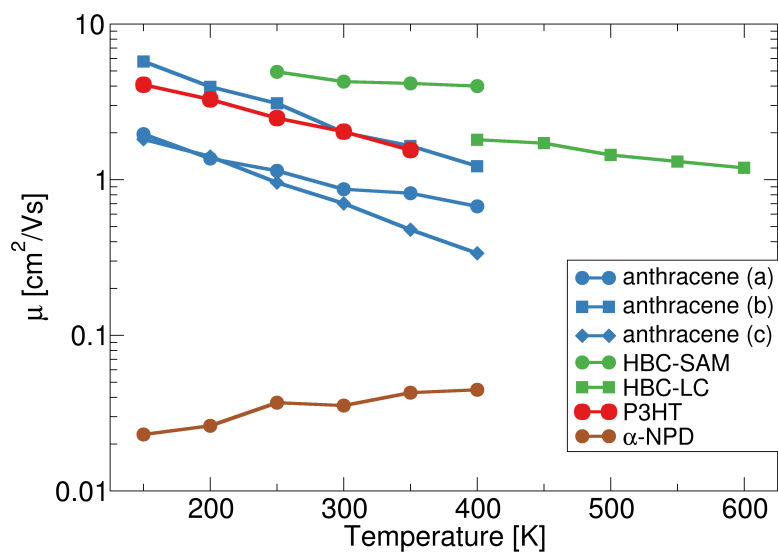


Figure 7.9.: Summary of the temperature dependent mobilities of all system studied in this chapter. System specific temperature dependences are obtained and mobilities in a range of three orders of magnitude are accessible.

Summary and Future Work

In this work, several efficient methods for the investigation of electron transfer in OSCs were developed, advanced, and assessed.

In particular in chapter 3 we have further developed and benchmarked an efficient fragment orbital method based on the semi-empirical method DFTB. We found that the coupling of fragment orbital methods is underestimated systematically, which was attributed to the non-exact calculation of exchange-correlation. The application of constant scaling factors was proposed, which reduces the errors both for hole and electron transfer significantly. This efficient correction scheme makes FODFTB comparably accurate to FODFT calculations with the PBE functional, while being six orders of magnitude faster. This shows that FODFTB is suitable for applications like scanning of the electronic couplings of large data bases, or for propagation of the charge carrier along an MD simulation with the CEID method.

Furthermore, in chapter 4 we tested this Hamiltonian for the calculation of bridge-mediated electronic coupling. We found that the distance dependence of the electronic coupling, obtained with our FODFTB Hamiltonian, is similar to CDFT results. Both methods, however, experience difficulties in the correct reproduction of the barrier height.

In chapter 5 we have shown that conventional CEID simulations may fail for OSCs because of the SI error in the total energy expression. We developed an SI-free variant of CEID, where we included additionally (non-)local electron-phonon coupling in a consistent manner.

In chapter 6 we applied this method to two well-characterized OSCs and found that we can reproduce the absolute values as well as the anisotropy of experimental mobilities with excellent accuracy. We furthermore showed for HBC that it may not be sufficient to

consider only the degenerate molecular HOMOs in the charge transfer, as usually done. Inclusion of energetically lower lying orbitals was found to have a significant influence on the charge carrier dynamics.

In chapter 7 we have investigated the temperature dependence of the mobility for different systems. Band-like temperature dependence as well as activated hopping were observable, depending on the morphology of the OSC. Usually, we found higher mobilities compared to the experiment, which can be expected considering that we simulate only pristine materials without any dopants or impurities.

Future studies will therefore focus on the investigation of the effect of structural defects and impurities on the CEID simulations. While we studied only interstrand transport in the polymer P3HT in section 7.4, it would also be desirable to simulate intrastrand transport. However, the fragmentation of polymer chains is much more difficult than the fragmentation of OSCs consisting of small molecules. Application of specially parametrized capping atoms can facilitate the fragmentation of such systems, as we have recently demonstrated for CT over peptide backbones.¹⁷³ Furthermore, the inclusion of electronic polarization effects, is a necessary next step for the simulation of more heterogeneous systems like interfaces, as we have discussed in section 5.5.

Appendix

A.1. Electronic Couplings with Degenerated States

In the case of degenerated HOMOs (or LUMOs) there exist in general several charge transfer integrals between two fragments. For two degenerated orbitals $\{\phi_n^a, \phi_n^b\}$ on each of two fragments n the Hamilton matrix can be written as

$$H = \begin{pmatrix} \epsilon_1 & 0 & V_{aa} & V_{ab} \\ 0 & \epsilon_1 & V_{ba} & V_{bb} \\ V_{aa} & V_{ba} & \epsilon_2 & 0 \\ V_{ab} & V_{bb} & 0 & \epsilon_2 \end{pmatrix} \quad (\text{A.1})$$

with $V_{ab} = \langle \phi_1^a | \hat{H} | \phi_2^b \rangle$. However, there is a unitary transformation

$$U = \begin{pmatrix} \cos(\alpha) & \sin(\alpha) & 0 & 0 \\ -\sin(\alpha) & \cos(\alpha) & 0 & 0 \\ 0 & 0 & \cos(\beta) & \sin(\beta) \\ 0 & 0 & -\sin(\beta) & \cos(\beta) \end{pmatrix} \quad (\text{A.2})$$

where α and β are the rotation angles for orbitals on fragment 1 and 2, so that

$$H' = U^{-1} H U = \begin{pmatrix} \epsilon_1 & 0 & V'_{aa} & V'_{ab} \\ 0 & \epsilon_1 & V'_{ba} & V'_{bb} \\ V'_{aa} & V'_{ba} & \epsilon_2 & 0 \\ V'_{ab} & V'_{bb} & 0 & \epsilon_2 \end{pmatrix} \stackrel{!}{=} \begin{pmatrix} \epsilon_1 & 0 & V'_{aa} & 0 \\ 0 & \epsilon_1 & 0 & V'_{bb} \\ V'_{aa} & 0 & \epsilon_2 & 0 \\ 0 & V'_{bb} & 0 & \epsilon_2 \end{pmatrix} \quad (\text{A.3})$$

The requirements

$$\begin{aligned}
 0 &\stackrel{!}{=} V'_{ab} = \frac{1}{2}((V_{ab} - V_{ba}) \cos(\alpha - \beta) + (V_{ab} + V_{ba}) \cos(\alpha + \beta) \\
 &\quad + (V_{aa} + V_{bb}) \sin(\alpha - \beta) - (V_{aa} - V_{bb}) \sin(\alpha + \beta)) \\
 0 &\stackrel{!}{=} V'_{ba} = \frac{1}{2}((-V_{ab} + V_{ba}) \cos(\alpha - \beta) + (V_{ab} + V_{ba}) \cos(\alpha + \beta) \\
 &\quad - (V_{aa} + V_{bb}) \sin(\alpha - \beta) - (V_{aa} - V_{bb}) \sin(\alpha + \beta))
 \end{aligned}$$

the sum of these two equations leads to:

$$(V_{ab} + V_{ba}) \cos(\alpha + \beta) - (V_{aa} - V_{bb}) \sin(\alpha + \beta) = 0 \quad (\text{A.4})$$

$$\tan(\alpha + \beta) = \frac{V_{ab} + V_{ba}}{V_{aa} - V_{bb}} \quad (\text{A.5})$$

$$\alpha + \beta = \arctan\left(\frac{V_{ab} + V_{ba}}{V_{aa} - V_{bb}}\right) \quad (\text{A.6})$$

and the difference to:

$$(V_{ab} - V_{ba}) \cos(\alpha - \beta) + (V_{aa} + V_{bb}) \sin(\alpha - \beta) = 0 \quad (\text{A.7})$$

$$\tan(\alpha - \beta) = \frac{V_{ba} - V_{ab}}{V_{aa} + V_{bb}} \quad (\text{A.8})$$

$$\alpha - \beta = \arctan\left(\frac{V_{ba} - V_{ab}}{V_{aa} + V_{bb}}\right) \quad (\text{A.9})$$

This defines α and β and thus lead to a new set of orbitals where ‘‘cross-couplings’’ are zero due to symmetry reasons (e.g. one set σ - and one set π -interacting orbitals).

In this symmetry adapted basis the orthogonalized Hamiltonian can be written as

$$H'_{ortho} = U^{-1} S^{-\frac{1}{2}} U U^{-1} H U U^{-1} S^{-\frac{1}{2}} U = U^{-1} S^{-\frac{1}{2}} H S^{-\frac{1}{2}} U \quad (\text{A.10})$$

A.2. Test of Basis Sets and FODFTB Methods

In ref. 118 the influence of compression radius on electronic coupling was studied. It was found that increasing the density confinement radius r_0^{dens} yields systematically larger couplings. When the wave function confinement radius r_0^{wf} is increased, however, this

is not generally true, because a more diffuse wavefunction leads also to larger wavefunction overlap. The orthogonalized coupling elements, which are the ones of interest, can therefore decrease with weaker confinement.

We therefore tested both FO methods presented in section 3.1 and 3.2 with the parameterization that was proposed for DNA ($r_0^{dens} = 7$ a.u. and $r_0^{wf} = 8$ a.u.) and also with weaker confined parameterizations, without any confinement of the density. The couplings were calculated for 11 molecules of the hole-transfer set shown in table 3.1 and additionally pyridine, pyrimidine, 4(3H)-pyrimidinone, naphthalene, anthracene, tetracene and pentacene. The monomers were optimized as in section 3.3.2 and the cofacial dimers were build with a stacking separation of 3.5 Å.

As can be seen in figure A.1 we find that with the block matrix method we get typically a little bit lower couplings. However, the differences are quite small and the two methods differ mainly conceptually and less in their numerical results. Furthermore we see that the actual value of the compression radii has only minor impact once the wavefunction is already free enough to expand, which is already the case with the originally proposed set for DNA.

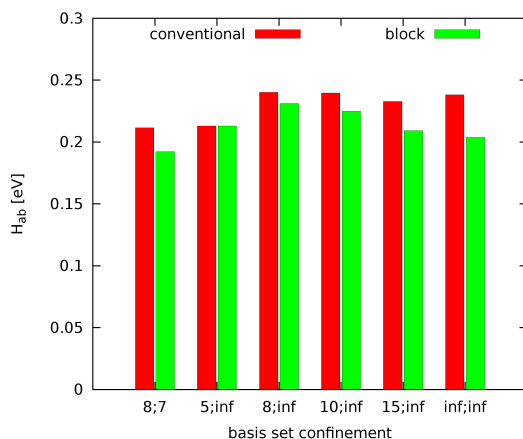


Figure A.1.: Average coupling of 18 π -conjugated molecules with the conventional and the block matrix method Both methods were tested with different confinement radii $r_0^{wf}; r_0^{dens}$.

Bibliography

- [1] J. Ferraris, D. O. Cowan, V. Walatka and J. H. Perlstein, *J. Am. Chem. Soc.*, 1973, **95**, 948–949.
- [2] H. Shirakawa, E. J. Louis, A. G. MacDiarmid, C. K. Chiang and A. J. Heeger, *J. Chem. Soc., Chem. Commun.*, 1977, **0**, 578–580.
- [3] C. K. Chiang, C. R. Fincher, Y. W. Park, A. J. Heeger, H. Shirakawa, E. J. Louis, S. C. Gau and A. G. MacDiarmid, *Phys. Rev. Lett.*, 1977, **39**, 1098–1101.
- [4] S. R. Forrest, *Nature*, 2004, **428**, 911–918.
- [5] J. R. Sheats, *J. Mater. Res.*, 2004, **19**, 1974–1989.
- [6] T. Sekitani, U. Zschieschang, H. Klauk and T. Someya, *Nat Mater*, 2010, **9**, 1015–1022.
- [7] A. Fechtenkötter, N. Tchebotareva, M. Watson and K. Müllen, *Tetrahedron*, 2001, **57**, 3769–3783.
- [8] R. J. Kline, M. D. McGehee, E. N. Kadnikova, J. Liu, J. M. J. Fréchet and M. F. Toney, *Macromolecules*, 2005, **38**, 3312–3319.
- [9] R. J. Kline, M. D. McGehee, E. N. Kadnikova, J. Liu and J. M. J. Fréchet, *Adv. Mater.*, 2003, **15**, 1519–1522.
- [10] H. Dong, X. Fu, J. Liu, Z. Wang and W. Hu, *Adv. Mater.*, 2013, **25**, 6158–6183.
- [11] F. So, J. Kido and P. Burrows, *MRS Bull.*, 2008, **33**, 663–669.
- [12] B. . W. D’Andrade and S. . R. Forrest, *Adv. Mater.*, 2004, **16**, 1585–1595.
- [13] S. Reineke, F. Lindner, G. Schwartz, N. Seidler, K. Walzer, B. Lussem and K. Leo, *Nature*, 2009, **459**, 234–238.
- [14] G. Horowitz, *Adv. Mater.*, 1998, **10**, 365–377.
- [15] M. E. Gershenson, V. Podzorov and A. F. Morpurgo, *Rev. Mod. Phys.*, 2006, **78**, 973–989.
- [16] L. Schmidt-Mende, A. Fechtenkötter, K. Müllen, E. Moons, R. H. Friend and J. D. MacKenzie, *Science*, 2001, **293**, 1119–1122.
- [17] P. Peumans, A. Yakimov and S. R. Forrest, *J. Appl. Phys.*, 2003, **93**, 3693–3723.
- [18] Y.-J. Cheng, S.-H. Yang and C.-S. Hsu, *Chem. Rev.*, 2009, **109**, 5868–5923.

- [19] "Energy and the challenge of sustainability", United Nations Development Programme and World Energy Council, 2000, p. 163; Retrieved from <http://www.undp.org> (Oct 2015).
- [20] "2014 Key World Energy Statistics", International Energy Agency, 2014, p. 26; Retrieved from <http://www.iea.org/publications/freepublications/> (Oct 2015).
- [21] A. F. Sherwani, J. A. Usmani and Varun, *Renew. Sust. Energ. Rev.*, 2010, **14**, 540–544.
- [22] J.-L. Brédas, J. E. Norton, J. Cornil and V. Coropceanu, *Acc. Chem. Res.*, 2009, **42**, 1691–1699.
- [23] J. Gubbi, R. Buyya, S. Marusic and M. Palaniswami, *Future Gener. Comput. Syst.*, 2013, **29**, 1645–1660.
- [24] J. L. Brédas, J. P. Calbert, D. S. Filho and J. Cornil, *Proc. Natl. Acad. Sci. U.S.A.*, 2002, **99**, 5804–5809.
- [25] V. Coropceanu, J. Cornil, D. A. da Silva Filho, Y. Olivier, R. Silbey and J.-L. Brédas, *Chem. Rev.*, 2007, **107**, 926–952.
- [26] A. Troisi and G. Orlandi, *Phys. Rev. Lett.*, 2006, **96**, 086601+.
- [27] A. Troisi and G. Orlandi, *J. Phys. Chem. A*, 2006, **110**, 4065–4070.
- [28] A. Troisi, *Adv. Mater.*, 2007, **19**, 2000–2004.
- [29] A. Troisi, *Chem. Soc. Rev.*, 2011, **40**, 2347–2358.
- [30] J. Nelson, J. J. Kwiatkowski, J. Kirkpatrick and J. M. Frost, *Acc. Chem. Res.*, 2009, **42**, 1768–1778.
- [31] J. J. Kwiatkowski, J. Nelson, H. Li, J. L. Bredas, W. Wenzel and C. Lennartz, *Phys. Chem. Chem. Phys.*, 2008, **10**, 1852–1858.
- [32] P. Friederich, F. Symalla, V. Meded, T. Neumann and W. Wenzel, *J. Chem. Theory Comput.*, 2014, **10**, 3720–3725.
- [33] J. Kirkpatrick, V. Marcon, K. Kremer, J. Nelson and D. Andrienko, *J. Chem. Phys.*, 2008, **129**, 094506+.
- [34] X. Feng, V. Marcon, W. Pisula, M. R. Hansen, J. Kirkpatrick, F. Grozema, D. Andrienko, K. Kremer and K. Müllen, *Nat. Mater.*, 2009, **8**, 421–426.
- [35] V. Marcon, D. W. Breiby, W. Pisula, J. Dahl, J. Kirkpatrick, S. Patwardhan, F. Grozema and D. Andrienko, *J. Am. Chem. Soc.*, 2009, **131**, 11426–11432.
- [36] C. Poelking, E. Cho, A. Malafeev, V. Ivanov, K. Kremer, C. Risko, J.-L. Brédas and D. Andrienko, *J. Phys. Chem. C*, 2013, **117**, 1633–1640.
- [37] V. Rühle, J. Kirkpatrick and D. Andrienko, *J. Chem. Phys.*, 2010, **132**, 134103+.

-
- [38] T. Vehoff, Y. S. Chung, K. Johnston, A. Troisi, D. Y. Yoon and D. Andrienko, *J. Phys. Chem. C*, 2010, **114**, 10592–10597.
- [39] T. Vehoff, B. Baumeier, A. Troisi and D. Andrienko, *J. Am. Chem. Soc.*, 2010, **132**, 11702–11708.
- [40] T. Vehoff, B. Baumeier and D. Andrienko, *J. Chem. Phys.*, 2010, **133**, 134901+.
- [41] F. Ortmann, F. Bechstedt and K. Hannewald, *Phys. Status Solidi B*, 2011, **248**, 511–525.
- [42] D. P. McMahon and A. Troisi, *ChemPhysChem*, 2010, **11**, 2067–2074.
- [43] A. Troisi, *Org. Electron.*, 2011, **12**, 1988–1991.
- [44] F. Gajdos, H. Oberhofer, M. Dupuis and J. Blumberger, *J. Phys. Chem. Lett.*, 2013, **4**, 1012–1017.
- [45] L. Wang and D. Beljonne, *J. Phys. Chem. Lett.*, 2013, **4**, 1888–1894.
- [46] L. Wang and D. Beljonne, *J. Chem. Phys.*, 2013, **139**, 064316.
- [47] A. A. Kocherzhenko, F. C. Grozema and L. D. A. Siebbeles, *Phys. Chem. Chem. Phys.*, 2011, **13**, 2096–2110.
- [48] S. Stafstrom, *Chem. Soc. Rev.*, 2010, **39**, 2484–2499.
- [49] C. Gollub, S. Avdoshenko, R. Gutierrez, Y. Berlin and G. Cuniberti, *Isr. J. Chem.*, 2012, **52**, 452–460.
- [50] X. Gao, H. Geng, Q. Peng, J. Ren, Y. Yi, D. Wang and Z. Shuai, *J. Phys. Chem. C*, 2014, **118**, 6631–6640.
- [51] M. Born and R. Oppenheimer, *Ann. Phys.*, 1927, **389**, 457–484.
- [52] P. Hohenberg and W. Kohn, *Phys. Rev.*, 1964, **136**, B864–B871.
- [53] W. Kohn and L. J. Sham, *Phys. Rev.*, 1965, **140**, A1133–A1138.
- [54] D. M. Ceperley and B. J. Alder, *Phys. Rev. Lett.*, 1980, **45**, 566–569.
- [55] G. Seifert and J.-O. Joswig, *WIREs Comput. Mol. Sci.*, 2012, **2**, 456–465.
- [56] M. Gaus, Q. Cui and M. Elstner, *WIREs Comput. Mol. Sci.*, 2013, **4**, 49–61.
- [57] J. C. Slater and G. F. Koster, *Phys. Rev.*, 1954, **94**, 1498–1524.
- [58] K. Ohno, *Theor. Chim. Acta*, 1964, **2**, 219–227.
- [59] G. Klopman, *J. Am. Chem. Soc.*, 1965, **87**, 3300–3303.
- [60] Q. Cui, M. Elstner, E. Kaxiras, T. Frauenheim and M. Karplus, *J. Phys. Chem. B*, 2001, **105**, 569–585.

- [61] J. P. Perdew, R. G. Parr, M. Levy and J. L. Balduz, *Phys. Rev. Lett.*, 1982, **49**, 1691–1694.
- [62] A. J. Cohen, P. Mori-Sánchez and W. Yang, *Phys. Rev. B*, 2008, **77**, 115123+.
- [63] J. F. Janak, *Phys. Rev. B*, 1978, **18**, 7165–7168.
- [64] P. Mori-Sánchez, A. J. Cohen and W. Yang, *Phys. Rev. Lett.*, 2008, **100**, 146401+.
- [65] T. Bally and G. N. Sastry, *J. Phys. Chem. A*, 1997, **101**, 7923–7925.
- [66] E. Ruiz, D. R. Salahub and A. Vela, *J. Phys. Chem.*, 1996, **100**, 12265–12276.
- [67] M. Lundberg and P. E. M. Siegbahn, *J. Chem. Phys.*, 2005, **122**, 224103+.
- [68] M. Lundberg, Y. Nishimoto and S. Irle, *Int. J. Quantum Chem.*, 2012, **112**, 1701–1711.
- [69] J. Wang, R. M. Wolf, J. W. Caldwell, P. A. Kollman and D. A. Case, *J. Comput. Chem.*, 2004, **25**, 1157–1174.
- [70] W. L. Jorgensen and J. Tirado-Rives, *J. Am. Chem. Soc.*, 1988, **110**, 1657–1666.
- [71] W. L. Jorgensen, D. S. Maxwell and J. Tirado-Rives, *J. Am. Chem. Soc.*, 1996, **118**, 11225–11236.
- [72] R. W. Hockney, S. P. Goel and J. W. Eastwood, *J. Comput. Phys.*, 1974, **14**, 148–158.
- [73] H. J. C. Berendsen, J. P. M. Postma, W. F. van Gunsteren, A. DiNola and J. R. Haak, *J. Chem. Phys.*, 1984, **81**, 3684–3690.
- [74] S. Nosé, *Mol. Phys.*, 1984, **52**, 255–268.
- [75] W. G. Hoover, *Phys. Rev. A*, 1985, **31**, 1695–1697.
- [76] M. Parrinello and A. Rahman, *J. Appl. Phys.*, 1981, **52**, 7182–7190.
- [77] S. Nosé and M. L. Klein, *Mol. Phys.*, 1983, **50**, 1055–1076.
- [78] C. A. Mead and D. G. Truhlar, *J. Chem. Phys.*, 1982, **77**, 6090–6098.
- [79] K. Ruedenberg and G. J. Atchity, *J. Chem. Phys.*, 1993, **99**, 3799–3803.
- [80] G. J. Atchity and K. Ruedenberg, *Theor. Chem. Acc.*, 1997, **97**, 47–58.
- [81] H. Nakamura and D. G. Truhlar, *J. Chem. Phys.*, 2001, **115**, 10353–10372.
- [82] T. Pacher, L. S. Cederbaum and H. Köppel, *J. Chem. Phys.*, 1988, **89**, 7367–7381.
- [83] T. Pacher, L. S. Cederbaum and H. Köppel, in *Adiabatic and Quasidiabatic States in a Gauge Theoretical Framework*, ed. I. Prigogine and S. A. Rice, John Wiley & Sons, Inc., Hoboken, NJ, USA, 1993, vol. 84, pp. 293–391.

-
- [84] R. Cimiraglia, J. P. Malrieu, M. Persico and F. Spiegelmann, *J. Phys. B: At. Mol. Phys.*, 1985, **18**, 3073–3084.
- [85] C.-P. Hsu, *Acc. Chem. Res.*, 2009, **42**, 509–518.
- [86] R. J. Cave and M. D. Newton, *Chem. Phys. Lett.*, 1996, **249**, 15–19.
- [87] R. J. Cave and M. D. Newton, *J. Chem. Phys.*, 1997, **106**, 9213–9226.
- [88] J. E. Subotnik, S. Yeganeh, R. J. Cave and M. A. Ratner, *J. Chem. Phys.*, 2008, **129**, 244101+.
- [89] J. E. Subotnik, R. J. Cave, R. P. Steele and N. Shenvi, *J. Chem. Phys.*, 2009, **130**, 234102+.
- [90] Q. Wu and T. Van Voorhis, *Phys. Rev. A*, 2005, **72**, 024502+.
- [91] F. L. Hirshfeld, *Theor. Chim. Acta*, 1977, **44**, 129–138.
- [92] H. Oberhofer and J. Blumberger, *J. Chem. Phys.*, 2010, **133**, 244105+.
- [93] Q. Wu and T. Van Voorhis, *J. Chem. Phys.*, 2006, **125**, 164105+.
- [94] P. O. Löwdin, *J. Chem. Phys.*, 1950, **18**, 365–375.
- [95] M. D. Newton, *Chem. Rev.*, 1991, **91**, 767–792.
- [96] H. Oberhofer and J. Blumberger, *Phys. Chem. Chem. Phys.*, 2012, **14**, 13846+.
- [97] K. Senthilkumar, F. C. Grozema, F. M. Bickelhaupt and L. D. A. Siebbeles, *J. Chem. Phys.*, 2003, **119**, 9809.
- [98] K. Senthilkumar, F. C. Grozema, C. F. Guerra, F. M. Bickelhaupt, F. D. Lewis, Y. A. Berlin, M. A. Ratner and L. D. A. Siebbeles, *J. Am. Chem. Soc.*, 2005, **127**, 14894–14903.
- [99] Troisi, Alessandro (2009) Theories of the charge transport mechanism in ordered organic semiconductors. In: Malinova, Violeta and Belegriou, S. (Serena) and Bruyn Ouboter, Dirk and Meier, Wolfgang Peter, (eds.) *Advances in Polymer Science*. Springer, pp. 213–258.
- [100] A. Miller and E. Abrahams, *Phys. Rev.*, 1960, **120**, 745–755.
- [101] H. Bässler, *Phys. Status Solidi B*, 1993, **175**, 15–56.
- [102] R. A. Marcus, *J. Chem. Phys.*, 1956, **24**, 966–978.
- [103] R. A. Marcus, *J. Chem. Phys.*, 1956, **24**, 979–989.
- [104] R. A. Marcus, *Annu. Rev. Phys. Chem.*, 1964, **15**, 155–196.
- [105] R. Marcus and N. Sutin, *Biochim. Biophys. Acta, Rev. Bioenerg.*, 1985, **811**, 265–322.

- [106] S. S. Skourtis, D. H. Waldeck and D. N. Beratan, *Annu. Rev. Phys. Chem.*, 2010, **61**, 461–485.
- [107] A. Heck, P. B. Woiczikowski, T. Kubař, B. Giese, M. Elstner and T. B. Steinbrecher, *J. Phys. Chem. B*, 2012, **116**, 2284–2293.
- [108] J. R. Miller, L. T. Calcaterra and G. L. Closs, *J. Am. Chem. Soc.*, 1984, **106**, 3047–3049.
- [109] T. Kubař and M. Elstner, *J. Phys. Chem. B*, 2010, **114**, 11221–11240.
- [110] T. Kubař and M. Elstner, *Phys. Chem. Chem. Phys.*, 2013, **15**, 5794–5813.
- [111] N. Karl and J. Marktanner, *Mol. Cryst. Liq. Cryst. Sci. Technol., Sect. A*, 2001, **355**, 149–173.
- [112] Y. A. Mantz, F. L. Gervasio, T. Laino and M. Parrinello, *J. Phys. Chem. A*, 2006, **111**, 105–112.
- [113] A. Kokil, K. Yang and J. Kumar, *J. Polym. Sci. B Polym. Phys.*, 2012, **50**, 1130–1144.
- [114] K. Hong, S. Y. Yang, C. Yang, S. H. Kim, D. Choi and C. E. Park, *Org. Electron.*, 2008, **9**, 864–868.
- [115] A. Kubas, F. Hoffmann, A. Heck, H. Oberhofer, M. Elstner and J. Blumberger, *J. Chem. Phys.*, 2014, **140**, 104105+.
- [116] A. Kubas, F. Gajdos, A. Heck, H. Oberhofer, M. Elstner and J. Blumberger, *Phys. Chem. Chem. Phys.*, 2015, **17**, 14342–14354.
- [117] T. Kubař and M. Elstner, *J. R. Soc., Interface*, 2013, **10**, 20130415+.
- [118] T. Kubař, P. B. Woiczikowski, G. Cuniberti and M. Elstner, *J. Phys. Chem. B*, 2008, **112**, 7937–7947.
- [119] P. G. Szalay, T. Müller, G. Gidofalvi, H. Lischka and R. Shepard, *Chem. Rev.*, 2012, **112**, 108–181.
- [120] S. R. Langhoff and E. R. Davidson, *Int. J. Quantum Chem.*, 1974, **8**, 61–72.
- [121] W. Butscher, S.-K. Shih, R. J. Buenker and S. D. Peyerimhoff, *Chem. Phys. Lett.*, 1977, **52**, 457–462.
- [122] C. Angeli, R. Cimiraglia, S. Evangelisti, T. Leininger and J. P. Malrieu, *J. Chem. Phys.*, 2001, **114**, 10252–10264.
- [123] C. Angeli, R. Cimiraglia and J.-P. Malrieu, *Chem. Phys. Lett.*, 2001, **350**, 297–305.
- [124] C. Angeli, R. Cimiraglia and J.-P. Malrieu, *J. Chem. Phys.*, 2002, **117**, 9138–9153.
- [125] A. Hellweg, S. A. Grun and C. Hattig, *Phys. Chem. Chem. Phys.*, 2008, **10**, 4119–4127.

- [126] S. Grimme, L. Goerigk and R. F. Fink, *WIREs Comput. Mol. Sci.*, 2012, **2**, 886–906.
- [127] K. Eichkorn, O. Treutler, H. Öhm, M. Häser and R. Ahlrichs, *Chem. Phys. Lett.*, 1995, **240**, 283–290.
- [128] M. Sierka, A. Hogekamp and R. Ahlrichs, *J. Chem. Phys.*, 2003, **118**, 9136–9148.
- [129] R. Ahlrichs, M. Bär, M. Häser, H. Horn and C. Kölmel, *Chem. Phys. Lett.*, 1989, **162**, 165–169.
- [130] TURBOMOLE version 6.5, a development of University of Karlsruhe and Forschungszentrum Karlsruhe GmbH, 1989–2007, TURBOMOLE GmbH, 2013, see <http://www.turbomole.com>.
- [131] CPMD, <http://www.cpmc.org/>, Copyright IBM Corp 1990-2015, Copyright MPI für Festkörperforschung Stuttgart 1997-2001.
- [132] J. P. Perdew, K. Burke and M. Ernzerhof, *Phys. Rev. Lett.*, 1996, **77**, 3865–3868.
- [133] J. P. Perdew, K. Burke and M. Ernzerhof, *Phys. Rev. Lett.*, 1997, **78**, 1396.
- [134] N. Troullier and J. L. Martins, *Phys. Rev. B*, 1991, **43**, 1993–2006.
- [135] G. te Velde, F. M. Bickelhaupt, E. J. Baerends, C. Fonseca Guerra, S. J. A. van Gisbergen, J. G. Snijders and T. Ziegler, *J. Comput. Chem.*, 2001, **22**, 931–967.
- [136] M. Elstner, D. Porezag, G. Jungnickel, J. Elsner, M. Haugk, T. Frauenheim, S. Suhai and G. Seifert, *Phys. Rev. B*, 1998, **58**, 7260–7268.
- [137] T. Kubař, Z. Bodrog, M. Gaus, C. Köhler, B. Aradi, T. Frauenheim and M. Elstner, *J. Chem. Theory Comput.*, 2013, **9**, 2939–2949.
- [138] T. Niehaus, *J. Mol. Struct. THEOCHEM*, 2001, **541**, 185–194.
- [139] M. Gaus, Q. Cui and M. Elstner, *J. Chem. Theory Comput.*, 2011, **7**, 931–948.
- [140] C. Sutton, J. S. Sears, V. Coropceanu and J.-L. Brédas, *J. Phys. Chem. Lett.*, 2013, **4**, 919–924.
- [141] J. Moens, R. Seidel, P. Geerlings, M. Faubel, B. Winter and J. Blumberger, *J. Phys. Chem. B*, 2010, **114**, 9173–9182.
- [142] Y. Tateyama, J. Blumberger, T. Ohno and M. Sprik, *J. Chem. Phys.*, 2007, **126**, 204506+.
- [143] V. Coropceanu, Y. Li, Y. Yi, L. Zhu and J. L. Brédas, *MRS Bull.*, 2013, **38**, 57–64.
- [144] E. Maggio and A. Troisi, *Philos. Trans. R. Soc. London, Ser. A*, 2014, **372**, 20130011+.
- [145] C. Liang and M. D. Newton, *J. Phys. Chem.*, 1992, **96**, 2855–2866.

- [146] K. D. Jordan and M. N. Paddon-Row, *J. Phys. Chem.*, 1992, **96**, 1188–1196.
- [147] L. A. Curtiss, C. A. Naleway and J. R. Miller, *Chem. Phys.*, 1993, **176**, 387–405.
- [148] P.-O. Löwdin, *J. Mol. Spectrosc.*, 1963, **10**, 12–33.
- [149] P.-O. Löwdin, *J. Mol. Spectrosc.*, 1964, **14**, 112–118.
- [150] S. Priyadarshy, S. S. Skourtis, S. M. Risser and D. N. Beratan, *J. Chem. Phys.*, 1996, **104**, 9473–9481.
- [151] S. Grimme, *J. Comput. Chem.*, 2006, **27**, 1787–1799.
- [152] A. Schäfer, C. Huber and R. Ahlrichs, *J. Chem. Phys.*, 1994, **100**, 5829–5835.
- [153] B. Aradi, B. Hourahine and T. Frauenheim, *J. Phys. Chem. A*, 2007, **111**, 5678–5684.
- [154] J. Tao, J. P. Perdew, V. N. Staroverov and G. E. Scuseria, *Phys. Rev. Lett.*, 2003, **91**, 146401+.
- [155] J. P. Perdew, J. Tao, V. N. Staroverov and G. E. Scuseria, *J. Chem. Phys.*, 2004, **120**, 6898–6911.
- [156] A. D. Becke, *J. Chem. Phys.*, 1993, **98**, 5648–5652.
- [157] C. Adamo and V. Barone, *J. Chem. Phys.*, 1999, **110**, 6158–6170.
- [158] A. D. Becke, *J. Chem. Phys.*, 1993, **98**, 1372–1377.
- [159] S.G. Lias, "Ionization Energy Evaluation" in NIST Chemistry WebBook, NIST Standard Reference Database Number 69, Eds. P.J. Linstrom and W.G. Mallard, National Institute of Standards and Technology, Gaithersburg MD, 20899, <http://webbook.nist.gov>, (retrieved January 2, 2016).
- [160] G. Lüdemann, P. B. Woiczikowski, T. Kubař, M. Elstner and T. B. Steinbrecher, *J. Phys. Chem. B*, 2013, **117**, 10769–10778.
- [161] G. Lüdemann, I. A. Solov'yov, T. Kubař and M. Elstner, *J. Am. Chem. Soc.*, 2015, **137**, 1147–1156.
- [162] A. A. Voityuk, *Chem. Phys. Lett.*, 2006, **427**, 177–180.
- [163] M. Elstner and G. Seifert, *Philos. Trans. R. Soc., A*, 2014, **372**, 20120483+.
- [164] M. Elstner, *J. Phys. Chem. A*, 2007, **111**, 5614–5621.
- [165] D. Van Der Spoel, E. Lindahl, B. Hess, G. Groenhof, A. E. Mark and H. J. C. Berendsen, *J. Comput. Chem.*, 2005, **26**, 1701–1718.
- [166] S. Páll, M. Abraham, C. Kutzner, B. Hess and E. Lindahl, *Solving Software Challenges for Exascale*, Springer International Publishing, 2015, vol. 8759, pp. 3–27.
- [167] E. Deumens, A. Diz, R. Longo and Y. Öhrn, *Rev. Mod. Phys.*, 1994, **66**, 917–983.

- [168] D. Marx and J. Hutter, *Ab Initio Molecular Dynamics: Basic Theory and Advanced Methods*, Cambridge University Press, 1st edn, 2009.
- [169] M. Fähnle, C. Elsässer and H. Krimmel, *Phys. Status Solidi B*, 1995, **191**, 9–19.
- [170] L. E. Ratcliff, L. Grisanti, L. Genovese, T. Deutsch, T. Neumann, D. Danilov, W. Wenzel, D. Beljonne and J. Cornil, *J. Chem. Theory Comput.*, 2015, **11**, 2077–2086.
- [171] P. Friederich, V. Meded, F. Symalla, M. Elstner and W. Wenzel, *J. Chem. Theory Comput.*, 2015, **11**, 560–567.
- [172] A. J. Cohen, P. Mori-Sánchez and W. Yang, *Science*, 2008, **321**, 792–794.
- [173] A. Heck, P. B. Woiczikowski, T. Kubař, K. Welke, T. Niehaus, B. Giese, S. Skourtis, M. Elstner and T. B. Steinbrecher, *J. Phys. Chem. B*, 2014, **118**, 4261–4272.
- [174] N. Karl, *Organic Crystals, Germanates, Semiconductors*, Springer Berlin Heidelberg, 1980, vol. 4, pp. 1–100.
- [175] B. R. Kaafarani, *Chem. Mater.*, 2011, **23**, 378–396.
- [176] C. P. Brock and J. D. Dunitz, *Acta Crystallogr., Sect. B: Struct. Sci*, 1990, **46**, 795–806.
- [177] C. I. Bayly, P. Cieplak, W. Cornell and P. A. Kollman, *J. Phys. Chem.*, 1993, **97**, 10269–10280.
- [178] J. Wang, W. Wang, P. A. Kollman and D. A. Case, *J. Mol. Graphics Modell.*, 2006, **25**, 247–260.
- [179] J. A. Kalinowski, B. Lesyng, J. D. Thompson, C. J. Cramer and D. G. Truhlar, *J. Phys. Chem. A*, 2004, **108**, 2545–2549.
- [180] T. Darden, D. York and L. Pedersen, *J. Chem. Phys.*, 1993, **98**, 10089–10092.
- [181] V. Lemaure, D. A. da Silva Filho, V. Coropceanu, M. Lehmann, Y. Geerts, J. Piris, M. G. Debije, A. M. van de Craats, K. Senthilkumar, L. D. A. Siebbeles, J. M. Warman, J.-L. Brédas and J. Cornil, *J. Am. Chem. Soc.*, 2004, **126**, 3271–3279.
- [182] A. M. van de Craats, J. M. Warman, A. Fechtenkötter, J. D. Brand, M. A. Harbison and K. Müllen, *Adv. Mater.*, 1999, **11**, 1469–1472.
- [183] O. V. Gritsenko, P. R. T. Schipper and E. J. Baerends, *Chem. Phys. Lett.*, 1999, **302**, 199–207.
- [184] P. R. T. Schipper, O. V. Gritsenko, S. J. A. van Gisbergen and E. J. Baerends, *J. Chem. Phys.*, 2000, **112**, 1344–1352.
- [185] H. Tada, H. Touda, M. Takada and K. Matsushige, *Appl. Phys. Lett.*, 2000, **76**, 873–875.

- [186] L. Li, Q. Tang, H. Li, X. Yang, W. Hu, Y. Song, Z. Shuai, W. Xu, Y. Liu and D. Zhu, *Adv. Mater.*, 2007, **19**, 2613–2617.
- [187] J. Kirkpatrick, V. Marcon, J. Nelson, K. Kremer and D. Andrienko, *Phys. Rev. Lett.*, 2007, **98**, 227402.
- [188] E. Mozafari and S. Stafström, *J. Chem. Phys.*, 2013, **138**, 184104+.
- [189] J. Wade, F. Steiner, D. Niedzialek, D. T. James, Y. Jung, D.-J. Yun, D. D. C. Bradley, J. Nelson and J.-S. Kim, *J. Mater. Chem. C*, 2014, **2**, 10110–10115.
- [190] J. Ren, N. Vukmirović and L.-W. Wang, *Phys. Rev. B*, 2013, **87**, 205117+.
- [191] W. Gao and A. Kahn, *J. Phys.: Condens. Matter*, 2003, **15**, S2757–S2770.
- [192] J.-W. Kang, D.-S. Lee, H.-D. Park, J. W. Kim, W.-I. Jeong, Y.-S. Park, S.-H. Lee, K. Go, J.-S. Lee and J.-J. Kim, *Org. Electron.*, 2008, **9**, 452–460.
- [193] K. S. Son, M. Yahiro, T. Imai, H. Yoshizaki and C. Adachi, *Chem. Mater.*, 2008, **20**, 4439–4446.
- [194] S. Lee, C.-H. Chung and S. M. Cho, *Synth. Met.*, 2002, **126**, 269–273.
- [195] S. Naka, H. Okada, H. Onnagawa, Y. Yamaguchi and T. Tsutsui, *Synth. Met.*, 2000, **111-112**, 331–333.
- [196] C. Lin, Y. Chen, H. Chen, F. Fang, Y. Lin, W. Hung, K. Wong, R. Kwong and S. Xia, *Org. Electron.*, 2009, **10**, 181–188.
- [197] C. H. Cheung, K. K. Tsung, K. C. Kwok and S. K. So, *Appl. Phys. Lett.*, 2008, **93**, 083307+.
- [198] N. D. Nguyen, M. Schmeits and H. P. Loeb, *Phys. Rev. B*, 2007, **75**, 075307++.
- [199] K. K. Tsung and S. K. So, *Org. Electron.*, 2009, **10**, 661–665.
- [200] E. J. Samuelsen and J. Mardalen, *Handbook of Organic Conductive Molecules and Polymers*, Wiley, Chichester, UK, 1997, vol. 3, pp. 87–120.
- [201] C. Poelking and D. Andrienko, *Macromolecules*, 2013, **46**, 8941–8956.
- [202] M. Moreno, M. Casalegno, G. Raos, S. V. Meille and R. Po, *J. Phys. Chem. B*, 2010, **114**, 1591–1602.
- [203] H. Sirringhaus, N. Tessler and R. H. Friend, *Science*, 1998, **280**, 1741–1744.
- [204] Z. Bao, A. Dodabalapur and A. J. Lovinger, *Appl. Phys. Lett.*, 1996, **69**, 4108–4110.
- [205] T. Erb, U. Zhokhavets, G. Gobsch, S. Raleva, B. Stühn, P. Schilinsky, C. Waldauf and C. J. Brabec, *Adv. Funct. Mater.*, 2005, **15**, 1193–1196.
- [206] J. A. Merlo and C. D. Frisbie, *J. Phys. Chem. B*, 2004, **108**, 19169–19179.
- [207] J. A. Merlo and C. D. Frisbie, *J. Polym. Sci. B Polym. Phys.*, 2003, **41**, 2674–2680.

- [208] W. Pisula, X. Feng and K. Müllen, *Adv. Mater.*, 2010, **22**, 3634–3649.
- [209] D. Käfer, A. Bashir, X. Dou, G. Witte, K. Müllen and C. Wöll, *Adv. Mater.*, 2010, **22**, 384–388.
- [210] A. Bashir, A. Heck, A. Narita, X. Feng, A. Nefedov, M. Rohwerder, K. Müllen, M. Elstner and C. Wöll, *Phys. Chem. Chem. Phys.*, 2015, **17**, 21988–21996.
- [211] J. M. Warman and A. M. Van De Craats, *Mol. Cryst. Liq. Cryst.*, 2003, **396**, 41–72.
- [212] I. Fischbach, T. Pakula, P. Minkin, A. Fechtenkötter, K. Müllen, H. W. Spiess and K. Saalwächter, *J. Phys. Chem. B*, 2002, **106**, 6408–6418.
- [213] S. Kumar, J. M. Rosenberg, D. Bouzida, R. H. Swendsen and P. A. Kollman, *J. Comput. Chem.*, 1992, **13**, 1011–1021.

Curriculum Vitae

Name	Alexander Heck
Date of birth	13. April 1987
Place of birth	Malsch bei Karlsruhe
Nationality	German
9/2012 – present	PhD student at the Institute of Physical Chemistry of the Karlsruhe Institute of Technology
4/2007 – 4/2012	Studies in chemistry at the Karlsruhe Institute of Technology 4/2012 Diploma, Title of the Thesis: „Berechnung von Elektronentransfer-Parametern in solvatisierten Peptiden“ 3/2009 Intermediate Diploma
9/1997 – 6/2006	Albertus-Magnus-Gymnasium in Ettlingen
8/1993 – 7/1997	Johann-Peter-Hebel-Schule in Malsch